POLITECNICO DI TORINO

DEPARTMENT OF MECHANICAL AND AEROSPACE ENGINEERING

Master's Degree Thesis in Biomedical Engineering

Development of a Neural Network - Based CAD system for automated classification of ECG anomalies using wearable technology

Academic Supervisor
Gabriella OLMO

Company Supervisors
Alessandro GUMIERO
Stéphane PICCOLO

Candidate
Marta BARBERIS

A.Y. 2022/2023

Abstract

In recent times, there has been growing attention towards Computer-Aided Diagnosis (CAD) systems dedicated to the automated analysis of electrocardiograms (ECGs). These systems have gained significant interest due to their potential to facilitate the diagnostic process and improve the precision of cardiac anomaly identification and classification. Furthermore, CAD systems can be situated within the broader context of telemedicine, specifically telecardiology and remote monitoring of cardiac conditions.

It is within this context that this thesis work is situated, presenting a method that employs Artificial Intelligence (AI) for the automatic classification of cardiac anomalies. It is based on the ECG traces acquired through a three-lead ECG wearable patch device, commercialised by CGM and designed in collaboration with STMicroelectronics, called 'HI ECG 3-LEAD'. This battery-powered device is designed to be applied with adhesive electrodes to the patient's chest, allowing the acquisition, recording, and transmission of one to three channels of ECG and other physiological parameters (body position, subject's activity status, MEMS data) to an external device via Bluetooth technology. Due to its simplicity, safety, wireless connectivity, and battery life in excess of 24 hours, it is well-suited for monitoring cardiac arrhythmias in non-hospital environments. Additionally, the proposed system aims to provide valuable assistance to cardiologists in examining and reporting of ECG signals, reducing the analysis time and increasing the accuracy in identifying and classifying cardiac anomalies.

The method consists of two main stages. In the first stage, following appropriate pre-processing of the ECG signal, the positioning of the device on the user's chest is identified to correct any potential electrode misplacement that could compromise the subsequent analysis of cardiac anomalies. This prediction has been addressed as a ternary classification problem, considering that the device user manual indicates three possible chest electrode placements. In the second stage, a convolutional neural network is employed for detecting and classifying cardiac anomalies. The ECG signals used for training the network were obtained from publicly available arrhythmia databases, as currently, no electrocardiographic traces are available with the CMG Hi 3-Lead device and properly interpreted by cardiologists.

Overall, this thesis work demonstates good promise in the field of cardiac anomaly classification, showcasing the potential of wearable device and AI to enhance cardiac monitoring and diagnosis.

Acknowledgements

Al termine di questo bellissimo percorso, ci tengo a ringraziare tutte le persone che hanno contribuito a supportarmi (e sopportarmi) durante la stesura della mia Tesi.

In primo luogo, un ringraziamento speciale alla Professoressa Olmo per la disponibilità e la gentilezza che ha sempre dimostrato nei miei confronti e per avermi dato l'opportunità di conoscere e collaborare con una realtà così importante come STMicroelectronics.

Grazie a tutti i miei colleghi: è stato un onore potervi conoscere e spero potremo rivederci in futuro. Un ringraziamento particolare ad Alessandro, per il supporto e per la bella opportunità che mi ha dato nel poter lavorare a questo progetto.

Ultimo, ma non meno importante, grazie mille a Stéphane per tutto: se mi posso ritenere soddisfatta di questo lavoro è in particolar modo grazie a te!

A mia mamma

Table of Contents

List of Tables

List of Figures

Acronyms

ACS Acute Coronary Syndroms

AE Autoencoder

AF Atrial Fibrillation

AFl Atrial Flutter

AI Artificial Intelligence

AAMI Association for Advancement of Medical Instrumentation

ANN Artificial Neural Network

AT Atrial Tachycardia

AV Atrioventricular

BAN Body Area Network

BSN Body Sensor Network

CDSS Clinical Decision Support System

CGM CompuGroup Medical

CGM Convolutional Neural Network

CRT-D Cardiac Resynchronisation Therapy Device

CVD Cardiovascular Disease

CWT Continuous Wavelet Transform

DWT Discrete Wavelet Transform

DL Deep Learning

DNN Deep Neural Network

ECG Electrocardiogram

FC Fully Connected

FIR Finite Impulse Response

FL Focal Loss

Hi-ECG CGM Hi 3 Leads ECG

ICD Implanted Cardiac Defibrillator

IIR Infinite Impulse Response

LED Light-Emitting Diode

LMIC Low- and Middle-Income Countries

LSTM Long Short-Term Memory network

MEMS Micro-Electromechanical Systems

MIT-BIH Massachusetts Institute of Technology - Beth Israel Hospital Arrhythmia

ML Machine Learning

MLL Modified Limb Lead

MLP Multi-Layer Perceptron

NSR Normal Sinus Rhythm

PAC Premature Atrial Contraction

PPG Photoplethysmography

PVC Premature Ventricular Contraction

ReLU Rectified Linear Unit

RNN Recurrent Neural Network

RM Remote Monitoring

SA Sinoatrial

SLL Standard Limb Lead

VF Ventricular Fibrillation

VT Ventricular Tachycardia

WD Wearable Device

WHO World Health Organization

Chapter 1

Theoretical and Medical Background

This chapter aims to describe the theoretical framework in which this thesis work is situated, particularly regarding aspects such as telemedicine and telecardiology. Specifically, telemonitoring and Wearable Devices (WDs) have emerged as essential tools in the field, enabling continuous monitoring of cardiac health and facilitating early detection of abnormalities. The 'HI ECG 3-LEAD' device will then be presented: this wearable electrocardiogram (ECG) recorder is used in this work to record three electrocardiographic signal leads.

Additionally, this chapter intends to provide critical concepts related to electrocardiography and its application in the context of wearable devices, including indications on standard and modified electrode systems on the patient's body, with particular emphasis on the differences in ECG signal morphology between different electrode placements.

Finally, theoretical insights will be provided on the main cardiac anomalies primarily classified in the literature concerning Computer-Aided Diagnosis (CAD) systems for classifying pathological electrocardiograms.

1.1 Telemedicine

The World Health Organization (WHO) defines digital health as the application of digital technologies for medical purposes, encompassing the expanding use of technologies in the delivery of healthcare services. Telemedicine is closely linked to digital health as it aims to leverage the expanding role of technology to establish more efficient healthcare practices [1]. The WHO defines telemedicine as [2]: "*The delivery of health care services, where distance is a critical factor, by all health care professionals using information and communication technologies for the exchange of valid information for diagnosis, treatment and prevention of disease and injuries, research and evaluation, and for the continuing education of health care providers, all in the interests of advancing the health of individuals and their communities.*"

An example where distance has proven to be a critical factor is the outbreak of the COVID-19 pandemic, which posed unique challenges to the healthcare system: previous studies have already highlighted the crucial role of telemedicine in times of disasters and public health emergencies. With the outbreak of the COVID-19 crisis in 2020 and the significant uncertainties surrounding its spread and infectivity, the urgent need for telemedicine quickly became essential for managing patients' healthcare and, at the same time, ensuring their safety through social distancing and quarantine measures [3, 4].

This context has facilitated the development and advancement of telecommunication systems, enabling the remote transmission of medical information between patients and healthcare facilities, thereby eliminating the need for in-person visits. Furthermore, this technology has enabled remote monitoring of patients with severe illnesses, ensuring prompt emergency interventions [5].

1.1.1 Telecardiology

One of the fields of medicine where electric and electronic devices (including wearable devices) were first used for both diagnostics and therapy is cardiology: essential and relatively easy-obtainable physical signals give helpful, and sometimes vital, information about a patient's condition, such as arterial blood pressure and heart rhythm. With the advent of technology enabling the transmission of such information to remote locations, the concepts of telemonitoring and even remote treatment started to emerge [6]. It is within this context that telecardiology finds its place, as it can be defined as "*cardiology at a distance*", thus the usage of telemedicine in the cardiology field.

The current formats of telemedicine used in cardiology include [7]:

1. *Synchronous (live) applications*: as remote consultations or teleconsultation and real-time video/audio consultation;

2. *Asynchronous (store & forward) applications*: e-consultation, imaging and data storage and remote patient monitoring.

In telecardiology, the COVID-19 pandemic provided a valuable opportunity to demonstrate that the widespread adoption of digital health solutions can overcome patient-, physician- and system-related barriers to cardiac rehabilitation. Existing guidelines for implementation have supported this approach. The management of heart failure has also witnessed a renewed emphasis on monitoring and home follow-up. This involved offering explicit guidelines on establishing effective virtual visit programs, as outlined in a comprehensive document by the Heart Failure Association of America [8, 9]. Figure 1.1 illustrates what could be the optimal recommendations for delivering remote healthcare to patients, which have been derived from lessons learned during the COVID-19 pandemic.

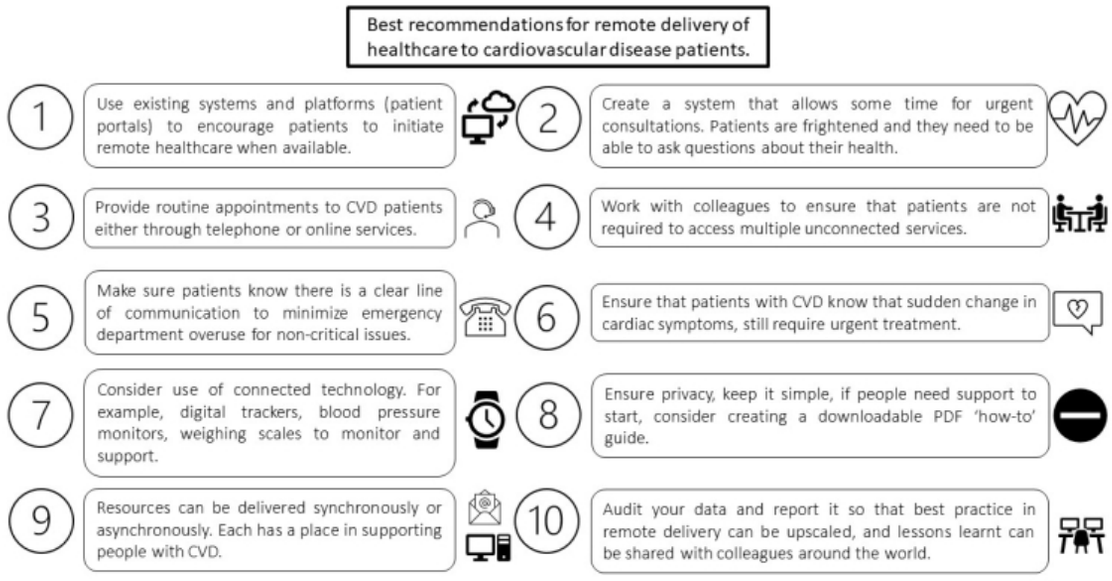

Figure 1.1: Best recommendations for remote delivery of health care to cardiovascular disease patients [8].

Finally, it is essential to perceive telemedicine-driven interventions not as standalone, one-size-fits-all solutions but as complementary additions to the existing multifaceted health interventions that can be tailored to different patient populations [10].

The critical advantages of telecardiology, as reported by [8], are:

- Improved treatment follow-up and quality of care.

- Reduction in the number of trips, resulting in time savings and an improved quality of life (reduced incidence of inappropriate shocks).
- Early detection of problems and prevention of complications;
- Decreased length of hospital stays and utilization of healthcare services (hospitalizations, consultations).
- Decreased reliance on in-person consultations while maintaining access to specialized medical advice, reducing the need for patient transportation.
- Reduced isolation for patients with cardiac implants who are located far from implant centers, particularly benefiting elderly patients with limited access to transportation.

Telemonitoring in Cardiology

The real-time transmission and reporting of electrocardiograms (ECGs) have represented a significant step forward in handling time-sensitive cardiovascular diseases, such as Acute Coronary Syndromes (ACS). Additionally, it has proven valuable in the management of chronic cardiac conditions, ensuring continuity of care on a routine basis [11].

The most direct approach to Remote Monitoring (RM) involves collecting data from already implanted devices, such as pacemakers, Implanted Cardiac Defibrillators (ICDs) and Cardiac Resynchronisation Therapy Devices (CRT-Ds), through a patient-provided transmitter and communication technology that facilitates remote data transfer. For many years, this data acquisition has been used primarily to detect technical issues such the battery level, electrode dysfunction, or insulation defects. However, in the present time, the device can also be used to assess patients' clinical status, including changes in heart rate, respiration rate, or physical activity.

Another RM approach involves using external wearable devices specifically designed for this purpose. Recent advances in chipset electronics and sensor technology have made these devices cost-effective and highly efficient.

A RM system via a wearable device typically comprises four elements: the wearable device itself, a network infrastructure, a communications interface to allow data transfer, and an analytics platform capable of integrating large amounts of data and identifying critical information [6]. Figure 1.2 shows the structure of a telemonitoring system for remote monitoring of arrhythmia and heart failure patients.

The TeleCheck-AF project is an example of RM implementation in telecardiology, developed during COVID-19 [13]. Maastricht Medical University Centre developed a mobile health (mHealth) intervention unit specifically designed to

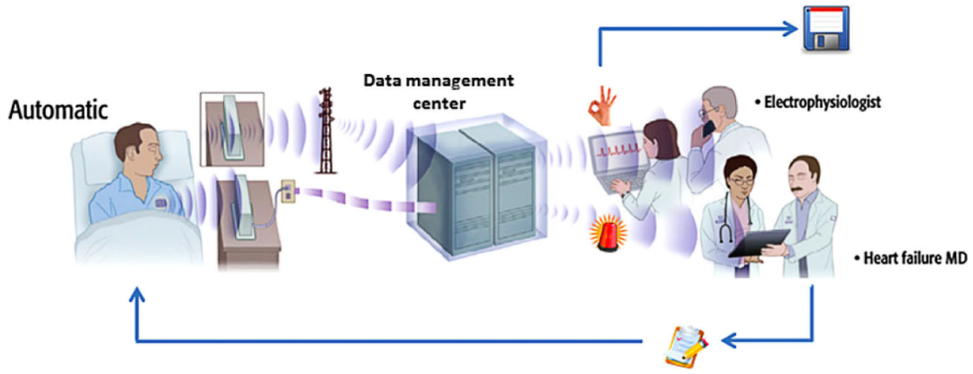

Figure 1.2: Telemonitoring system for remote monitoring of arrhytmia and heart failure patients [12]. The data management center is responsible for the integration of data acquired from the patient.

facilitate Atrial Fibrillation (AF) teleconsultations. This initiative aimed to ensure uninterrupted and comprehensive management of AF through teleconsultation during the pandemic. TeleCheck-AF consisted of three main components:

1. A structured teleconsultation ("*Tele*").
2. An app-based on-demand heart rate and rhythm monitoring infrastructure ("*Check*").
3. Comprehensive AF management ("*AF*").

The infrastructure to monitor heart rate and rhythm is based on a CE-marked mobile phone app, which uses photoplethysmography (PPG) technology through the built-in camera of the smartphone, allowing semi-continuous heart rate and rhythm monitoring of AF patients both before and during the teleconsultation.

During the pandemic, this strategy was expanded to various European countries, with great satisfaction from both physicians and patients: more than 80% of centres reported no problems during the implementation of the TeleCheck-AF monitoring system, and the majority (94%) of the recruited patients agreed that the app was easy to use [8, 14].

Wearable Devices and their application in Telemonitoring

Wearables, *wearable devices*, or *wearable technology* refer to small electronic and mobile devices or computers with wireless communications capability. These devices can be integrated into gadgets, accessories, or clothes that can be worn directly on

the human body. In some cases, wearables may also include invasive versions such as microchips or smart tattoos [15].

Equipped with sensors and advanced technologies, these devices enable the storage and transmission of biological signals or parameters (like heart rate, oxygen saturation, respiratory rate, and electrocardiographic signals), as well as parameters related to the movement and activity status of the user [16]. By continuously collecting and transmitting this information and data to healthcare providers, wearable devices facilitate remote patient monitoring and early detection of abnormalities, allowing for timely interventions and personalised treatment plans.

Different Wearable Devices (WDs) can also be connected to each other, as happens in Body Area Networks (BANs). In BANs, communication takes place entirely within or in the proximity of the human body. In cardiac monitoring, when continuous deployment is required, sensors embedded in ICDs, injectable cardiac monitors, implantable loop recorders or pacemakers are used. On the other hand, for shorter periods of monitoring (like 2 to 4 weeks), patches, i.e., wearable stick-on monitoring devices worn on the torso, provide continuous and looping ECG recording. In addition to this, for intermittent symptom-triggered monitoring, touch-activated electrodes configured for smartphones can be used.

As depicted in Figure 1.3, in a typical architecture of a patient monitoring system implementing wearable sensors technology, on-body sensors establish wireless communication with stationary devices (such as wireless local area network) or wearable gateway devices (such as mobile phones) to transmit sensor data to remote locations.

The measurements obtained from wearable sensors can be either stored locally on the wearable monitoring device itself for later transmission or, alternatively, they can be directly transmitted (for example, over the public mobile phone network) to a medical centre where patient's data can be accessed online using the Internet independently of the patient's physical location. Lastly, it is important to consider that reducing battery consumption through power scavenging, also known as "energy harvesting", from on-body sources or the environment can be a potential solution to enhance battery life, especially for implantable sensors. In fact, the advancement of low-power measurement and transmission systems plays a vital role in the successful development of wireless Body Sensor Network (BSN) systems [17].

1.1.2 CAD systems for heart diseases

Cardiovascular diseases (CVDs) are disorders affecting the heart and the blood vessels, including coronary heart disease, peripheral arterial disease, cerebrovascular

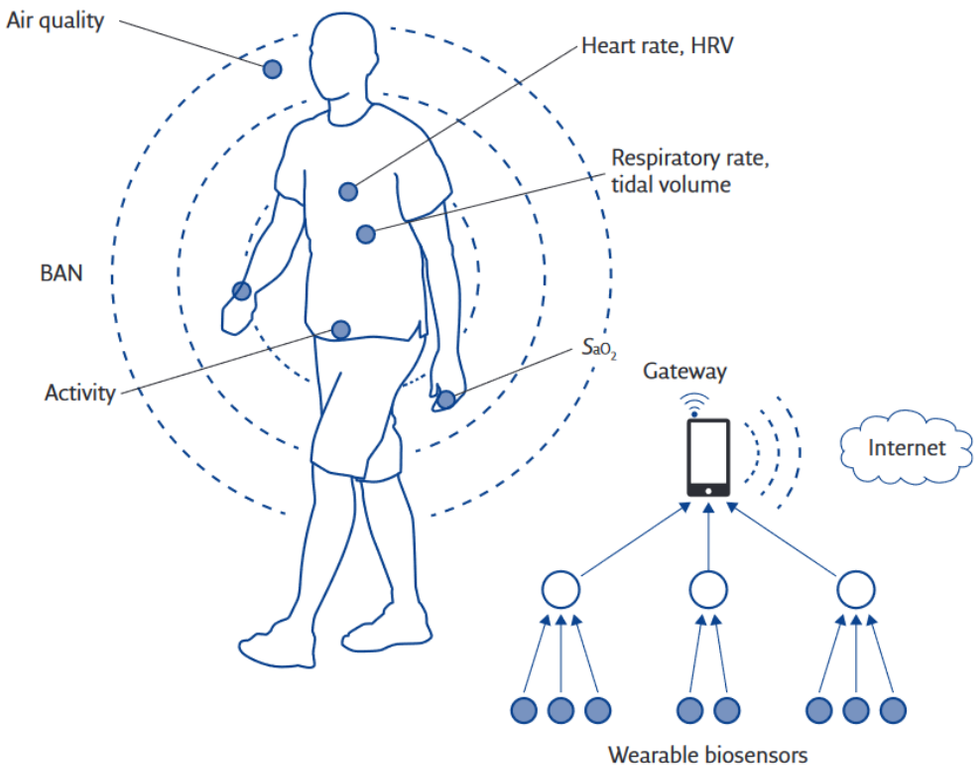

Figure 1.3: Architecture of a patient monitoring system using wearable sensors [17]. Wearable sensors communicate through wireless technology with stationary or wearable gateway devices to relay sensor data to remote locations.

disease, rheumatic heart disease and other conditions [18]. Among the diverse spectrum of various cardiovascular abnormalities, this thesis work will focus specifically on arrhythmia, the most prevalent heart condition, which refers to any irregularity in the rate or rhythm of a person's heartbeat. During an arrhythmia, the electrical impulses may be excessively rapid, too slow, or irregular, leading to irregular heartbeats [19].

According to the WHO, CVDs are the primary cause of death globally, accounting for approximately 17.9 million deaths yearly. More than 80% of CVD deaths are attributed to heart attacks and strokes, and about one-third of these deaths occur prematurely in individuals under the age of 70. Notably, over 75% of these deaths occur in Low- and Middle-Income Countries (LMICs) [18]. From an economic perspective, it is estimated that CVDs incur an annual cost of approximately €169 billion in the European Union. Of this amount, 62% accounts for direct costs within the healthcare system, while the remaining portion represents productivity losses and informal care [20]. It is reported that identifying individuals at the

highest risk of CVDs and the insurance they receive for appropriate treatment can prevent premature deaths [18].

Standard diagnostic tests for CVDs include ECG, echocardiogram, blood work, ambulatory monitoring, cardiac computed tomography and magnetic resoncance imaging, stress test, cardiac catheterisation etc. However, accurate diagnosis requires analysis and integration of much laboratory data and patient information. Integrated data analysis through the manual procedure can be complex and time-consuming, and the diagnostic effectiveness depends on physicians' knowledge and experience, which can sometimes lead to misdiagnosis [21].

Another point to consider is that there is often a low physician-to-patient ratio in low-resource clinical settings compared to developed nations. Furthermore, even when such physicians are accessible, they often operate in an environment that lacks high-quality expertise and medical infrastructure. Combined, these phenomena contribute to an overburdened healthcare system that fails to adequately meet the community's needs and can result in untreated patients or patients receiving inadequate or substandard treatment [22]. Acknowledging that over-burdened healthcare systems are not just limited to low-resource clinical settings is essential. Indeed, health systems in developed nations, such as the National Health Service in the United Kingdom, are recognising this reality, particularly in the wake of the COVID-19 pandemic [23].

To mitigate this burden, researchers and healthcare professionals are focusing on systems that assist healthcare professionals in their daily tasks, particularly in the decision-making phase [22]. In this context, Computed-Aided Diagnosis (CAD) is introduced. CAD is defined as: "*A diagnosis made by a physician who uses the output from a computerised medical data analysis as a second opinion in detecting lesions, assessing disease severity, and making diagnostic decisions*". CAD is expected to improve physicians' diagnostic capabilities and reduce the time required for accurate diagnosis [24].

Artificial intelligence (AI), which simulates human intelligence in machines programmed to replicate human thoughts and actions, holds promise in assisting clinicians in diagnosing and managing CVDs through extensive data analysis. Clinical Decision Support Systems (CDSS) based on AI can be developed using traditional Machine Learning (ML) algorithms or Deep Learning (DL) algorithms that leverage large datasets and complex algorithms for model training [21].

The design of an ML-based CAD system for cardiovascular diseases is structured into an *offline* and an *online* system. The purpose of the offline system is to evaluate and select the best algorithm structure, which is then employed in the online one as a diagnosis support system. Both the online and offline systems can be modelled as an algorithm chain, as shown in Figure 1.4. The algorithm

chain starts with pre-processing and feature extraction[1]. As such, the classification outcomes constitute the decision support for medical specialists [25].

On the other hand, CAD systems can also be implemented in a telemonitoring system to perform automatic ECG classification. In this scenario, it is important to consider that the computational complexity associated with these systems may lead to increased power consumption. Therefore, exploring solutions that involve low-complexity algorithms becomes necessary, allowing for implementation in WDs [26].

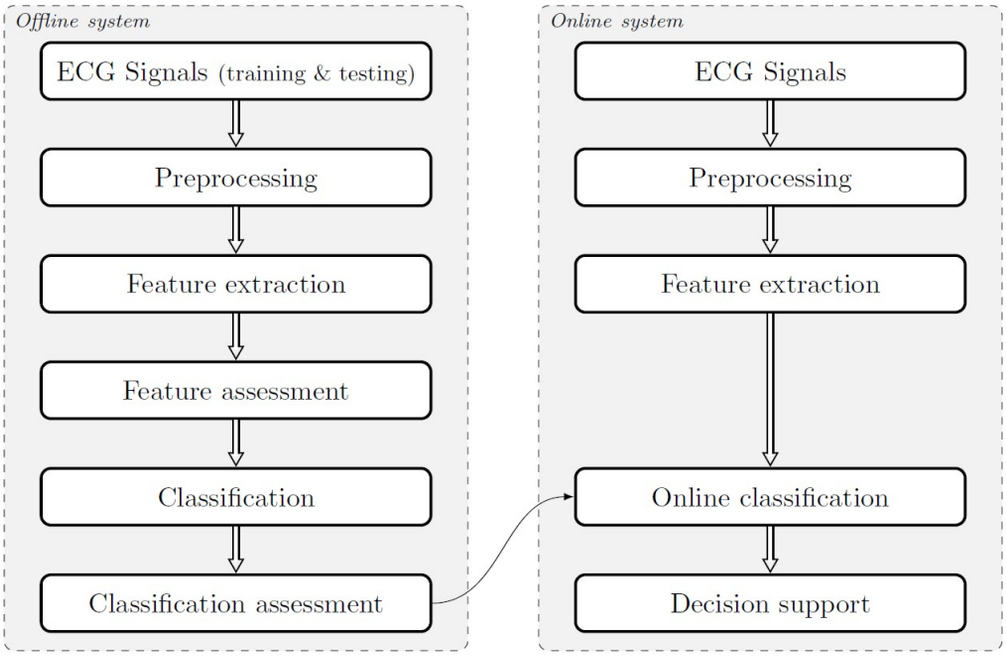

Figure 1.4: Block Diagram of ML-Based CAD system for cardiovascular diseases [25]. It is constituted of two main blocks: online and offline systems.

1.2 CGM HI 3 LEADS ECG

In this paragraph, the Hi 3 Leads ECG CGM device will be presented, and its use within this thesis work to acquire ECG signals and other physiological parameters will be described.

[1]As better described in paragraph 2.2, feature extraction is not required in DL-based CAD systems.

1.2.1 Device overview

CGM Hi 3 Leads ECG (Hi-ECG) is a CE-mark wearable ECG recorder commercialised by CompuGroup Medical (CGM) and developed in collaboration with STMicroelectronics.

This battery-powered medical device is designed to be applied with adhesive electrodes (patches) on the patient's chest to acquire, record, and transmit one to three channels of ECG and other parameters (such as body position, subject's activity status and Micro-Electromechanical Systems - MEMS - data) to an external device, using Bluetooth technology. Due to its simplicity and ease of use, absence of wired connections, and battery life of over 24 hours, this device is suitable for various applications, as reported by CGM Telemedicine, including [27]:

- *Tele Holter*: remote Holter up to 30 days with web-based platform[2] data transmission and dedicated advanced holter analysis software.
- *Telemonitoring*: remote monitoring up to 7 days with online transmission and data analysis in a web-based platform by using an integrated and dedicated algorithm.
- *Tele ECG*: remote rest ECG examination when symptoms occur or on scheduled sessions, with online transmission and data analysis in web-based platform.

The Hi-ECG device sensor suite includes, in addition to the three electrodes, a MEMS triaxial accelerometer dedicated to the analysis of physical activity and body position. As shown in Figure 1.5, two of the electrodes are integrated into the main body of the device, while the third electrode is connected to the main body through a cable. The three electrodes perform differential measurements, where a single-lead ECG is obtained for each pair. Therefore, a total of three bipolar ECG leads can be recorded. The resolution of each ECG channel is 12 bits, ranging from -6.6 mV to +6.6 mV; the default sampling frequency is 128 Hz.

The main block of electronic components comprises three differential amplifiers (for each signal channel), three Light-Emitting Diodes (LEDs), a microcontroller, a Bluetooth module and a battery. The Bluetooth module connects Hi-ECG with a host device (e.g., a smartphone, tablet, or computer) to periodically transmit all the acquired signals. The internal battery is a lithium-ion one (3 VDC with 250 mAh capacity). The LEDs provide information on the battery charge status, the

[2]The web platform is *CGM CARE MAP*, a web solution that allows healthcare personnel to always keep in touch with their patients by monitoring not only cardiac rhythm but also several vital parameters (oxygen saturation, blood pressure) which help to have a complete clinical picture of the patient's health.

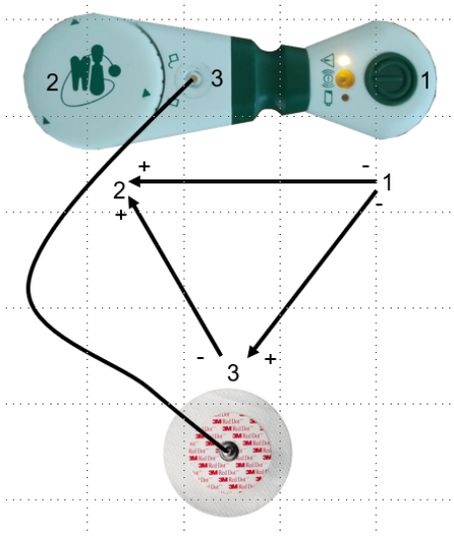

Figure 1.5: CGM HI 3 LEADS ECG medical device [27]. The polarity of the three electrodes is also shown.

current operational mode of the device (engage, streaming and monitoring), and warnings on the incoming signals (such as the detachment of one or more electrodes). The adopted microcontroller is the STM32L451, based on the high-performance Arm® Cortex®-M4 32-bit RISC core operating at frequencies up to 80 MHz and embedding up to 512 Kbytes of flash memory and up to 160 Kbytes of SRAM [28].

1.2.2 Use of the Device in the thesis work

In this thesis work, Hi-ECG is used to acquire and transmit three channels of ECG signal and accelerometric data on the three axes and the body posture level to a personal computer. The body posture level is a parameter that indicates whether the user is in an upright, seated or lying position. These data have been processed in MATLAB version R2021a and Python version 3.10 to classify cardiac anomalies using a deep learning–based approach.

The signals are acquired by positioning the device's electrodes according to the instructions provided in the user manual. Specifically, three types of electrode placement - *configurations* - are indicated, as shown in Figure 1.6.

- *Configuration #1* (indicated in the user manual as '*preferred electrodes position*'): The main body of the device is vertically applied (with the power button facing upwards) at the mid-sternal level, with the upper electrode positioned along the axillary line. The movable electrode is placed at the level of the left inframammary fold.

- *Configuration #2*: The main body of the device is horizontally applied (with the power button facing right) at the level of the axillary and mid-sternal line. The movable electrode is applied at the level of the left inframammary fold.
- *Configuration #3*: The main body of the device is horizontally applied (with the power button facing left) at the level of the xiphoid and right para-sternal line. The movable electrode is placed along the axillary and left para-sternal line.

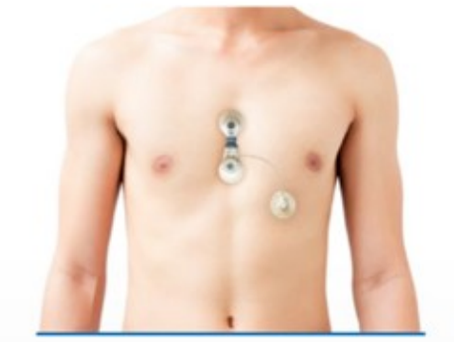

(a) Configuration #1

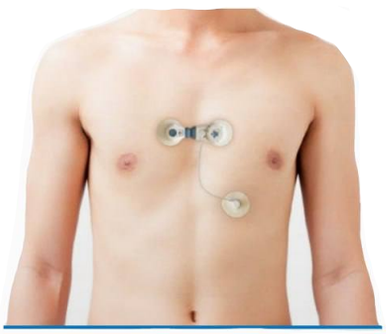

(b) Configuration #2

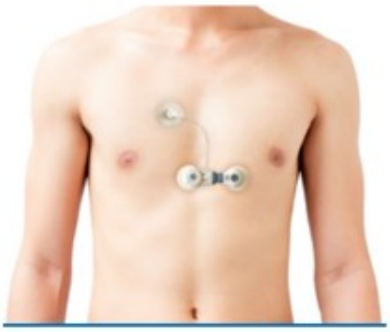

(c) Configuration #3

Figure 1.6: Electrode Placements of Hi-ECG proposed by the user manual [27].

It should be noted that Hi-ECG is intended to be positioned by the users themselves, and therefore, there is a possibility of electrodes misplacement. In this thesis work, we will also address electrode placement scenarios where the user has incorrectly positioned the main body of Hi-ECG. The configurations characterised by misplacement of the main body electrodes will be referred to as:

- Configuration #1 – Misplacement;

- Configuration #2 – Misplacement;
- Configuration #3 – Misplacement;

1.3 Electrocardiography

This paragraph will briefly describe the basic principles of electrocardiography, with a specific focus on Einthoven's bipolar leads, as the ECG signals acquired with the Hi-ECG device also correspond to bipolar leads. The information presented here is derived from the books "*Fisiologia Cardiovascolare*" by Prof. L. Agnati [29] and "*In Quantitative Human Physiology*" by Prof. J. Feher [30], which can be referred to for a more detailed description.

1.3.1 Electrophysiological Characteristics of the Heart

While the electrical phenomena occurring at the level of individual cells are detected using intracellular microelectrodes inserted into the cardiac cell under examination, the overall electrical phenomena of the heart are recorded using macroelectrodes placed on the body's surface. These phenomena depend on the depolarisation and repolarisation of different parts of the myocardial mass, and their recording over time constitutes the ECG.

The study of the propagation of the electrical event within the cardiac mass is fundamental to interpreting the ECG and analysing cardiac abnormalities. The ECG waveform has a morphology that is dependent on this propagation. Alterations in cardiac tissue result in changes in the pathway and magnitude of the excitation wave, leading to modifications in the ECG morphology. Therefore, the diagnostic value of electrocardiography becomes evident.

The excitation wave arises in the Sinoatrial (SA) Node, located in the terminal groove on the posterior side of the heart, where the superior vena cava joins the right atrium. It exhibits an unstable membrane potential due to a spontaneous decrease in potassium ion permeability, resulting in progressive resting potential depolarization. When the membrane potential reaches approximately -50 mV, calcium ions (Ca^{++}) enter the cell, initiating the onset of the action potential. This action potential is transmitted in all directions within the atrial cells at a 1.0-1.2 m/s velocity. Since the SA node controls the heart rate, it is called the primary pacemaker.

After approximately 0.1 seconds, the impulse reaches the Atrioventricular (AV) node, the region where excitation reaches the ventricles. It is located posteriorly on the right side of the interatrial septum, near the opening of the coronary sinus.

The excitation propagates through the AV node at a 0.02-0.05 m/s speed. This delay allows for complete atrial contraction before the activation of the ventricular myocardium. If the transmission through the AV node were interrupted, the atria and ventricles would contract independently and not in a coordinated manner.

At this point, the excitation propagates along the His bundle with a velocity of approximately 1.2 m/s. After a short course in the interventricular septum, the His bundle divides into the right bundle branch and the left bundle branch. In these branches, the velocity of the excitation wave is approximately 2.0 m/s. These branches are located beneath the endocardium on their respective sides of the septum. They extend towards the apex of the corresponding ventricle, loop around it, and then return towards the base of the heart. Throughout their course, these branches give rise to fibres that penetrate the ventricular myocardium, forming the Purkinje network.

In the terminal endings of the fibres, the velocity of the wave decreases proportionally to the diameter of the involved fibres. The base of the ventricles is the last part to be activated.

Figure 1.7 shows the sequence of cardiac activation schematically.

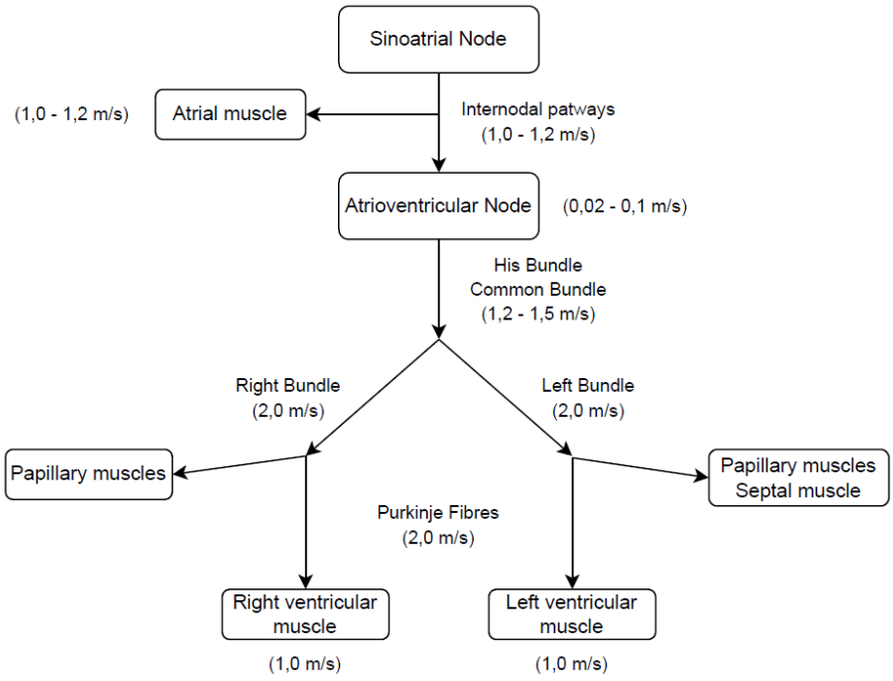

Figure 1.7: Initiation and propagation of excitation in the myocardium, modified from [29]. The propagation velocities of the excitation wave in each structure are indicated in parentheses.

1.3.2 Recording of Cardiac Electrical Events on the Body Surface

Recording the electrical events associated with the propagation of the excitation wave in the cardiac mass on the body surface constitutes the ECG, from which various information can be derived, including any alterations in the onset and propagation of the electrical phenomenon. This information is obtained by analysing the shape, amplitude, and temporal course of the potential variations that originate at the heart level and can be recorded using macroelectrodes located on the body surface.

To evaluate these aspects, it is essential to understand the physical principles of electrocardiography. Some key points are described in the following paragraph.

Heart as electric dipole

As excitation of the cardiac muscle is conveyed through the myocardium, the electrical state of the muscle fibres differs from place to place. During the conduction of the action potential, some parts of the muscle are depolarised, and others are not. This produces the equivalent of an electrical dipole, as is depicted in Figure 1.8.

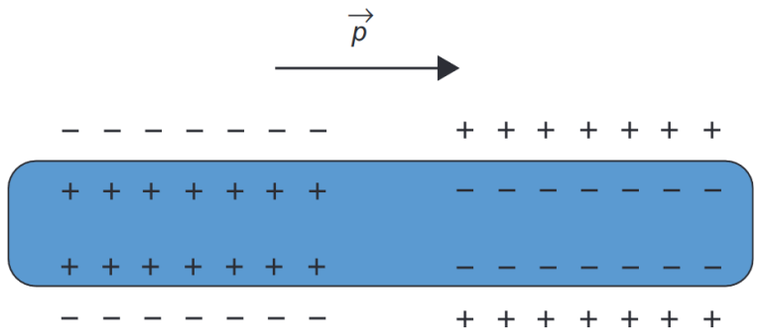

Figure 1.8: Equivalent dipole of the heart muscle during partial acrivation [30]. .

The dipole moment is given as:

$$\vec{p} = q^{+} \cdot \vec{d} \tag{1.1}$$

Where:

- d is a vector pointing from q^{-} (negative pole) to q^{+} (positive pole).
- q^{+} is the magnitude of charge separated by distance, d.

An electric potential (V) surrounds the dipole, and measured in a certain point P, it is given approximately as:

$$V = \frac{p \cos \theta}{4\pi\varepsilon r^2} \tag{1.2}$$

Here:

- p is the absolute value of the dipole momentum.
- θ and r are the polar coordinates, with respect to the dipole, of the point from where the electric potential is measured.
- ε is the relative permittivity, which describes the electrical characteristics of the tissue interposed between the dipole and the point P.

The electric dipole of the heart produces an electrical potential throughout the thorax and is projected onto the skin.

Bipolar Leads

Building upon the considerations presented in the previous paragraph, Einthoven (1860-1927) recorded potential differences on the body surface, resulting from the heart's electrical activity, using specialised electrodes and a highly sensitive galvanometer. His pioneering work in the measurement and interpretation of the ECG earned him the Nobel Prize in Medicine and Physiology in 1924.

He proposed three ways of placing electrodes on the body surface (known as '*leads*') and provided a theoretical interpretation of the potential differences recorded from these leads.

The three leads proposed by Einthoven are bipolar, meaning that one electrode acts as the positive electrode while the other acts as the negative electrode. These leads involve placing the electrodes on the two upper limbs and the left leg. The Bipolar Lead Combination is summarised in Table 1.1.

Lead	Electrode +	Electrode -	Signal combination	Geometrical angle
I	LA	RA	LA-RA	0°
II	LL	RA	LL-RA	+60°
III	LL	LA	LL-LA	+120°

Table 1.1: Bipolar Lead Combination

Einthoven believed these positions could be considered vertices of an equilateral triangle and that the heart, represented by the vector of the equivalent dipole, was located at the centre of this triangle. The voltage differences between the different electrodes can be measured in three combinations:

Left Arm - Right Arm = LEAD I

Left Leg - Right Arm = LEAD II

Left Leg - Left Arm = LEAD III

The voltages recorded at these bipolar leads are not independent. Because of Kirchoff's voltage law, which states that the voltage drop around any closed circuit is zero, we have the following:

$$\mathrm{I} + \mathrm{III} = \mathrm{II} \tag{1.3}$$

Where I, II and III are the voltage differences across leads I, II and III, respectively. So, the voltage in the third bipolar lead can always be calculated from the other two.

The voltages recorded in each of the bipolar leads at any instant are equal to the projection of the heart's electric dipole (cardiac vector) at that instant onto the bipolar lead.

Figure 1.9 represents the instantaneous electrical vector due to ventricular depolarization within the Einthoven triangle.

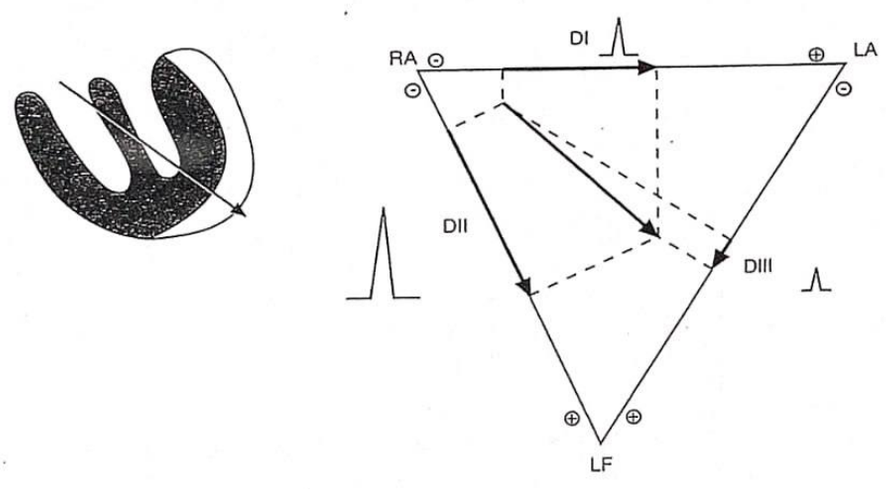

Figure 1.9: Equivalent electrical vector, modified from [29]. Partially excited ventricular mass representation with equivalent electrical vector (left panel). Placement within the Einthoven triangle of the electrical vector illustrated in the left panel and projections of the vector along the lead lines (right panel).

A deflection above the isoelectric baseline (positive wave) is recorded if the direction of the cardiac vector projection is in the same direction as the reference line of the lead; otherwise, a negative wave is observed. The resulting projections of the electric dipole moment onto the limb leads produces a record of voltage that

varies with time – the scalar electrocardiogram. The ECG is typically produced at a chart speed of 25 mm/s on a scale of 1 mV/cm.

An example of an ECG signal on lead II ($V_{LL} - V_{RA}$) is reported in Figure 1.10.

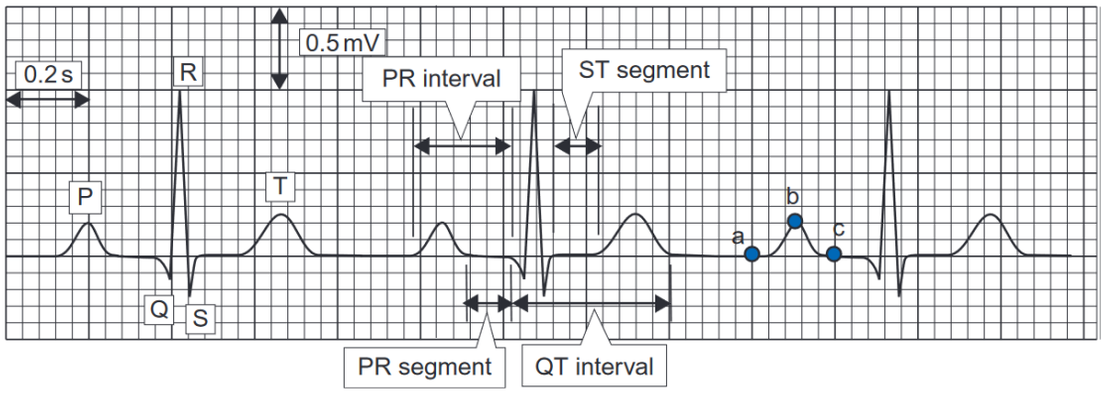

Figure 1.10: Typical appearance of the ECG on lead II [30]. The signal consists of several named electrical events, beginning with the P wave. The P wave is the first electrical event of the heart cycle and corresponds to the depolarization of the atria. The QRS complex corresponds to the depolarization of the ventricles. Buried within it is the electrical signature of the repolarisation of the atria. The T wave corresponds to the repolarisation of the ventricles. It is upright because of the sequence of repolarisation of different parts of the ventricles.

In addition to the three bipolar leads of Einthoven, which allow exploration of the electrical activity of the heart in the frontal plane, the standard ECG includes nine other leads (three augmented unipolar leads by Goldberger and six unipolar leads by Wilson), for a total of twelve leads. However, in this thesis work, the focus will only be on the bipolar leads as the Hi-ECG device records these kinds of leads, as described in paragraph 1.2.

1.3.3 General Theory of heart vector projection

The description provided in the previous paragraph indicates that the values recorded on leads I, II, and III at any time are the result of the electric dipole moment of the heart at that time. Yet, what is measured are the voltages on these leads, while the electric dipole moment remains unknown. Still, it is possible to approximately reconstruct the direction and magnitude of the electric dipole moment from these measured voltages, but this cannot be done by ordinary vector addition. This is because the vectors I, II, and III are *projections* of the heart's dipole moment onto axes that are not orthogonal. In fact, in orthogonal coordinate systems, a vector parallel to one coordinate has no components in the direction of

any other coordinate. In contrast, in the triangular coordinate system, a vector along one axis does have components along both other axes. This means that the electric dipole can be reconstructed only by reversing the projection onto the axes, as described in Figure 1.11.

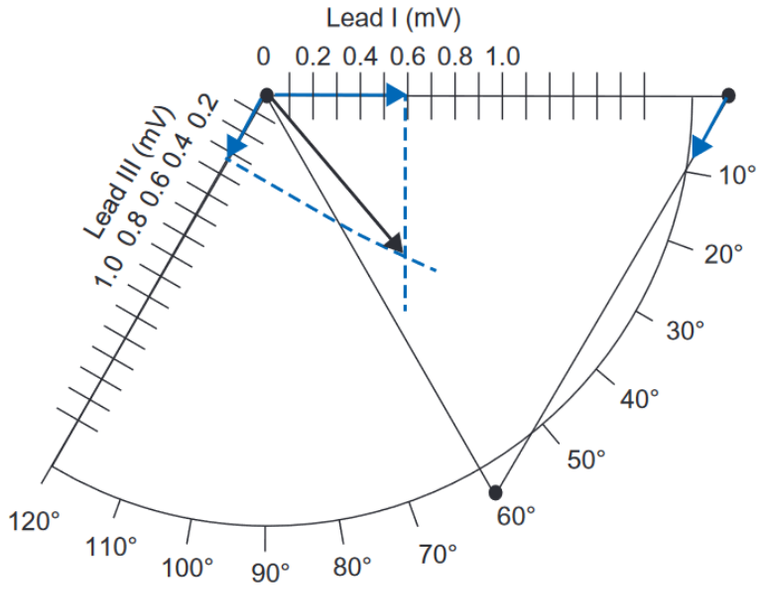

Figure 1.11: Reconstruction of the heart's electrical dipole from leads I and III [30]. A vector whose magnitude is the voltage of lead I is drawn with its starting point at the origin and its end on the lead I axis. A second vector equal to the voltage of lead III is drawn the same way but oriented on an axis parallel to the lead III axis and starting at the origin. The electric dipole extends from the origin to the intersection of the two lines drawn perpendicular to the axes at the ends of the lead I and lead III vectors. The electric dipole of the heart obtained this way pertains to the time leads I and III were measured. This dipole has a magnitude (its length in the same units as for the two lead axes) and a direction. The direction is usually given in degrees using the convention shown.

The size and magnitude of the cardiac electric dipole continuously change as excitation spreads through the heart. In Figure 1.12, the electric dipole is depicted in one specific state of the heart, mainly corresponding to the depolarization of the ventricles.

The cycle shown in Figure 1.13 is elongated toward the vector produced upon depolarizing the thick left ventricular wall. This elongation defines an *electrical axis* of the heart, which generally should relate to the heart's anatomical position within the thorax.

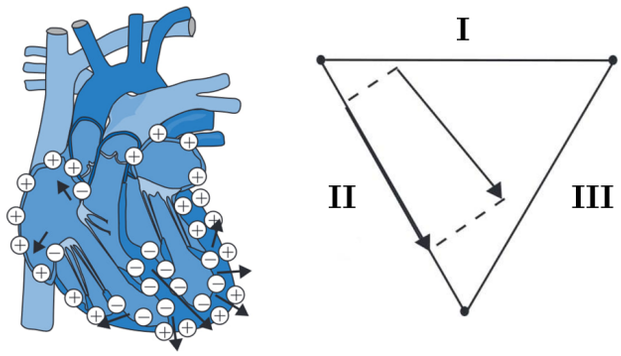

Figure 1.12: Representation of the cardiac electrical dipole during ventricular depolarization and its projection along lead II [30].

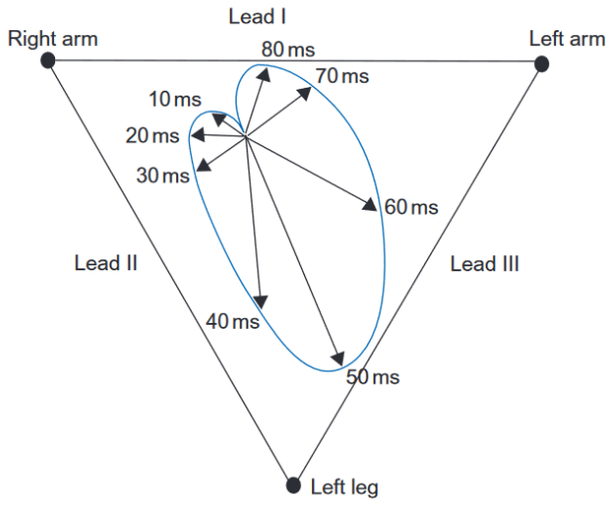

Figure 1.13: Approximate changes in the direction and magnitude of the cardiac dipole during ventricular excitation [30]. The dipole projection on the different leads produces the ECG and accounts for different shapes of the QRS complex recorded in leads I, II, and III.

The electrical axis is most easily defined as the cardiac electric dipole at the peak of the curve traced out in Figure 1.13. Because of its tilt, however, the projection of the vector tracing this curve peaks at different times on the lead I and lead III axes. This is why the electrical axis can be determined from lead I and lead III ECGs using the voltage of the R wave and selecting the resulting cardiac dipole as described in Figure 1.11.

The electrical axis is typically oriented about 60° below the horizontal but varies

widely from -30° to 110°. The electrical axis depends in part on the anatomical orientation of the heart: a tall, thin person generally would have a more vertically oriented electrical axis than a short, stout person. Moreover, the heart lies within a tough fibrous sac, the pericardium, which is fused to the diaphragm. So, during inspiration, the diaphragm moves downward to expand the thoracic cavity, pulling the heart into a more vertical orientation. Thus, the electrical axis typically becomes more vertical during inspiration and more horizontal during expiration.

The electrical axis also depends on the relative contributions of the right and left ventricles to the ECG. Hypertrophy of the left ventricle shifts the axis, causing left axis deviation, whereas hypertrophy of the right ventricle is associated with right axis deviation.

Assumptions underlying the Theory of Einthoven

The theory of Einthoven and the projection of the cardiac vector onto the frontal plane are based on certain assumptions:

- The chest is a spherical and homogeneous conductor, and the heart is at the sampling volume's centre.
- The cardiac electrical forces are generated at the centre of the conductor, and a single vector can represent the resultant of these forces at any given moment.
- The limb-trunk junction points (vertices of the Einthoven Triangle) are the vertices of an equilateral triangle inscribed in the longitudinal section of the spherical chest.

It is clear, therefore, that the theory formulated by Einthoven is applicable when the electrodes for acquiring bipolar leads are positioned on the limbs. This does not apply to the electrode placements indicated in the user manual of the Hi-ECG device, as described in paragraph 1.2.2.

1.4 Electrodes Positioning in Wearable Technologies for Cardiac Monitoring

As mentioned in the previous paragraph, there are several defined and established configurations of electrodes for measuring electrocardiogram signals in standard, comparable formats that facilitate the diagnosis of cardiac conditions. The Standard 12-Lead Configuration, depicted in Figure 1.14, enables the acquisition of an ECG signal in 12 leads (or channels): three bipolar limb leads (I – II – III), three unipolar limb leads (aVR – AVL – aVF), and six unipolar precordial leads (V1–V2–V3–V4–V5–V6).

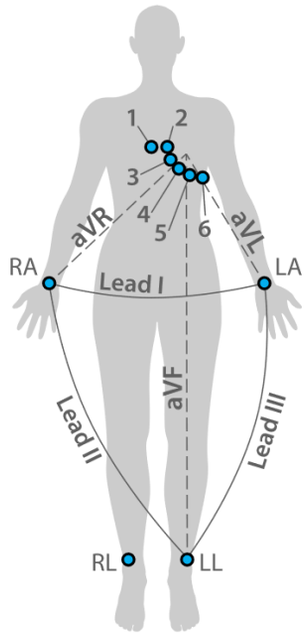

Figure 1.14: Standard 12-Lead configuration [31].

However, medical configurations have several limitations, including the use of a large number of electrodes and their uncomfortable placement, as well as limited movement and duration of the recordings [31]. This contrasts with the requirements of a cardiac monitoring system, where patient comfort needs to be considered, especially for long-term recordings that may involve physical activity. In this context, non-standard electrode placements have been proposed in the literature, specifically designed for wearable devices [31, 32, 33].

Furthermore, several studies have demonstrated that modification of the electrode placement, compared to the standard configuration, significantly alters the waveforms and axes of the electrocardiographic signal [34, 35]. Especially regarding the bipolar limb leads, deviations from the standard electrode placement may invalidate the assumptions underlying Einthoven's theory, as summarised in paragraph 1.3.3, making the interpretation of the electrocardiogram difficult, particularly for the detection of cardiac abnormalities.

In the next paragraph, we will focus on the configuration called 'Modified Limb Lead' often used in telemonitoring systems. Additionally, the signals from the MIT-BIH Arrhythmia Database, described in more detail in paragraph 2.4.1 and used in a part of this thesis, were acquired using a Holter device positioned according to this specific configuration [36].

1.4.1 Modified Limb Lead ECG system

The Modified Limb Lead ECG system involves placing the electrodes for the bipolar leads on the patient's chest, as shown in Figure 1.15, to enhance the user's comfort while wearing the portable electrocardiograph, particularly during physical activity.

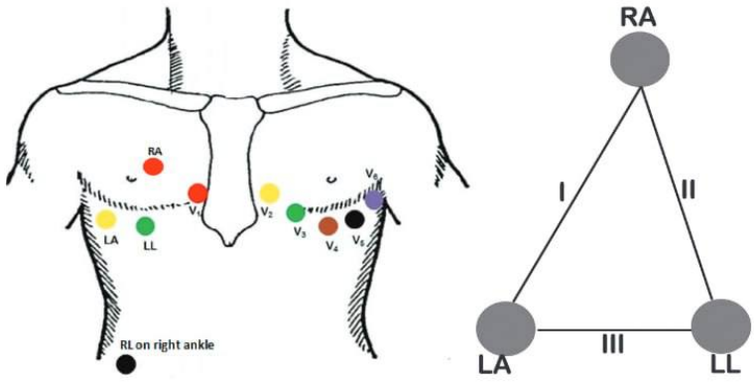

Figure 1.15: Placement of modified limb on the torso [37]. The polarity of the right arm electrode is negative, while the polarity of the left arm and left leg electrodes is positive. The conventional terminology is still used; for example, the potential difference between the right arm electrode (RA) and left arm electrode (LA) is still referred to as lead I, II, and III. The positions of the standard precordial electrodes V1-V6 remain unchanged compared to the Standard Limb Lead system.

Particularly:

- The right arm electrode is positioned in the third intercostal space on the subject's right side, slightly to the left of the mid-clavicular line.
- The left arm electrode is positioned in the fifth intercostal space on the subject's right side, slightly to the right of the mid-clavicular line.
- The left leg electrode is placed along the mid-clavicular line in the fifth intercostal space.
- The right leg electrode used as reference is placed on the subject's right ankle.

Several studies in the literature, including the one by Jayaraman et al. [37], have examined the differences between the Standard Limb Lead (SLL) and the MLL ECG system. In their study, 60 male subjects in sinus rhythm, aged between 25 and 58 years, with normal body composition, were recruited from the outpatient department of the Rajiv Gandhi Government General Hospital of Chennai. ECG signals were recorded from these subjects using the MLL system and then analysed.

Specifically, ECG values such as frontal plane axis (P, QRS, and T), amplitudes of each waveform (R, S, and T), and ST segment amplitudes (ST_a) level were all recorded and stored for further analysis. Compared to the conventional 12-lead ECG, the MLL configuration led to noticeable alterations in the frontal plane axis of the P, QRS, and T waves. The modifications in the placement of the limb electrodes significantly impacted the axis measurements, particularly in relation to the QRS and T wave axes. The distribution of these axis changes between the standard and modified positions can be observed in Figure 1.16.

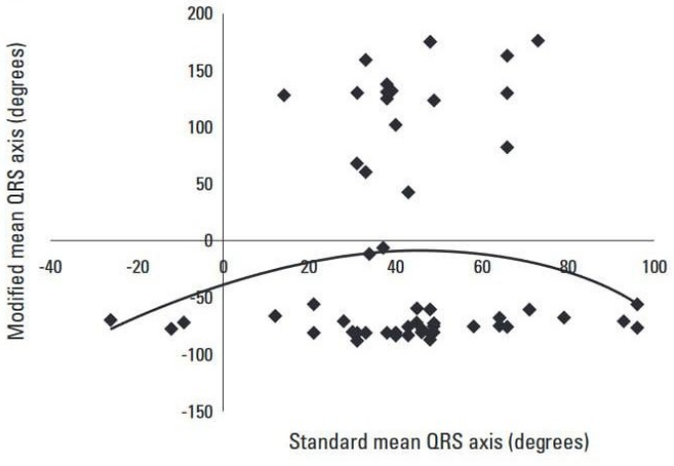

(a) Distribution of mean QRS wave axis in standard and modified position and curvilinear regression calculated from the axis values

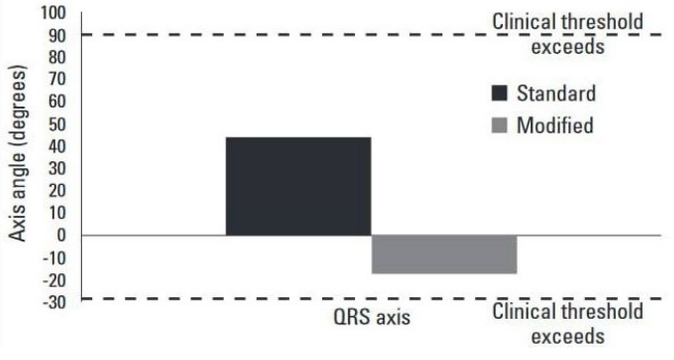

(b) Mean electrical axes of the QRS complex in standard and modified position showing the thresholds for clinical abnormality

Figure 1.16: Comparison between Standard Limb Lead and Modified Limb Lead systems [37].

As a result of the alterations in the placement of the limb electrodes, significant

shifts in the frontal plane axis were observed, leading to substantial changes in amplitude in the frontal plane leads. The modification of the limb electrode also produced changes in the (ST_a) in the frontal plane leads. To summarise, this study demonstrated that the deviations in the QRS axis caused false-positive changes in the frontal plane axis of the ECG. These findings highlight the possibility of incorrect interpretation of heart diseases based on these altered axis measurements.

1.5 Pathological electrocardiogram

In the following paragraph, we will discuss the major abnormalities that characterise pathological ECG, with a particular focus on the abnormalities that are most commonly classified by CAD systems described in the literature. For more information on cardiac abnormalities, we refer to the sources used to write this paragraph which are the books '*Fisiologia cardiovascolare*' by Prof. L. Agnati [29] and '*Advances in Cardiac Signal Processing*' by Dr. S. Acharya [38].

Cardiac abnormalities in an electrocardiogram are commonly classified into two fundamental categories:

1. *Cardiac rhythm abnormalities (or arrhythmias)*: These involve alterations in the orderly sequence and/or normal frequency of cardiac electrical events.

2. *Morphological abnormalities of the electrocardiographic waveform*: These abnormalities do not necessarily indicate changes in cardiac rhythm but are characterised by alterations in the shape, duration, or amplitude of specific components of the ECG waveform.

In the literature, the CAD systems for classifying pathological electrocardiogram focus on arrhythmias [25].

Arrhythmias may be more readily understood by categorising them in the following manner, based on where the pacemaker region (which normally is in the SA node) is located:

- Sinus Node Arrhythmias – pacemaker in the SA node.

- Atrial Arrhythmias – pacemaker in the atria.

- Junctional Arrhythmias – pacemaker in AV junction.

- Ventricular Arrhythmias – pacemaker in the bundle branches, Purkinje network, or ventricular myocardium.

- Atrioventricular Blocks – impulse blockage in the AV junction.

- Bundle Branch and Fascicular Blocks – impulse blockage in the bundle branches and sub-branches (fascicles).

The heart's natural rhythm, known as Normal Sinus Rhythm (NSR), is free from any disease or disorder. It is identified by a heart rate of 60 to 100 beats per minute. The regularity of the R-R interval may vary slightly with the breathing cycle, shortening slightly during inspiration. The heart's natural pacemaker is the sinoatrial node, responsible for generating this rhythm. Therefore, a characteristic feature of NSR includes a normal P-wave followed by a normal QRS complex. When the heart rate increases beyond 100 beats per minute, the rhythm is known as sinus tachycardia. This is not an arrhythmia but a normal response of the heart to higher demand for blood circulation.

1.5.1 Sinus Node Arrhythmias

Sinus node arrhythmias originate from the SA node of the heart, which serves as the normal pacemaker. Variations in the morphology of the P-wave characterise these types of arrhythmias. They can be classified into the following types:

- *Sinus Arrhythmia*: This is not a disorder or a true arrhythmia but a normal, physiologic variation in the sinus rate with the phases of respiration. The slowest instantaneous heartbeat may be less than 60 beats per minute, while the highest may exceed 100 beats per minute.
- *Sinus Bradycardia*: The rhythm originates from the SA node but at a rate of fewer than 60 beats per minute. The ECG appears normal except for the slow heart rate (Figure 1.17a).
- *Sinus Arrest*: The SA node intermittently fails to fire. There is no P-wave, no accompanying QRS complex and no T-wave. Bradycardia may result if the occurrence of sinus arrests is frequent. Sinus arrest results from a marked depression of the automaticity of the SA node. Since the automaticity of the S-A node is abnormal, the most extended P-P interval (i.e. the "pause" on the ECG) will not be a multiple of the shortest P-P interval, unlike SA exit block (Figure 1.17b).
- *Sino-Atrial Exit Block*: similar to sinus arrest, except that the SA node retains its automaticity, but the generated electrical impulse cannot exit from it and propagate. This is caused by an intermittent conduction block in the tissue surrounding the SA node. Occasionally, conduction manages to occur through the perinodal tissue. Since the automaticity of the SA node is expected, the most extended P-P interval is a multiple of the shortest P-P interval (the underlying rhythm).

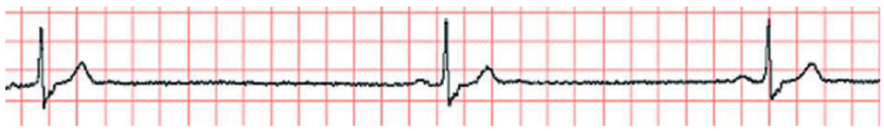

(a) In bradycardia, the heart beats at a slow rate, resulting in long R-R intervals.

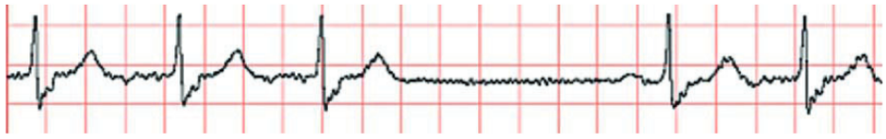

(b) Sinus arrest is characterised by a missing beat (P-QRS-T) that occurs repeatedly.

Figure 1.17: Examples of Sinus Arrhythmias [38].

1.5.2 Atrial Arrhythmias

Atrial arrhythmias occur when electrical impulses originate outside the SA node but within the atria. As the origin is not from the SA node, the morphology of the P-wave differs from that of the sinus P-wave. However, the subsequent QRS-T complex appears normal, as the ventricles receive their impulses through the AV node in the usual manner. Figure 1.18 shows the principal atrial arrhythmias: Premature Atrial Contraction (PAC), Atrial Tachycardia (AT), Atrial Flutter (AF) and Atrial Fibrillation (AF).

1.5.3 Junctional Arrhythmias

Junctional arrhythmias occur when the impulse originates within the AV junction, which includes the AV node and the Bundle of His. The resulting QRS complex and T-wave typically appear normal as they follow the common pathway for ventricular depolarisation. However, retrograde conduction to the atria may lead to the development of a P-wave with abnormal morphology and timing. The polarity of the P-wave is opposite to that of a normal sinus P-wave due to the retrograde propagation of depolarisation from the AV node towards the atria. Additionally, the wave appears after the onset of the QRS complex.

The primary junctional arrhythmias, shown in Figure 1.19, are Premature Junctional Contractions, Non-Paroxysmal Junctional Tachycardia and Paroxysmal Supraventricular Tachycardia.

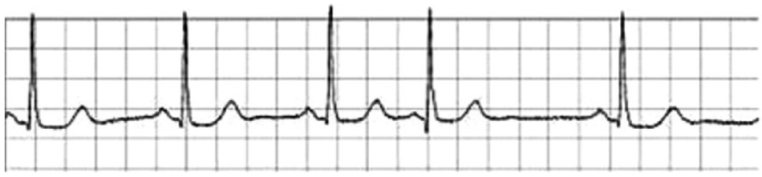

(a) A premature atrial contraction (PAC) is an atrial contraction that appears early in time with an abnormal P-wave morphology (shape).

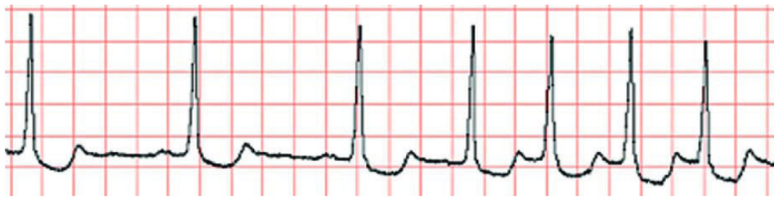

(b) Ectopic atrial tachycardia occurs when more than 3 PACs occur consecutively.

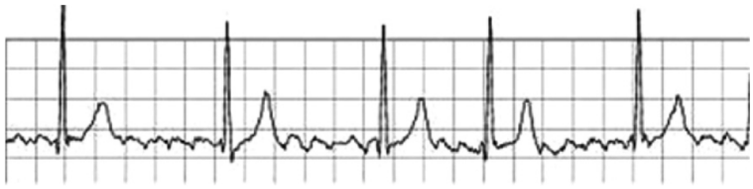

(c) Atrial Flutter. Atrial rate is very fast and has a consistent repetitive waveform with a saw-tooth like appearance.

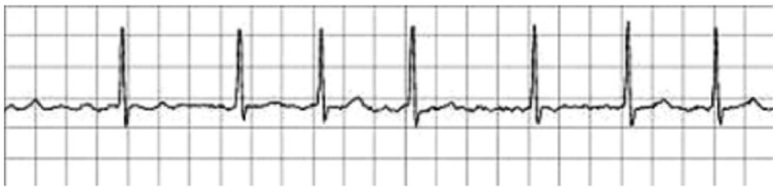

(d) Atrial Fibrillation. When atrial fibrillation occurs, the QRS appears erratically. There is no distinct P-wave.

Figure 1.18: Examples of Atrial Arrhythmias [38].

1.5.4 Ventricular Arrhythmias

Ventricular arrhythmias occur when the heart's impulses originate from the ventricles and then spread throughout the rest of the heart. These arrhythmias can happen due to either the ventricular myocardium's enhanced automaticity or a re-entry circuit. A normal conduction pathway from the atria to the ventricles results in a narrow, standard QRS complex where all ventricular myocardium

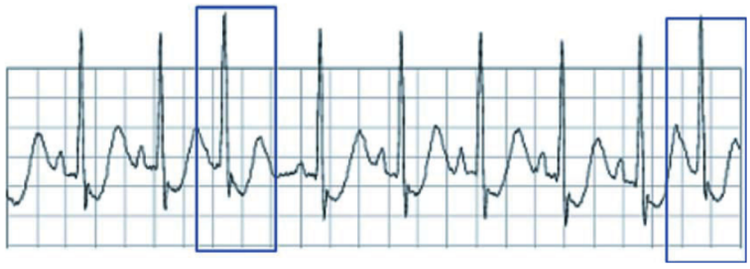

(a) In premature junctional escape contraction, a normal-looking QRS complex prematurely appears, but without a preceding P-wave. The accompanying T-wave is normal.

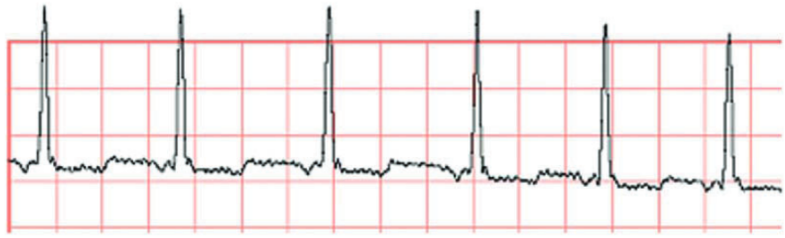

(b) Non-paroxysmal junctional tachycardia with retrograde conduction results in inverted P-waves. The atrial and ventricular rate falls in the normal range.

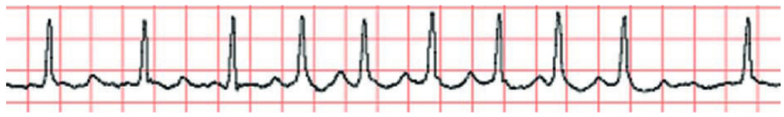

(c) Paroxysmal supraventricular tachycardia results in very fast heart rate ranging from 160 to 240 beats per minute for a short period of time.

Figure 1.19: Examples of Junctional Arrhythmias [38].

depolarises simultaneously. However, in cases of ventricular arrhythmias, the QRS complex is vast and bizarre in shape because the impulse is not propagated through the normal pathway but rather through non-specialized myocardium that conducts more slowly, resulting in a wider QRS complex and a different direction, leading to a bizarre-looking QRS complex.

In Figure 1.20, the main ventricular arrhythmias are shown: Premature Ventricular Contraction (PVC), Ventricular Tachycardia (VT), and Ventricular Fibrillation (VF).

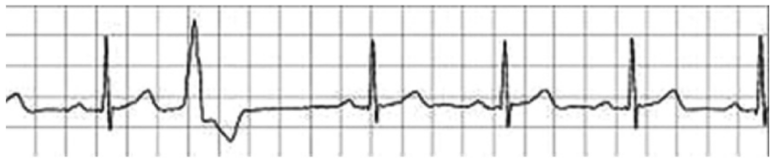

(a) An isolated premature ventricular contraction occurs without a preceding P-wave. The QRS morphology is bizarre in shape since depolarisation of the ventricles do not follow the normal sequence.

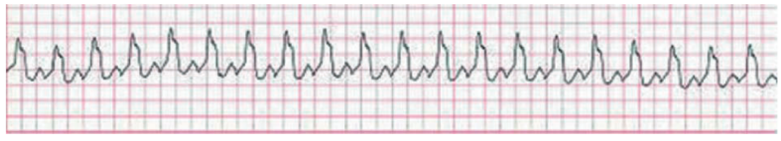

(b) Monomorphic ventricular tachycardia. Heart beats at a very fast rate and with a consistent bizarre-shaped QRS morphology.

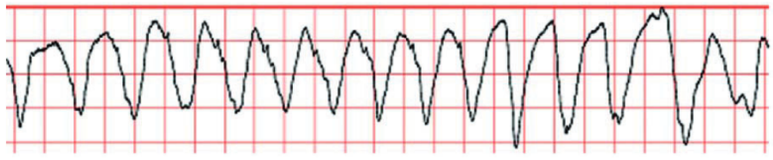

(c) Ventricular flutter exhibits a very rapid ventricular rate with a saw-tooth like ECG waveform.

Figure 1.20: Examples of Ventricular Arrhythmias [38].

1.5.5 Atrioventricular Blocks

The phenomena when electrical impulses are disrupted along the conduction pathways to the ventricles is known as atrioventricular blocks. This block may cause a delay or prevent the impulse from propagating to the rest of the conduction system intermittently. A first-degree AV block occurs when all the P-waves reach the ventricles, but the PR interval is prolonged. Second-degree AV blocks happen when some P-waves don't conduct to the ventricles and can be further categorised into:

- Wenkebach (or Mobitz Type 1).
- Mobitz Type II.
- 2:1 AV block.
- High-grade AV block (>3:1).

A complete heart block or third-degree block happens when all P-waves fail to conduct down to the ventricles. Pacemakers are used to treat this condition and bring the heart rate back to normal.

1.5.6 Bundle Branch and Fascicular Blocks

Bundle branch blocks are secondary to a conduction defect at the level of the right branch or the left branch of the bundle of His. In case of bundle branch block, the depolarisation of the two ventricles is asynchronous due to a delay in the activation process of the ventricle dependent on the blocked branch. This asynchronism causes a "loosening" of the QRS complexes is more than 120 ms. Depending on the locked branch, it is possible to recognise the right and left bundle branch blocks.

Chapter 2

State of the Art

This chapter will present some key concepts related to Artificial Intelligence and its application in medicine, with a particular focus on Machine Learning and Deep Learning techniques. We will then explain the main approaches commonly used in the literature for the specific task of cardiac anomaly classification, highlighting the differences between more traditional methods based on the extraction of "expert features" and more recent methods based on deep learning, such as the use of convolutional neural networks, the architecture details of which will be explained in this chapter. We will then analyse the main works found in the literature, highlighting those that classify cardiac anomalies on a beat-by-beat basis and those that classify them based on rhythm. Additionally, we will mention the main ECG databases and the performance metrics recommended by the Association for Advancement of Medical Instrumentation.

2.1 Artificial Intelligence in the Clinical Decision Support Field

In this paragraph, we will briefly overview important concepts related to Artificial Intelligence (AI) techniques like Machine Learning (ML) and Deep Learning (DL), as they are the basis of the methods used in research for identifying cardiac anomalies.

Seventy years ago, the idea of Artificial Intelligence was first introduced by Alan Turing through his description of "*thinking machines*". Later, John McCarthy came up with the term "*Artificial Intelligence*" to define the concept of computers being able to perform tasks that are typically considered intelligent when done by humans [39]. In healthcare, the cornerstone of effective patient care is experience and expertise. The more data and knowledge we have, the better equipped we are to make informed decisions.

One major obstacle for humans in acquiring extensive data is time limitations. Furthermore, with silicon chips, large amounts of patient data can now be accessed, obtained, and stored for processing. Utilising these vast amounts of data and transforming them to gain experience is the foundation of AI in medicine [40]. Besides, AI can aid physicians in risk-stratifying patients for interventions, identifying those most at risk, and evaluating multiple strategies to optimise overall patient outcomes. The next paradigm shift in medical education will involve integrating and educating physicians in model development.

The domain of Clinical Decision Support presents vast opportunities for AI to influence clinical management profoundly. While CDSS are not novel, the innovative concept of incorporating AI into a "black box" CDSS, which utilises inputs from diverse sources to generate decisions or recommendations for specific diagnostic and therapeutic strategies, represents a significant advancement [41]. AI-based CDSS have the potential to enhance the diagnosis, treatment, and prognosis of a specific medical condition by leveraging biomedical data to predict the likelihood of a medical outcome or the risk of a particular disease. These systems have the capability to analyse historical, present, and incoming patient data, enabling them to identify potential safety concerns, errors, or opportunities for improvement in the care pathway. Providing accurate and relevant predictions opens up new avenues for optimising patient care [42].

These systems can be developed using either traditional ML algorithms or the more advanced DL algorithms [21]. Figure 2.1 shows a taxonomy of Artificial Intelligence comprising Machine Learning and Deep Learning.

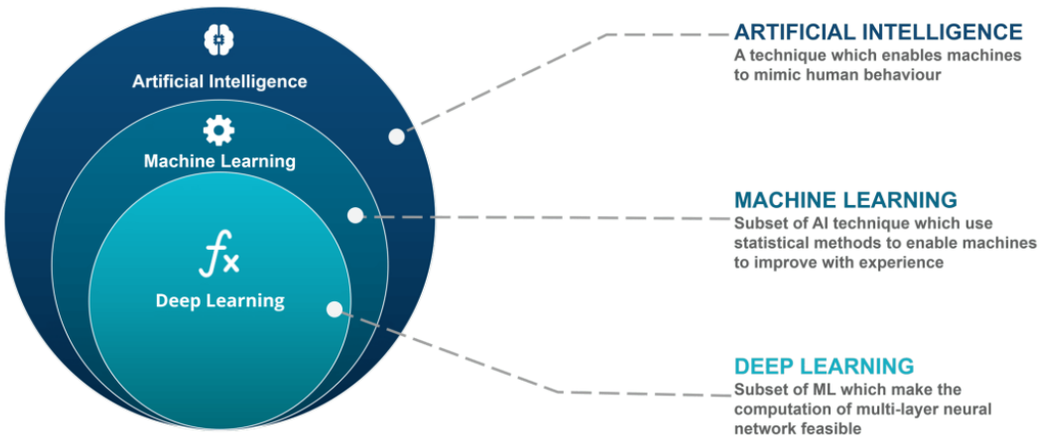

Figure 2.1: Artificial Intelligence Taxonomy [21].

2.1.1 Machine Learning

Machine Learning is a subfield of AI that focuses on enabling machines to mimic intelligent human behaviour. It encompasses the capability of a machine to learn from data and make predictions or take actions based on that learning. A ML system can have different descriptive, predictive, or prescriptive functions. In a descriptive function, the system uses data to explain past events, while in a predictive function, the system uses data to forecast future events. Lastly, in a prescriptive function, the system leverages data to offer suggestions or recommendations on actions to be taken [43, 44].

Several types of machine learning, including supervised and unsupervised learning, have distinct approaches and applications. In situations where training datasets are not available, unsupervised learning methods are employed. They are particularly valuable in scenarios involving unknown disease detection, new drug discovery, and fault diagnosis identification. On the other hand, supervised learning-based anomaly detection and classification techniques are efficient when annotated datasets and expert knowledge are present, enabling accurate detection and classification of anomalies [45].

2.1.2 Deep Learning

Deep Learning is a subset of ML that leverages computational models and algorithms inspired by the structure and functioning of biological neural networks in the brain. The human brain comprises a network of interconnected neurons, and deep learning aims to emulate this neural connectivity through Artificial Neural Network (ANN) techniques [46].

The term "*deep*" in deep learning is a technical term that refers to the number of layers in an ANN where there are typically three types of layers: the *input layer*, the *output layer*, and one or more *hidden layers*.

The input layer receives the input data, which can be in various formats, such as images, text, or numerical values. On the other hand, the output layer produces the final result of the data processing, which can be a classification, prediction, or any other desired output. The hidden layers are the intermediate layers between the input and output layers. They are responsible for extracting and learning the underlying patterns and representations within the data. The number of hidden layers can vary depending on the problem's complexity and the network's depth.

A deep ANN differs from a shallow ANN (characterised by a single hidden layer) by having a more significant number of hidden layers. This deeper architecture allows deep ANNs to perform more complex tasks. As data passes through each hidden layer, simpler features are combined and reassembled into more complex features.

In practice, deep learning excels at handling unstructured data and has demonstrated higher accuracy than traditional machine learning methods. However, it typically requires substantial training data to learn complex patterns and relationships effectively. Additionally, deep learning models often demand significant computational resources and specialised hardware and software for training and inference processes [47].

2.2 Approaches for the Classification of Cardiac Abnormalities

Over the years, numerous research studies have focused on classifying heartbeats. Existing solutions in this domain can generally be categorised into two main approaches: *feature engineering-based* methods and *deep learning-based* methods [48].

Regarding the first approach, in the past, the analysis of ECG signals relied heavily on diagnostic rules. This approach involved a two-step process: first, '*expert or hand-crafted features*' were extracted from the raw ECG data, and then these features were used to create decision rules or were input into ML algorithms to generate the final analysis results [49]. Expert features in ECG analysis can be classified into four main categories: *frequency-domain* features, *time-domain* features, *joint time-frequency* domain features, and *decomposition-domain* features [48]. These features can be extracted using computer-based algorithms, but they may not always be sufficient due to limitations in data quality and human expert knowledge [50]. Moreover, engineering hand-crafted features can be challenging,

even with a good domain understanding, often requiring iterative trial-and-error [51].

In recent years, studies exploring incorporating DL techniques in ECG analysis have significantly increased. These approaches aim to integrate feature extraction and classification stages within a unified framework, eliminating the need for handcrafted features. This methodology, known as *end-to-end learning*, has gained considerable attention [52]. A visual representation comparing the conventional methods and deep learning approaches can be found in Figure 2.2.

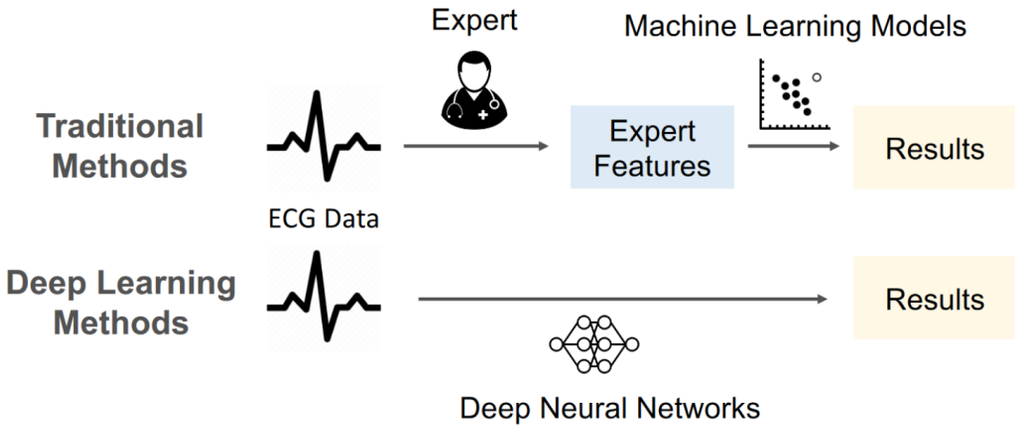

Figure 2.2: Comparison between traditional methods, that require the extraction of expert features, and deep learning methods [49].

2.2.1 Feature-engineering Based Methods

Feature-engineering based methods in ECG classification primarily focus on signal *feature extraction*, *feature selection*, and *classifier selection* [53].

In raw ECG signals, a heartbeat is represented as a high-dimensional time-series sequence; it is challenging for classifiers to interpret and extract relevant information to differentiate between different types of heartbeats. Hence, it becomes necessary to summarise and extract patterns from the time-series sequence of heartbeats to represent them effectively. These patterns, known as '*features*', play a crucial role in the classification process, directly influencing the final classification performance.

Feature extraction is typically guided by medical knowledge, which aids in enhancing the classification performance and providing explanatory insights into the model. An example of such a feature is the RR-interval, which is widely used due to its comprising of essential rhythm information.

Due to the abundance of features that can be derived from the ECG signal, the *feature selection* process becomes crucial. Many studies rely on the researchers'

experience and understanding of the task to determine which features to include, but this approach does not guarantee the optimal selection of features. On the other hand, a few studies have explored the feasibility of automated feature selection techniques to identify the most representative features. Generally, a feature selection technique comprises a search strategy to identify and evaluate candidate feature subsets through an objective function.

As for the *classifier selection*, the Support Vector Machine is widely used due to its robustness, good generalisation, and computational efficiency, as evidenced by studies such as [54, 55, 56]. Additionally, Decision Trees [57, 39], K-Nearest Neighbors [58, 59], and ANNs [60, 61] are also commonly employed in the literature for this purpose. Other classifiers that have been utilised include Optimum-Path Forest, Linear Discriminant, and hidden Markov models [53, 62].

2.2.2 Deep-Learning Based Methods

Heartbeat classification has recently witnessed significant advancements, primarily attributed to Deep Neural Networks (DNNs). A DNN is a computational model comprising multiple layers of processing units, enabling it to automatically learn and extract high-level representations from raw ECG recordings without extensive data preprocessing. This ability to learn intricate patterns and features directly from the data has revolutionised the field and improved classification accuracy and performance. Convolutional Neural Network (CNN), Recurrent Neural Network (RNN), Autoencoder (AE), and Long Short-Term Memory network (LSTM) are some of the DNNs used in the task of ECG classification. The following paragraph will outline the fundamental principles underlying a CNN, as it is the method chosen in this thesis.

Convolutional Neural Networks

LeCun first introduced CNNs in [63] as a type of neural network designed explicitly for feature extraction tasks while preserving the spatial configuration of the data and ensuring translation invariance. These characteristics have made CNNs extremely popular in domains where object shape is crucial, such as image analysis [64]. Recently, CNNs have attracted more and more attention in the applications in ECG signal classification because they have been proven effective in recognising key patterns and learning valuable features, such as P-waves and QRS-complexes of ECG heartbeats [53].

A typical CNN architecture, shown in Figure 2.3 consists of multiple convolutional layers, pooling layers, and fully connected layers, briefly described below. For further information please refer to the article by Alzubaidi et. al: "*Review of Deep Learning: Concepts, CNN Architectures, Challenges, Applications, Future*

Directions" [65].

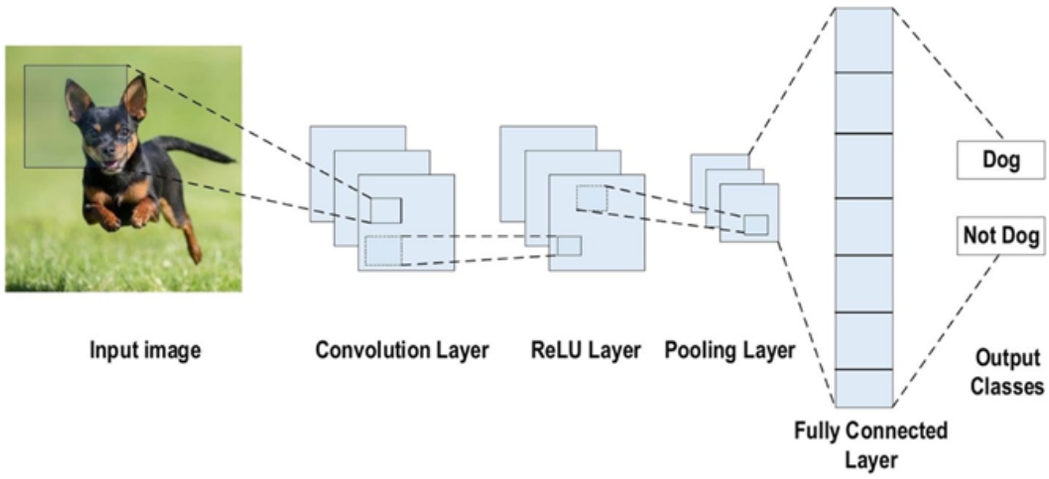

Figure 2.3: Example of CNN architecture for image classification [65].

Convolutional Layer

In a CNN, the convolutional layer is the central element responsible for most computational tasks. We define:

- An input tensor I, which represents a multidimensional array of data.
- A kernel K, which represents a multidimensional array of parameters.

The convolution operation S (shown in Figure 2.4) computes a weighted average of the input tensor and the kernel at every position, according to this equation:

$$S(p) = \int I(p-a)K(a)da \tag{2.1}$$

Where p is the position index.

The result of the convolution operation is referred to as a *feature map*. It is generated by matrix multiplication between the kernel and each equally-sized sub-matrix of the input tensor. This means that each kernel produces its own feature map. The number of kernels in a CNN is determined based on the specific task. It is typically defined by the complexity and diversity of the features that need to be learned from the input data.

After the convolution operation, applying a Rectified Linear Unit (ReLU) activation function is common[1]. The ReLU function introduces non-linearity into the network by converting negative values to zero and leaving positive values unchanged. It has been widely adopted in CNN architectures due to its low computational load and effectiveness in improving the network's learning capabilities.

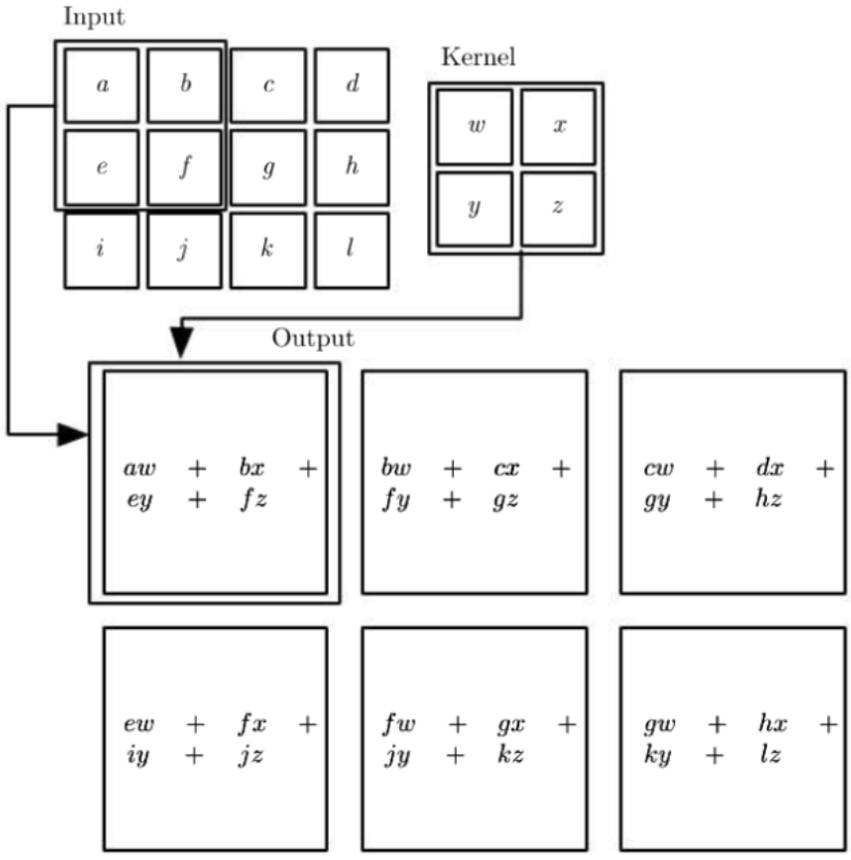

Figure 2.4: An example of 2D convolution between an input tensor of size 4x3 and a kernel of size 2x2 [66].

Pooling Layer

The pooling layer replaces the previous layer's output with a condensed representation, effectively reducing the size of the learned features and mitigating

[1]In ANNs, an activation function is a mathematical function applied to the output of a neuron or a group of neurons. It determines whether the neuron should be activated or not, based on the weighted sum of its input values. The activation function adds non-linearity to the neural network and is essential in the process of training the network [65]

the problem of *overfitting*[2] . Commonly employed pooling methods, such as max pooling, average pooling, and global average pooling, are depicted in Figure 2.5.

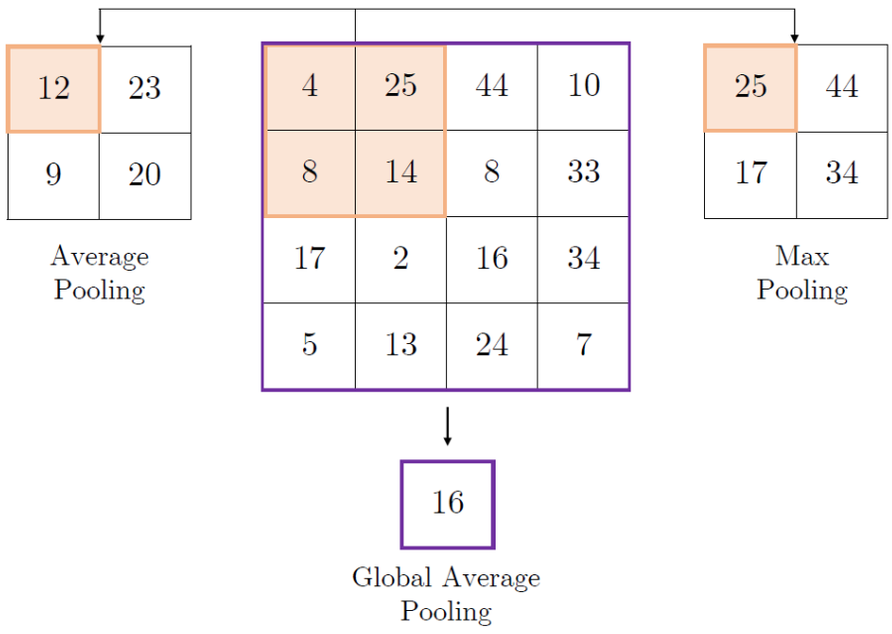

Figure 2.5: Three types of pooling operations. Modified from [66].

Fully Connected Layer

Typically, the Fully Connected (FC) layer is positioned at the end of a CNN architecture. In this layer, each neuron is interconnected with all neurons from the preceding layer. The FC layer adopts the fundamental approach of a conventional Multi-Layer Perceptron (MLP) neural network, as it is a type of *feed-forward* ANN.

In classification tasks, such as the classification of cardiac anomalies, specific *loss functions* are employed in the output layer. These loss functions quantify the predicted error generated by the CNN model across the training samples. Subsequently, the CNN learning process aims to optimise this error through various techniques and algorithms.

The loss function uses two parameters to calculate the error: the CNN estimated output (referred to as the *prediction*) and the actual output (referred to as the

[2]Overfitting is a common issue that can occur when training machine learning models. It refers to the phenomenon where the model becomes too complex and starts to fit the training data too closely, leading to poor performance on new, unseen data. This can be caused by various factors, such as using an overly complex model, having insufficient training data, or training for too long [65, 67].

label). Different types of loss functions are utilised for various problem types, and one widely employed option is the *Cross-Entropy* or (*Softmax*) loss function, which is frequently used for evaluating the performance of CNN models. It is also known as the *Log* loss function, and its output represents a probability of belonging to the class, denoted as p, which is in the range of [0,1]. The mathematical representation of the output class probability can be expressed as follows:

$$p_i = \frac{e^{a_i}}{\sum_{k=1}^{N} e_k^a} \tag{2.2}$$

Here, e^{a_i} represents the non-normalized output from the preceding layer, while N represents the number of neurons in the output layer (equal to the number of classes of the problem). Finally, the cross-entropy loss function can be mathematically represented as (y_i is the desired output and p_i is the predicted one):

$$H(p, y) = -\sum_i y_i \log(p_i) \qquad \text{where} \qquad i \in [1, N] \tag{2.3}$$

Overfitting is the central issue for CNN models to obtain well-behaved generalisations. If a model performs well on training data but fails on test data (i.e., data it has not seen before), it is considered *over-fitted*. On the contrary, an *under-fitted* model occurs when the model does not learn enough from the training data. Lastly, the model is *just-fitted* if it executes well on both training and testing data – this is the optimal scenario. These three types are illustrated in Figure 2.6.

Various concepts are used to help the regularisation to avoid overfitting, such as dropout, drop-weights, data augmentation and batch normalisation.

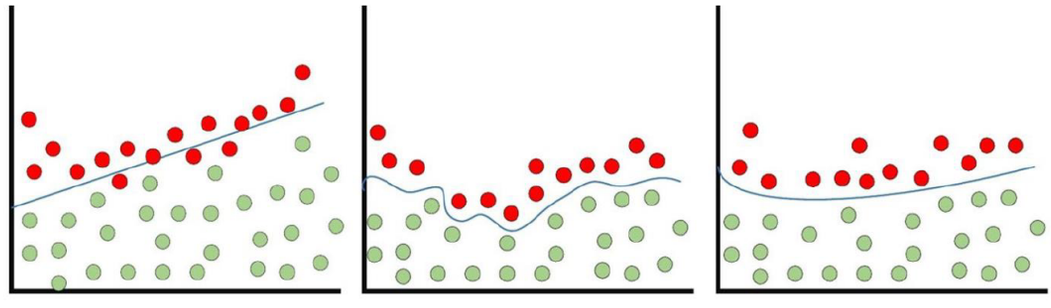

Figure 2.6: Over-fitting and under-fitting issues [65].

2.3 Critical Analysis of the Existing Works

The majority of research studies in the field of cardiac abnormalities classification focus on the classification of individual heartbeats. This is primarily driven by the standard proposed by the Association for Advancement of Medical Instrumentation (AAMI), namely ANSI/AAMI EC57:1998/(R) 2008. According to this standard, heartbeats are classified into 15 types, which are further categorised into five superclasses: Normal (N), Supraventricular (S) ectopic, Ventricular (V) ectopic, Fusion (F), and Unknown (Q) [68]. Table 2.1 provides an overview of the AAMI categorisation of abnormal heartbeats, while Figure 2.7 illustrates examples of these five different types [69].

In contrast, there are no specific regulations regarding the classification of rhythms; however, the work of Zhang et al. [70] suggested grouping 11 abnormal rhythms into four super classes based on the guidelines provided by cardiologists, as shown in Table 2.2.

Table 2.1: Classification of heartbeats according to AAMI standard: ANSI/AAMI EC57:1998/(R) 2008 [53].

AAMI class	Original class	Type of beat
Normal (N)	N	Normal beat
	L	Left bundle branch block beat
	R	Right bundle branch block beat
	e	Atrial escape beat
	j	Nodal (junctional) escape beat
Supraventricular ectopic beat (S)	A	Atrial premature beat
	a	Aberrated atrial premature beat
	J	Nodal (junctional) premature beat
	S	Supraventricular premature beat
Ventricular ectopic beat (V)	V	premature ventricular contraction
	E	Ventricular escape beat
Fusion beat (F)	F	Fusion of ventricular and normal beat
Unknown beat (Q)	/	Paced beat
	f	Fusion of paced and normal beat
	Q	Unclassifiable beat

In the context of heartbeat classification, following the AAMI standard, a notable work was done by Acharya et al. [71]. They proposed a 9-layer CNN model for the general heartbeat classification task. The model takes segmented heartbeats

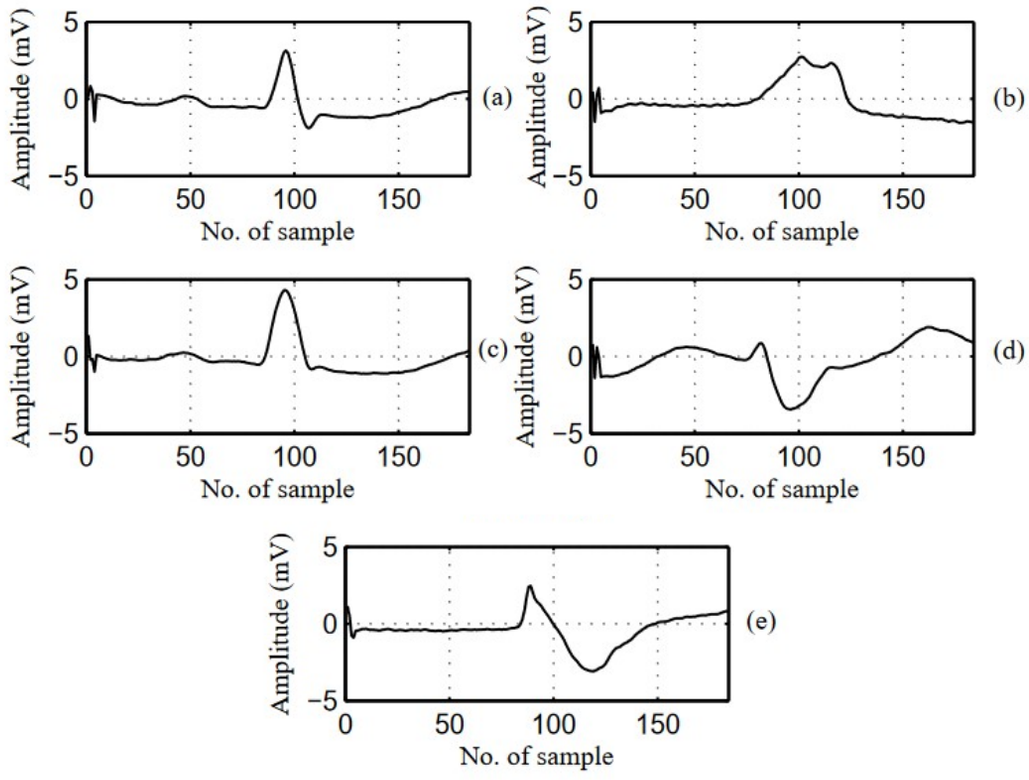

Figure 2.7: Super classes of heartbeats according to AAMI standard: (a) Normal (N) (b) Supraventricular ectopic (S) (c) Ventricular ectopic (V) (d) Fusion (F) (e) Unknown (Q), respectively [53].

as input and calculates the probability of each heartbeat type to which the input heartbeat may belong.

In addition to CNN, LSTM has also shown good performance on ECG signals, as Tan et al. [72] demonstrated in their work on detecting coronary artery disease. This has led to attempts at combining both CNN and LSTM, resulting in state-of-the-art results that Oh et al. achieved [73]. A similar approach was proposed by Liu et al., who utilised empirical mode decomposition to decompose segmented heartbeats into N components. 2D CNN layers processed the first N/2 components, while stacked bidirectional LSTM layers processed the remaining components. The outputs of both the CNN and LSTM layers were combined in the fusion layer to make a classification decision.

Regarding works that classify abnormal rhythms, one of particular importance is the study by Yildirim et al. [74]. This work is based on a low computational complexity CNN, making it suitable for telemedicine applications, especially on

Table 2.2: Classification of rhythms according to the work presented by Zhang et. Al [70].

Rhythm Class	Original Rhythm	Type of Rhythm
SR	SR	Sinus Rhythm
	SI	Sinus Irregularity
SB	SB	Sinus Bradycardia
AFIB	AFIB	Atrial Fibrillation
	AF	Atrial Flutter
GSVT	SVT	Supraventricular Tachycardia
	AT	Atrial Tachycardia
	SAAWR	Sinus Atrium to Atrial Wandering Rhythm
	ST	Sinus Tachycardia
	AVNRT	Atrioventricular Node Reentrant Tachycardia
	AVRT	Atrioventricular Reentrant Tachycardia

mobile devices and cloud computing for monitoring ECG signals from a single lead. Similarly, Acharya et al. [75] proposed a similar neural network focusing explicitly on classifying Atrial Fibrillation, Atrial Flutter, and Ventricular Fibrillation.

The mentioned works focus on classifying cardiac arrhythmias using a single channel of ECG signal. However, some studies, such as those by Yang et al. [76] and Tung et al. [77], have instead focused on multi-channel approaches to improve detection accuracy and reduce false positive alarms.

2.4 Evaluation of a Heartbeat Classification Model

Several ECG databases that serve as benchmarks for evaluating heartbeat classification models, aiming to standardise the evaluation of automatic arrhythmia

classification methods have been defined by AAMI. Among these databases, the most notable one for arrhythmia is the 'Massachusetts Institute of Technology - Beth Israel Hospital Arrhythmia Database' (MIT-BIH DB) [36]. This database holds significant importance as it was the first publicly available database designed for this purpose. Researchers often utilise this database to assess and validate the performance of various arrhythmia classification algorithms.

The AAMI has also recognised the need for multiple performance metrics to thoroughly evaluate heartbeat classification models, unlike other classification problems where overall accuracy alone is sufficient. In the context of evaluating arrhythmia classification models, researchers commonly utilise the MIT-BIH Database, which is a widely used benchmark dataset. This database provides valuable real-world ECG recordings for developing and testing arrhythmia classification algorithms. More information about the databases mentioned and the performance recommended by the AAMI are given in the following paragraphs.

2.4.1 Databases Used in the Construction of an ECG Classification Model

MIT-BIH Database

The MIT-BIH Database is widely employed in numerous literary publications, primarily due to its distinctiveness in incorporating the five arrhythmia groups recommended by the AAMI, as detailed in Table 2.1 [62]. These arrhythmia groups serve as a comprehensive representation of cardiac anomalies. Consequently, the database's utilisation allows researchers to assess and develop automatic arrhythmia classification methods aligned with the AAMI's standardised categories. This uniqueness and adherence to the AAMI's proposed arrhythmia groups contribute to the database's significance and widespread adoption within the research community.

The ECGs included in the MIT-BIH Arrhythmia Database originate from a collection of over 4000 long-term Holter recordings acquired by the Beth Israel Hospital Arrhythmia Laboratory from 1975 to 1979. These recordings were obtained from both inpatients and outpatients, with approximately 60% originating from inpatient cases. The database, as outlined in the MIT-BIH Arrhythmia Database Directory [36], comprises two distinct sets of records:

1. 23 records (numbered from 100 to 124 inclusive with some numbers missing) were derived randomly from the larger pool of long-term recordings.

2. 25 records (numbered from 200 to 234 inclusive, again with some numbers missing) specifically curated to encompass various rare but clinically significant phenomena that may not be adequately represented in a small random sample of Holter recordings.

The combination of these two sets of records provides a diverse range of ECG data, capturing both common and infrequent cardiac events, contributing to the comprehensive nature of the MIT-BIH Arrhythmia Database.

Each of the 48 records in the MIT-BIH Arrhythmia Database has a duration slightly exceeding 30 minutes and consists of two ECG leads. The primary lead, called '*lead A*', is typically a modified version of lead II (better described in paragraph 1.4.1). The secondary lead, designated as '*lead B*', is typically lead V1, although it may correspond to lead V2, V5, or V4 in certain records. It is worth noting that in the literature, lead A is commonly utilised for heartbeat detection due to its greater prominence in capturing the QRS complex [62].

The analogue outputs of the playback unit were converted into digital signals at a sampling rate of 360 Hz per signal in real-time. The digitisation process was carried out using custom-built hardware developed at the MIT Biomedical Engineering Center and the BIH Biomedical Engineering Laboratory [36].

Every heartbeat in the MIT-BIH Database is annotated independently by two or more cardiologists. This process ensures that any differences in opinion are resolved, resulting in a final set of reference annotations for each heartbeat in the database. In total, there are approximately 110,000 annotations available. Additionally, rhythm annotations are also provided.

Figure 2.8 displays a segment of the signal obtained from subject #205 along with the corresponding annotations.

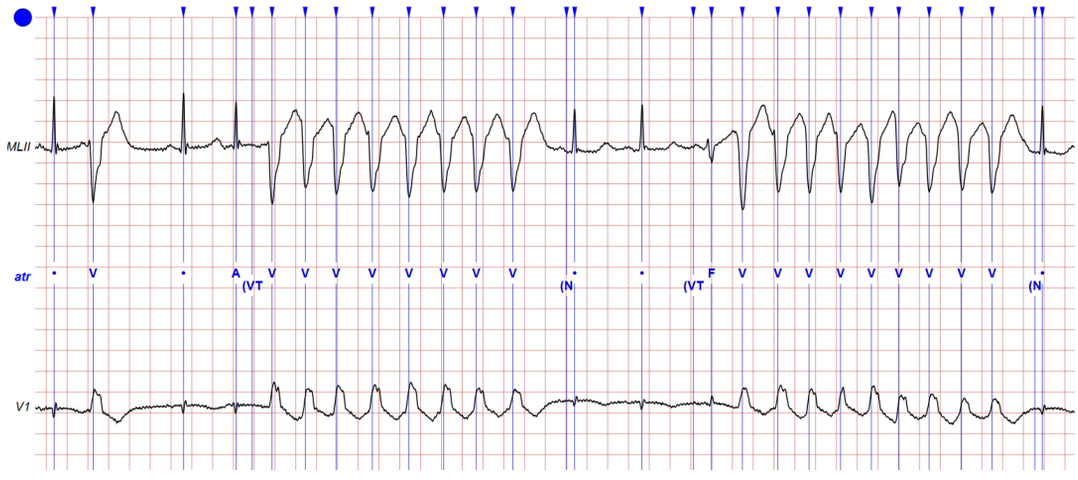

Figure 2.8: Example of beat annotation from the 10 seconds of the signal #205 [36]. In this case Ventricular Fusion (F), Ventricular Premature (V), Atrial Premature (A) beats have been annotates as well as some rhythms annotations (N: Normal, VT: Ventricular Tachycardia).

INCART DB

The St. Petersburg 12-lead arrhythmia database (known also as INCART DB) is widely used and freely accessible. It consists of 75 ECG recordings sampled at a rate of 257Hz. These recordings were extracted from 32 records at the St. Petersburg Institute of Cardiological Technics (Incart) in 2008 [78].

Each recording in the INCART DB contains 12 standard leads and lasts 30 minutes. The annotations for the ECG signals were initially generated by an automatic algorithm and then manually corrected based on the standard PhysioBank beat annotation definitions [79]. In addition to beat annotations, rhythm abnormalities, similar to the MIT-BIH DB, were also annotated. A summary of the distribution of annotated beats can be found in Table 2.3.

In addition to MIT-BIH and INCART DB, other commonly used ECG databases are: The PTB Diagnostic database [80], Creighton Ventricular Tachyarrhythmia Database [81] and China Physiological Signal Challenge 2018 [82].

Table 2.3: Comparison of the distribution of annotated beats in INCART and MIT-BIH DBs. Modified from [53].

Database	N	S	V	F	Q
MIT-BIH	90125	2781	7009	803	15
INCART	153491	1958	19993	219	6

2.4.2 Performance Metrics Recommended by AAMI

The development of an AI-based CAD system is typically divided into two phases: *training* and *testing*. During the testing phase, various measures AAMI recommends are used to evaluate the performance of classification methods. These measures help assess the effectiveness of the CAD system in correctly identifying different types of heartbeats. The measures recommended by AAMI include [62]:

- *Sensitivity* (Se), also known as '*Recall*': It represents the proportion of true positive predictions (correctly identified abnormal heartbeats) out of all actual positive instances (total abnormal heartbeats). A higher sensitivity indicates a better ability to detect abnormal heartbeats.
- *Positive predictivity* (+P), also known as '*Precision*': It measures the proportion of true positive predictions (correctly identified abnormal heartbeats) out

of all positive predictions (total predicted abnormal heartbeats). A higher positive predictivity indicates a lower rate of false positives.

- *False positive rate* (FPR): It calculates the proportion of false positive predictions (incorrectly identified normal heartbeats) out of all actual negative instances (total normal heartbeats). A lower false positive rate indicates a lower rate of misclassifying normal heartbeats as abnormal.
- *Overall accuracy* (Acc): It measures the proportion of correct predictions (both true positives and true negatives) out of the total number of instances.

To compare different methods, the first three measures (sensitivity, positive predictivity, and false positive rate) are particularly relevant, considering that the results of the majority class can strongly distort the overall accuracy. In this way, the first three measures are the most relevant for comparing the methods since the classes for the heartbeat types are highly imbalanced in available databases.

While AAMI specifies benchmark databases and evaluation metrics, there is a lack of a specific protocol that provides clear guidelines on how to perform an evaluation using these databases. The AAMI does not specify which recordings or heartbeats should be used for training a model and which should be used for testing the method. However, in the literature, two main paradigms are employed for constructing a cardiac anomaly classification model [62, 83]:

1. *Inter-patient paradigm*: In this type of classification of ECG beats, each patient's data are divided into training and test sets. This means that the data from each patient are used for both training the model and evaluating its performance. Most studies on beat classification adopt this paradigm, where the focus is on individual patients' data and classification within those specific patients.
2. *Intra-patient paradigm*: This paradigm uses data from different patients to train and evaluate the model. These methods aim to assess the model's generalisation across a larger population and overcome real-world challenges and these methods use data from multiple patients to create a model that can effectively classify anomalies in a diverse patient population.

The choice between these paradigms depends on the specific research objectives and data availability. The inter-patient paradigm is commonly used in studies focusing on beat classification, while the intra-patient paradigm addresses broader generalisation challenges.

Chapter 3

Design and Implementation of a CAD system for Automated ECG Anomaly Classification

In this chapter, we will discuss the methods and implementation choices for the development of the first task of this thesis. The underlying idea of this stage is to design and implement a CAD system for automated ECG classification that can be used in the future on a database consisting of properly labelled signals acquired through the Hi-ECG device. However, such a database is currently unavailable. Therefore, the designated model has been implemented using the freely available MIT-BIH database. In terms of architecture, Convolutional Neural Networks have been chosen as they have proven highly efficient in previous works in this field. We will discuss how these signals are preprocessed to enhance the signal-to-noise ratio and how to segment and normalise them. Next, we will illustrate how the network was designed and trained and how its performances were evaluated in the testing phase, according to the Association for the Advancement of Medical Instrumentation recommendations.
The CAD system presented is not applicable to signals acquired with the Hi-ECG device as they are morphologically different from the MIT signals. Therefore, a future development of the work involves applying the proposed methodology in the presence of a database of signals acquired with the Hi-ECG device, with properly labelled cardiac anomalies.

3.1 Motivations and Context

In the previous chapters, we highlighted the importance of signal morphology in classifying cardiac anomalies. Considering this, to apply a cardiac anomaly classification model to signals acquired with the Hi-ECG device, it is necessary to consider that there is currently no database of ECG signals acquired with such a device that includes properly labelled recordings of cardiac patients. For this reason, in this thesis work, we chose to develop two parallel tasks, which will be described in more detail in the following two chapters:

- *Task #1: Design and Implementation of a CAD System for Automated ECG Anomaly Classification.* The purpose of this task is to develop a CAD system to be trained in a future phase of the work, considering a database of signals acquired with the Hi-ECG device. For more information on this database, please refer to chapter 6. Since we do not have access to this specific database, we have chosen in this phase to use one of the publicly available databases discussed in the paragraph 2.4.1.
- *Task #2: Development of a method for the adaptation of a Pre-trained CAD System to Hi signals.* This task aims to develop a methodology to enable the use of a CAD system, pre-trained with signals from freely available databases, on signals acquired with the Hi-ECG device.

This chapter describes the steps necessary for the first task. It is important to consider that the CAD system developed in this study cannot be directly applied to the classification of anomalies present in signals acquired with the Hi-ECG device due to the following reasons [84]:

- ECG tracings acquired by wearable devices, such as the Hi-ECG device, differ from those typically considered in the literature, such as the MIT-BIH Database. For example, in the Hi-ECG device, the electrodes are positioned closer together compared to a classical Holter or 12-leads configuration, which can result in changes in the morphology of the signals, as discussed in section 1.4.
- The Hi-ECG device is intended to be placed by users themselves rather than by clinicians. Therefore, it is necessary to consider that there may be positioning errors, which can again lead to modifications in the morphology of the ECG signals.
- The Hi-ECG device's user manual specifies three configurations in which the user can position the device. Different configurations correspond to different signal morphologies.

- During long-term monitoring, user movements can cause device displacement, compromising the quality of the signals. Moreover, the morphology of the heartbeats might vary due to changes in the heart rate. This makes ECG tracings acquired by the Hi-ECG device more heterogeneous than those acquired in more controlled situations, such as those in the MIT-BIH Database.

Considering the aforementioned reasons, in order to implement the CAD system directly on the signals acquired from the wearable device under analysis, it would be necessary to have a specifically constructed database using that device with properly labelled cardiac anomalies. However, this chapter proposes a procedure that can be followed in the future if such a database becomes available.

The MIT-BIH Arrhythmia DB was chosen for training and testing the proposed CAD system. The reason behind this choice is that this database is considered the most comprehensive for the specific task of classifying cardiac anomalies, and it is also the most widely used database in the literature [85]. This allows a more accurate comparison between the present work and state-of-the-art studies. Considering then the fact that the annotations concerning abnormal rhythms are far less than the annotations for beats, it has been chosen to develop a network for the classification of abnormal heartbeats, following the ANSI/AAMI EC57:1998/(R) 2008 standard, that recommends categorising beats in 5 superclasses:

- Normal (N).
- Supraventricular ectopic (S).
- Ventricular ectopic (V).
- Fusion (F).
- Unknown (Q).

3.2 Proposed Pipeline

For this task, it was decided to design a Convolutional Neural Network, as it is one of the most used networks in this field, given the excellent performance that has been achieved, such as in the works of Acharya et. Al [71, 86, 87], Yıldırım et. Al [88] and Zubair et. Al [83].

The pipeline consists of two phases: *Training* and *Testing*, represented graphically in Figure 3.1.

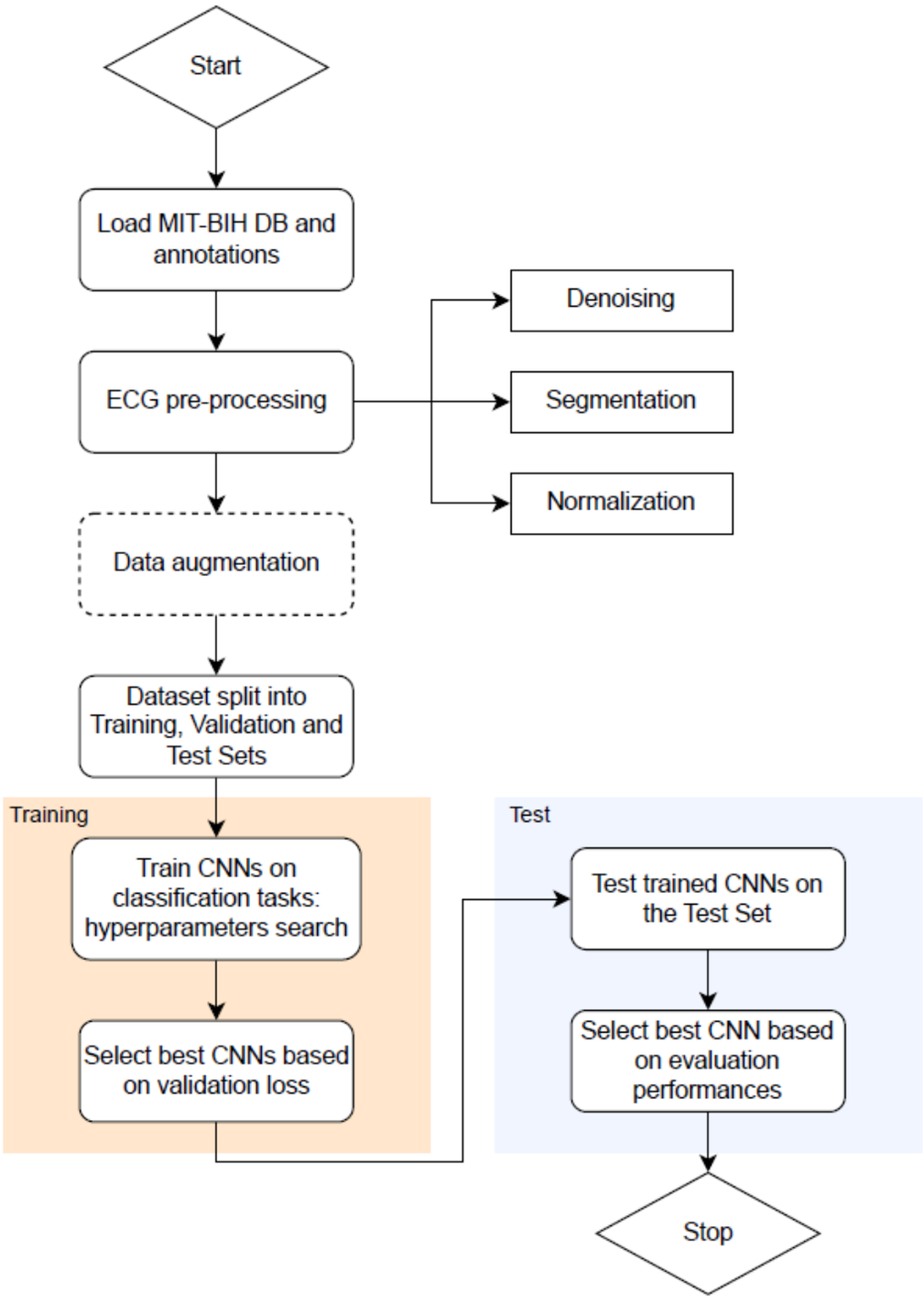

Figure 3.1: Proposed pipeline for the first task of the work. In two different colours are represented the training and the test phase.

Generally, the proposed steps consist of:

1. *Loading MIT-BIH DB signals and annotations*: In this study, only Modified Limb Lead II (MLL-II) ECG signals were analysed, as it is a bipolar lead similar to the leads acquired by the Hi-ECG device.

2. *ECG Pre-processing*: This phase involves noise removal, ECG segmentation, and normalisation of the signals.

3. *Data augmentation*: Generating synthetic data is one way to overcome the imbalance in the number of ECG heartbeats in the five classes (N, S, V, F, Q). Another method implemented in this thesis is using a cost-sensitive loss function during network training.

4. *Dataset split into Training, Test, and Validation Sets*: A ten-fold cross-validation approach was used to avoid overfitting and ensure robust evaluation.

5. *Training of the model*: This phase also includes a grid search tuning method to optimise the network's performance.

6. *Testing of the models*: All the trained networks resulting from the grid search tuning method were tested on the Test Set, and their evaluation performances were obtained. The model with the best performance was selected for this task.

3.3 ECG Data Preprocessing

The ECG signals are processed as follows:

- Removal of noise.
- ECG segmentation.
- ECG normalisation.

3.3.1 Noise Removal

To ensure accurate cardiac arrhythmia detection and classification, it is crucial to address the issue of background noise that accompanies the acquisition and transmission of ECG signals. Implementing appropriate measures to mitigate the impact of noise is necessary for reliable analysis and interpretation of the signals [53, 89].

ECG signals can be affected by various types of noises, including baseline wander, powerline interference, electrode motion artefacts, and EMG noise. These artefacts can introduce distortions and unwanted components into the ECG signal, making it challenging to analyse and interpret the underlying cardiac activity accurately. A brief explanation of these noises is given below [90, 91]:

- *Baseline wander*: It is characterised by the shifting or wandering of the baseline axis of a signal, causing the entire signal to deviate from its normal position. In ECG signals, baseline wander can occur due to improper electrode-skin impedance, patient movement, and respiration. The frequency content of baseline wander typically lies within the range of 0.5 Hz, but it can increase during intense body movement or stress tests.

- *Powerline interference*: It refers to the presence of electromagnetic fields generated by powerlines, which can introduce noise into ECG signals and other bioelectrical signals recorded from the body surface. This interference is characterised by sinusoidal patterns at 50 or 60 Hz. The narrowband nature of powerline interference makes it challenging to accurately analyse and interpret low-amplitude waveforms, leading to unreliable delineation and the possibility of spurious waveforms.

- *Electrode Motion Artifacts*: They occur when the impedance of the skin around the electrodes changes due to stretching or movement. These artefacts share similarities with baseline wander regarding signal characteristics but are more problematic to mitigate because their spectral content significantly overlaps with the QRS complex. They typically manifest as high-amplitude waveforms, occasionally mistaken for PQRST complexes.

- *Electromyographic (EMG) Noise*: It represents a significant challenge in many ECG applications, particularly during recordings obtained during exercise. This noise is caused by muscle activity and can obscure low-amplitude waveforms. Unlike baseline wander and powerline interference, EMG noise cannot be effectively removed through narrowband filtering due to its spectral content overlapping with the PQRST complex. Filtering out muscle noise presents a more complex problem, requiring advanced techniques to separate it from the desired ECG signal accurately.

There are many approaches for filtering such noises, such as Infinite Impulse Response (IIR) and Finite Impulse Response (FIR) Filtering, Adaptive Filtering, Discrete and Bionic Wavelet Transform (DWT, BWT) Approaches, Moving Average Approach, Filtered Residue Method, and Empirical Mode Decomposition [91, 89].

The objective of filtering is to extract the ECG signal from the noise, ensuring that the clinical information remains undistorted while removing as much noise as

possible. To achieve this, it is necessary to understand the frequency contributions of the various waves that make up the ECG signal. Specifically, variations in the speed of wavefront propagation during the cardiac cycle, as described in paragraph 1.3.1, are manifested by differences in the frequency content of ECG waves. As shown in Figure 3.2, The T wave is predominantly found within the frequency range of zero (DC) to 10 Hz, the P wave is characterised by frequencies ranging from 5 to 30 Hz, and the QRS complex typically contains frequencies within the range of 8 to 50 Hz [92].

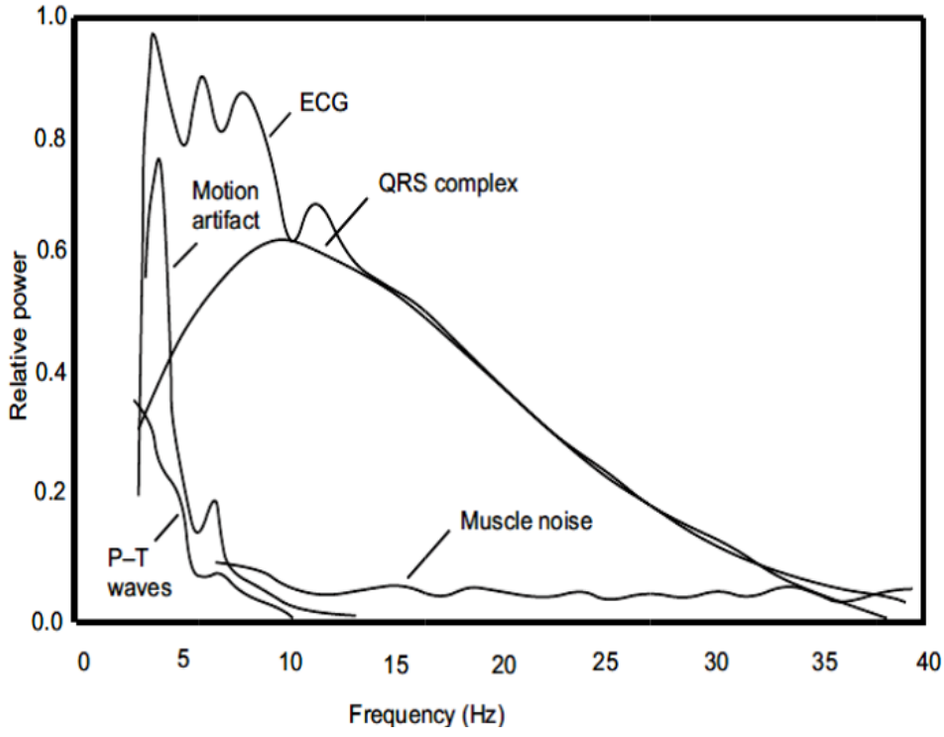

Figure 3.2: Power spectra of ECG components showing the relative frequencies [93]. The spectra include QRS complex, P and T waves, muscle noise, and motion artefacts. The analysis is based on an average of 150 beats.

For the noise removal of MIT-BIH signals, wavelet-based denoising was chosen as the approach, as it is a commonly used technique in the literature and is known for its effectiveness in preserving signal features while effectively reducing noise. Its main advantages over other techniques include the coefficient compaction characteristics of wavelets, the ability to dilute noise in the wavelet domain, and the removal of redundancy. In fact, it is advantageous in ECG signals due to their large data size. ECG data requires significant memory storage, averaging 100 MB daily for a signal sampled at 1 kHz. This poses challenges for real-time

telemedicine applications, where efficient transmission of ECG signals to remote diagnosis facilities is necessary [94].

3.3.2 Wavelet-based Denoising of MIT-BIH DB

A wavelet is a mathematical function that exhibits wave-like oscillations with an amplitude that starts from zero, increases, and then decreases back to zero. Figure 3.3 illustrates an example of a wavelet function, specifically the first derivative of Gaussian function. Wavelets have become a valuable tool in signal processing and data analysis because they capture localised information in both time and frequency domains and extract features from various types of data, including signals, images, and time series. They are beneficial in applications where the data is local and global features need to be analysed simultaneously [95].

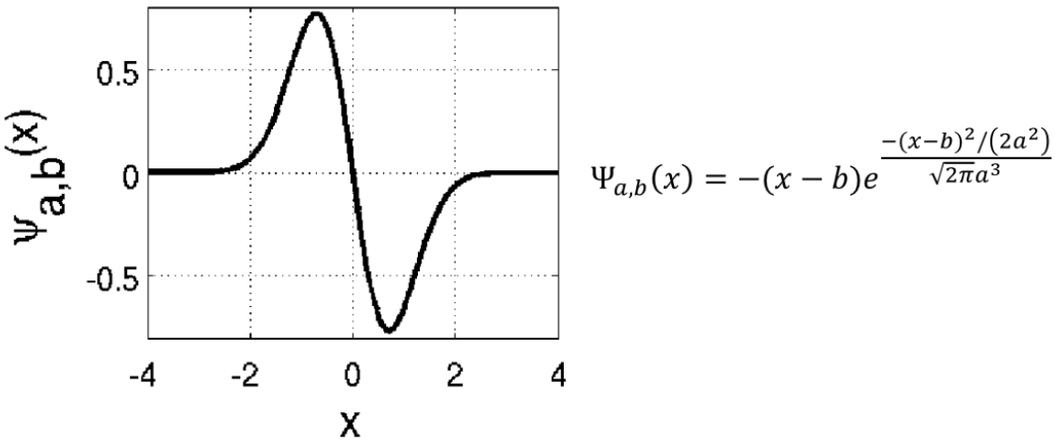

Figure 3.3: Example of wavelet function: first derivative of gaussian function.

The Discrete Wavelet Transform (DWT) provides a time-frequency representation of a signal by decomposing it into different frequency bands using scaling and wavelet functions. It iteratively applies these functions to the signal, capturing its frequency content at several levels of detail. This multi-scale decomposition allows for efficient analysis of signals in different frequency bands [53, 96].

The DWT is the discrete form of Continuous Wavelet Transform (CWT) given in the following equation:

$$C(a,b) = \int_{-\infty}^{+\infty} x(t)\psi_{a,b}^{*}(t)dt \tag{3.1}$$

Here, $x(t)$ is the signal, a and b are respectively the dilatation and the translation of the wavelet, and $\psi^{*}(t)$ is the complex conjugate of the analysing mother wavelet, which can be of various types such as Haar, Daubechies, Symlet etc. [97].

To define the DWT, the following assumptions are made:

$$b = 2^{-s} \quad a = 2^{-s}l \tag{3.2}$$

Where l describes the shifting parameter and s the scale parameter ($l = 0, 1, 2...$; $s = 0, 1, 2...$). By discretising the signal $x(t)$ and using the above formulas, we obtain the DWT as follows:

$$W(l, s) = 2^{\frac{s}{2}} \sum_{n} x(n)\psi\left(2^s n - l\right) \tag{3.3}$$

The main objective of the DWT is to decompose a signal into different resolutions using low-pass and high-pass filters. The decomposition equations are as follows:

$$A(k) = \sum_{n} x(n)h(2k - n) \tag{3.4}$$

$$D(k) = \sum_{n} x(n)g(2k - n) \tag{3.5}$$

In these equations, $x(n)$ denotes the original signal, $h(n)$ is the half-band low-pass filter, $g(n)$ is the half-band high-pass filter, $A(k)$ represents the approximation coefficients, and $D(k)$ represents the detail coefficients. Particularly:

- Approximation coefficients represent the low-frequency components of the signal.
- Detail coefficients represent the high-frequency components of the signal.

The DWT decomposition at level 2 can be illustrated using the block diagram shown in Figure 3.4. Depending on the desired cutoff frequency, this process can be repeated for deeper levels.

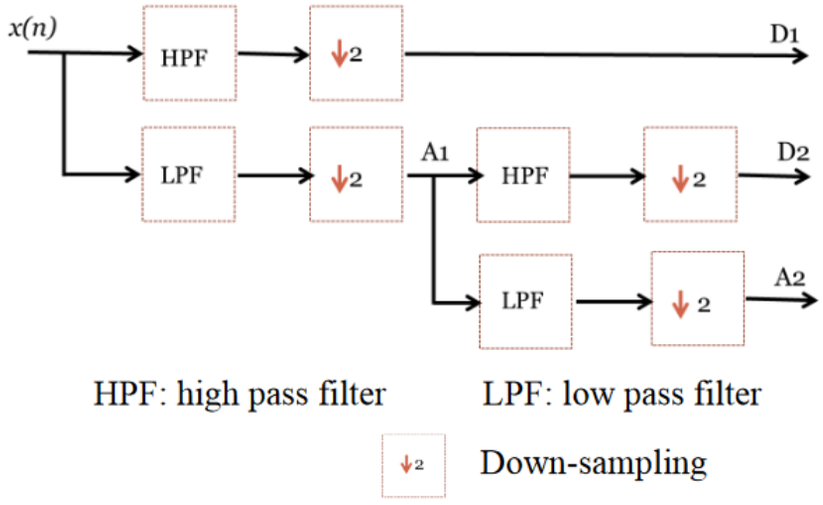

Figure 3.4: DWT decomposition model at level 2. HPF and LPF are the high-pass and the low-pass analysis filters [98]. The block $\downarrow 2$ represents the down-sampling operator by a factor of 2. The input signal $x(n)$ is recursively decomposed into a total of three sub-band signals described by: $A2$ – approximation coefficients for the coarse signal and the detailed coefficients $D1$ and $D2$ for the detailed signals of two resolutions.

Finally, the denoised signal can be reconstructed through the inverse DWT, using the updated details coefficients of DWT after estimating noise on these coefficients. Figure 3.5 shows an implementation of two-level inverse DWT [98].

In this work, the Daubechies D6 wavelet function (‘*db6*’) was chosen as the mother wavelet. This selection was based on previous studies in the literature that reported favourable results using this wavelet. Although the Daubechies functions are conceptually more complex and involve slightly more complicated computations, they have the advantage of capturing finer details that may be missed by other wavelet algorithms, such as the Haar wavelet algorithm [52, 99].

- The 9th-level *approximation* subband, corresponding to the frequency range of 0-0.351 Hz, primarily contains the baseline wander. So, it was not used in the reconstruction of the denoised signal.
- Information beyond 45 Hz in the ECG signal was deemed to be of less significance. Consequently, the first and second-level *detail* coefficients, representing frequency bands of 90-180 Hz and 45-90 Hz, respectively, were not included in the reconstruction process of the denoised ECG.

All in all, for the denoising procedure, only the detail signals from the 3rd to the 9th levels were used, while all other sub-band coefficients were replaced with

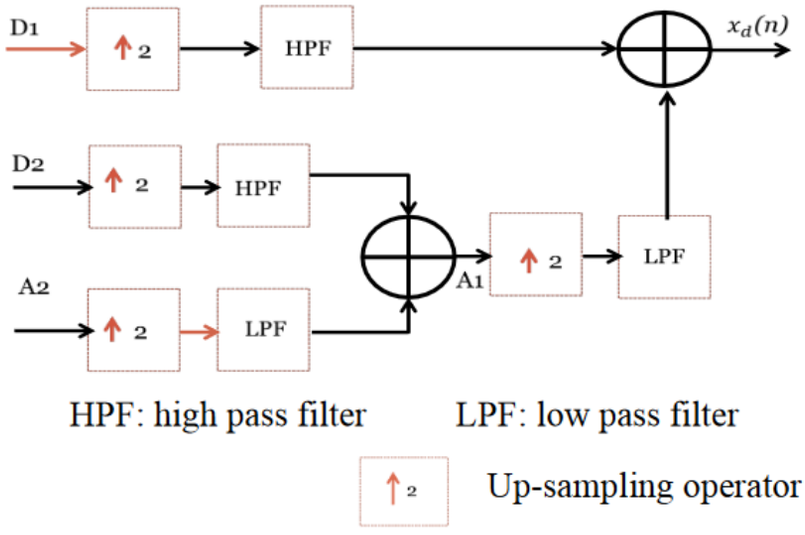

Fig. 5. IDWT block

Figure 3.5: Inverse DWT. HPF and LPF are the high-pass and low-pass analysis filters [98]. The block ↑ 2 represents the up-sampling operator by a factor of 2. Signals of the various sub-bands are recursively combined to reconstruct the output signal $x_d(n)$

zeros. These selected sub-bands were employed in the computation of the inverse wavelet transform, leading to the generation of the denoised ECG signal [100].

3.3.3 ECG Segmentation

The segmentation process was carried out by following these steps, as outlined in Algorithm 1:

1. Identification of R-peaks using the Pan-Tompkins algorithm [101].

2. Calculation of the time interval between the current R-peak and the previous R-peak ($T1$) and between the next R-peak and the current R-peak ($T2$).

3. Segmentation of the heartbeat by considering the interval (I) as the minimum value between $T1/2$ and $T2/2$.

4. Beat stretching to achieve a fixed length of 260 samples. This value was chosen considering that the RR interval falls approximately between 0.7 and 1.2 seconds [29]. Therefore, considering a worst-case scenario with an RR interval of 0.7 seconds, a heartbeat would have a duration of approximately

260 samples, given the sampling frequency of MIT-BIH DB signals equal to 360 Hz.

The implemented segmentation ensures that there is only one R-peak for each heartbeat, regardless of the subject's heart rate value.

Algorithm 1 MIT-BIH DB Heartbeat Segmentation Algorithm

Require: MIT-BIH DB signals
Require: Beat annotations
for $i = 1$ **to** length(mitdbs) **do**
    ▷ Read sig
    ▷ Wavelet-based denoising of sig
    ▷ Resampling of sig to 128 Hz
    ▷ R-peaks detection through Pan-Tompkins algorithm: R_{pos}
    for $j = 2$ **to** size$(R_{pos}) - 1$ **do**
        Compute $T_1 = R_{pos}(j) - R_{pos}(j-1)$
        Compute $T_2 = R_{pos}(j+1) - R_{pos}(j)$
        Compute Interval as $I = \min\left(\frac{T_1}{2}, \frac{T_2}{2}\right)$
        Beat segmentation: beat = signal $(R_{pos}(j) - I : R_{\text{pos}}(j) + I)$
        ▷ Identifies the AAMI EC57 category of beat based on its record
    end for
end for

A modified version of the Pan-Tompkins algorithm was implemented to detect R-peaks, excluding the filtering phase as it was performed earlier. Pan-Tompkins is a widely used algorithm for the real-time detection of QRS complexes and consists of the following stages [48, 101], graphically depicted in Figure 3.6:

1. *Derivative stage*: provides information about the slope of the QRS complex.

2. *Squaring*: each signal sample is squared, making all points of the signal positive and emphasising higher frequency components, particularly the ECG frequencies.

3. *Moving window integration (MWI)*: provides information about the waveform characteristics and the slope of the R-wave.

4. *Threshold adjustment*: a dual-threshold technique is employed. The higher threshold is used for initial signal analysis, while the lower threshold is activated only if no QRS complex is detected within a specific time interval. The thresholds are automatically adjusted; lower thresholds indicate an improved signal-to-noise ratio.

5. *Average R-R interval adjustment*: two averages of the R-R interval are calculated. The first average considers the eight most recent beats, while the second average considers the eight most recent beats with R-R intervals falling within certain limits. This approach allows for rapid adaptation to changes and cardiac irregularities.

6. *T-wave identification*: if an R-R interval is shorter than 360 ms, it is evaluated whether the current QRS complex has been correctly identified or represents a T-wave. If the slope of the waveform is lower than half of the previous QRS complex, it is identified as a T-wave; otherwise, it is considered a QRS complex.

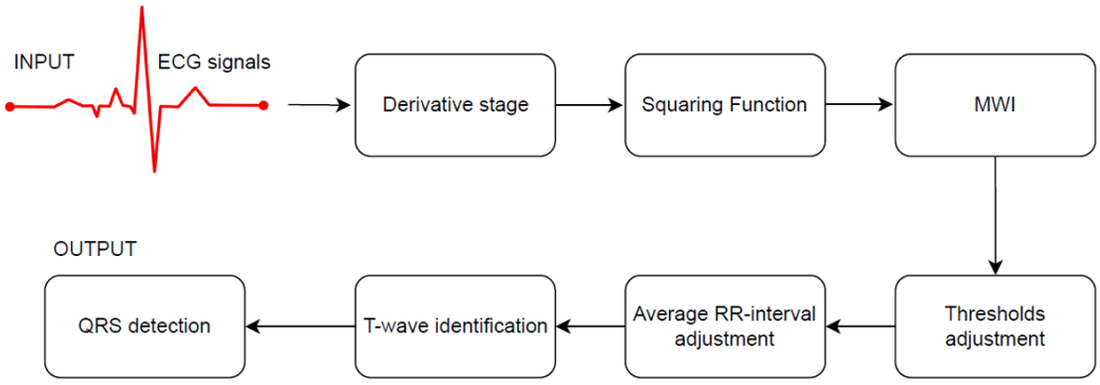

Figure 3.6: Block diagram of the Pan-Tompkins algorithm.

3.3.4 ECG Normalization

Each heartbeat is normalised using Z-score normalisation to address the issue of amplitude scaling and eliminate the offset effect before inputting the heartbeats into the CNN for training and testing. This is necessary because the raw data exhibits a wide range of values, both depending on acquisition parameters and on the patient. Normalisation techniques are applied to standardise these values by compressing the original data range to a more coherent interval. This normalisation process enhances the gradient flow in the network during gradient descent, leading to faster convergence rates [73, 87]. Given x as the segmented heartbeat, the normalised x is computed as:

$$x_{\text{norm}} = \frac{x - \mu}{\sigma} \tag{3.6}$$

Where μ and σ are respectively the mean value and standard deviation of data.

3.4 Addressing Class Imbalance: Strategies for Handling an Unbalanced Dataset

One of the significant challenges in classifying ECG anomalies is the highly imbalanced dataset. In fact, the number of abnormal heartbeats is significantly lower compared to normal heartbeats. This imbalance makes it difficult to train an effective deep-learning model with many parameters using small datasets with disease labels [49]. To address this issue, two main methods are commonly employed:

1. *Data augmentation*: This involves generating synthetic training datasets using generative models such as variational Autoencoders or Generative Adversarial Networks. Alternatively, simple techniques like altering samples through amplitude scaling can also be used.

2. *Using specific loss functions*: one example is the Focal Loss (FL), designed to give more importance to the minority class samples during training. This helps to mitigate the impact of class imbalance in the dataset.

Both methods have been implemented in this thesis work. Specifically, regarding data augmentation, the method proposed by Acharya et al. [71] was chosen, where synthetic data is generated based on Z-score normalisation. They varied the standard deviation and mean of the Z-scores from the original normalised ECG segments. The specific implementation details of the scaling method are not mentioned, but it seems that a randomly selected scale factor was applied to each segment. In the present work, random scale factors were chosen within a range that spans the minimum to maximum values of the mean and standard deviation calculated from the heartbeats in the entire database.

This method, although simple, presents some significant limitations:

- The synthetically generated heartbeats will not have a zero mean and unit standard deviation like the originally normalised heartbeats in the database. This could introduce bias in the learning of the network.

- This type of synthetic data generation does not take into account the physiological principles underlying the ECG signal. A more interesting approach, using amplitude scaling as well, is presented in the work of Do et al. [102]. In their approach, the characteristic peaks of the ECG (e.g., P, Q, R, S, T) are treated differently, and the scaling factor is decided in collaboration with a cardiologist.

Due to the abovementioned limitations, it was decided to proceed with the unbalanced dataset while implementing a specific cost-sensitive loss function, described in more detail in paragraph 3.6.

3.5 CNN Architecture

A 1-dimensional CNN with nine layers was employed for heartbeat classification. The architecture of the CNN model, adapted from the work of Acharya et al. [71], is summarised in Table 3.1. Additionally, Figure 3.7 provides a graphical representation of the model.

Table 3.1: Architecture of the proposed CNN model [71].

Layers	Type	# of Neurons	Kernel size for Each Output Feature Map)	Stride
0-1	Convolutional	258 x 5	3	1
1-2	Max-Pooling	129 x 5	2	2
2-3	Convolutional	126 x 10	4	1
3-4	Max-Pooling	63 x 10	2	2
4-5	Convolutional	60 x 20	4	1
5-6	Max-Pooling	30 x 20	2	2
6-7	Fully-Connected	30	-	-
7-8	Fully-Connected	20	-	-
8-9	Fully-Connected	5	-	-

Excluding the input layer, which has a size of 260 (corresponding to the number of samples in the segmented heartbeats), the network comprises nine layers with the following characteristics:

- *Three convolutional layers*: Every convolutional layer (layers 1, 3, and 5) convolves its respective kernel, which has a size of 3, 4 and 4, respectively. The convolution operation is performed using the equation below:

$$x_n = \sum_{k=0}^{N-1} y_k f_{n-k} \tag{3.7}$$

  Here, y is the signal, f is the kernel, and N is the number of elements of y. The kernel is initialised using the Xavier initialisation [103]. The output vector

(or feature map) is denoted as x. The kernel size was determined through a brute force technique, and the stride (i.e., the step size when sliding the kernels across the input data) was set at 1. Finally, the ReLU function is used as the activation function for these three convolutional layers and the first two fully-connected layers.

- *Three max-pooling layers*: After every convolutional layer, a max-pooling operation (with a stride set at 2) is applied to the feature maps with the aim of reducing its size.

- *Three fully-connected layers:* These layers consist of 30, 20, and 5 output neurons, respectively. In the final layer, before computing the loss, the softmax activation function is applied to the output to squash the values within the range of [0, 1]. The softmax function is defined as:

$$\widehat{y}^{(i)} = \frac{\exp\left(z^{(i)}\right)}{\sum_{j=1}^{C} \exp\left(z^{(j)}\right)} \tag{3.8}$$

  Where C represents the number of ECG beat categories (five in this case), and $y(i)$ denotes the class probability assigned by the CNN to the input feature vector $z(i)$.

3.6 Training Phase

3.6.1 Training Parameters

Choosing hyperparameters – e.g., parameters set before model training that cannot be learned during the training process – is a crucial step in developing effective machine learning models. The optimal values for these parameters can vary depending on the dataset, model complexity, and available computational resources. Therefore, tuning hyperparameters often involves an iterative process of running experiments and evaluating performance on a validation set. In this work, some hyperparameters were selected based on previous research, while others were obtained using the *grid search technique*. This technique involves systematically testing different combinations of hyperparameters to determine the combination that yields the best model performance [104].

The CNN model was trained with the following parameters:

- *Optimization algorithm*: Adam (Adaptive Moment Estimation) with a variable Learning Rate (LR) based on the training epoch. The LR is an important

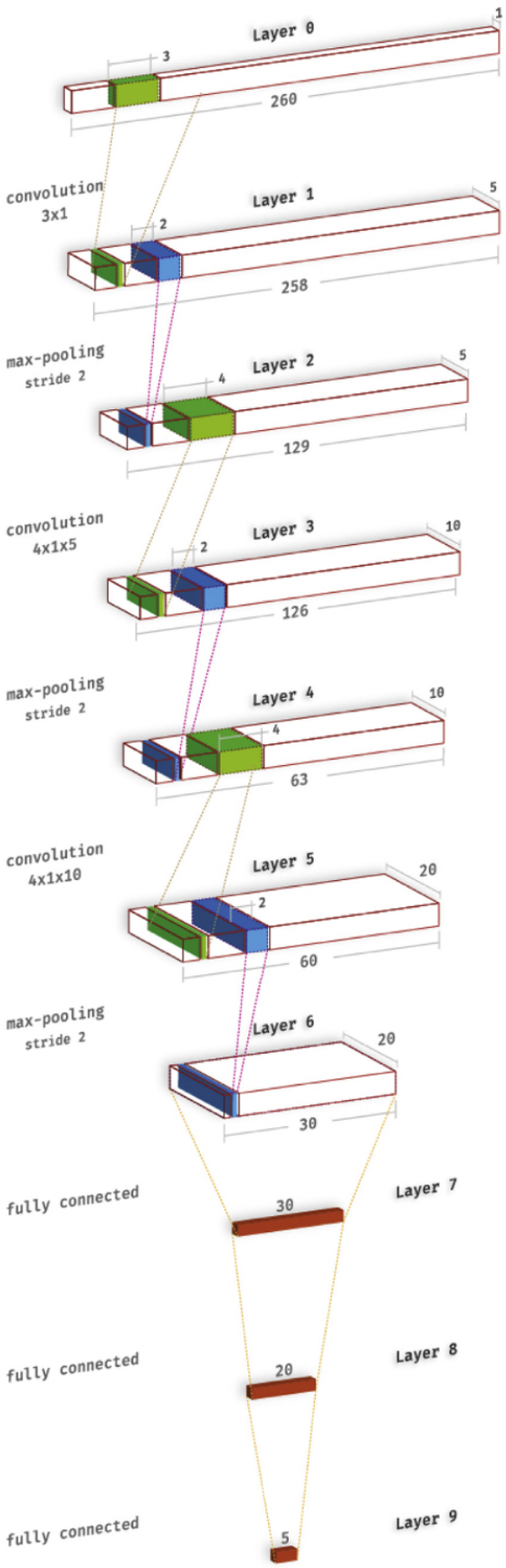

Figure 3.7: Architecture of the proposed CNN model [71].

hyperparameter that controls the change applied to the model weights in response to the estimated error during each update [105]. The initial LR (lr_0) in this work was determined using the grid search technique. The LR for the current epoch i out of the total number of training epochs N is calculated using the equation provided:

$$lr = lr_0 \times \left(1 - \frac{i}{N}\right)^{0.9} \tag{3.9}$$

The progressive reduction of the learning rate helps accelerate the neural model training in the initial epochs while preventing weight instability and overfitting in the later epochs.

- *Number of epochs*: The CNN was trained over 20 epochs, where each epoch represents a complete cycle of presenting all training data to the model. The backpropagation algorithm was used for training [106].
- *Loss function*: The CNN model used the Categorical FL as the loss function to handle the unbalanced dataset. The Categorical Focal Loss, introduced by Lin et al. [88], is a variant of the Cross-Entropy Loss that assigns different weights to each sample based on its classification error. It focuses on the problematic and less-represented classes by reducing the contribution of samples already correctly classified by CNN. The Categorical FL can be calculated through Equation 3.10, where $\hat{y}$ represents the class probability calculated in the output layer using the softmax function, and γ is the focusing parameter.

$$\mathrm{FL}(\widehat{y}) = -(1 - \widehat{y})^{\gamma} \cdot \log(\widehat{y}) \quad \gamma \geq 0 \tag{3.10}$$

Compared to the classical Cross-Entropy function (Equation 3.11), the Categorical Focal Loss introduces a modulating factor, $(1 - \hat{y})^{\gamma}$, that keeps the loss function almost unaffected for misclassified examples with small class probabilities ($\hat{y}$). As the model's confidence increases, the modulating factor tends to 0, down-weighting the loss value for well-classified examples.

$$\mathrm{CE}(\widehat{y}) = -\log(\widehat{y}) \tag{3.11}$$

The focusing parameter γ rescales the modulating factor, giving more weight to hard examples than easy ones and reducing their impact on the loss function, as shown in Figure 3.8.

Different values of the focusing parameter γ were tested during the training process using the grid search technique. The optimal value was determined based on performance evaluation. Figure 3.9 provides a visual representation of how the loss value is calculated during the training process.

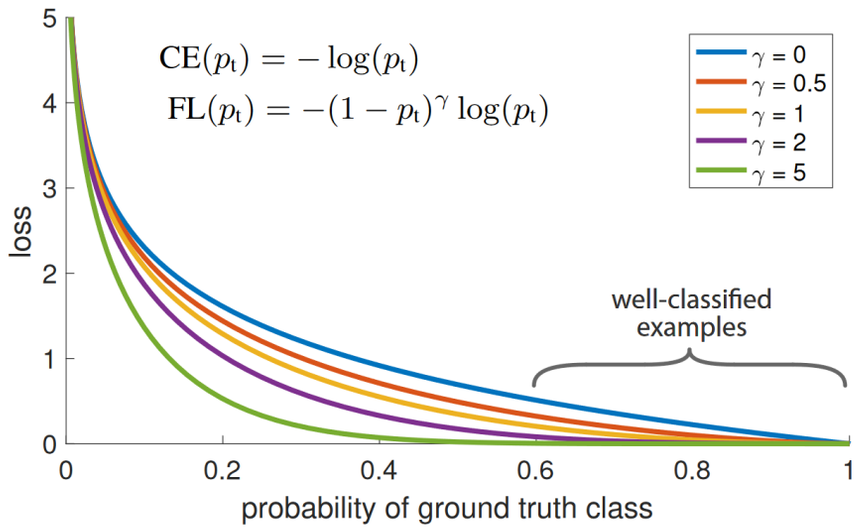

Figure 3.8: Effect of the focusing parameter γ on the focal loss. When $\gamma = 0$, Focal Loss is equal to cross-entropy loss [88].

Finally, a comprehensive grid search technique optimised the hyperparameters γ (focusing parameter), batch size, and initial learning rate. Table 3.2 displays the attempted values for these parameters during the grid search process. The grid search involved testing various combinations of these parameters to find the optimal values.

In the end, a total of 90 networks were saved, considering all possible combinations of the mentioned parameters. The performance of each network was evaluated on the test set, and the best-performing network was selected and saved.

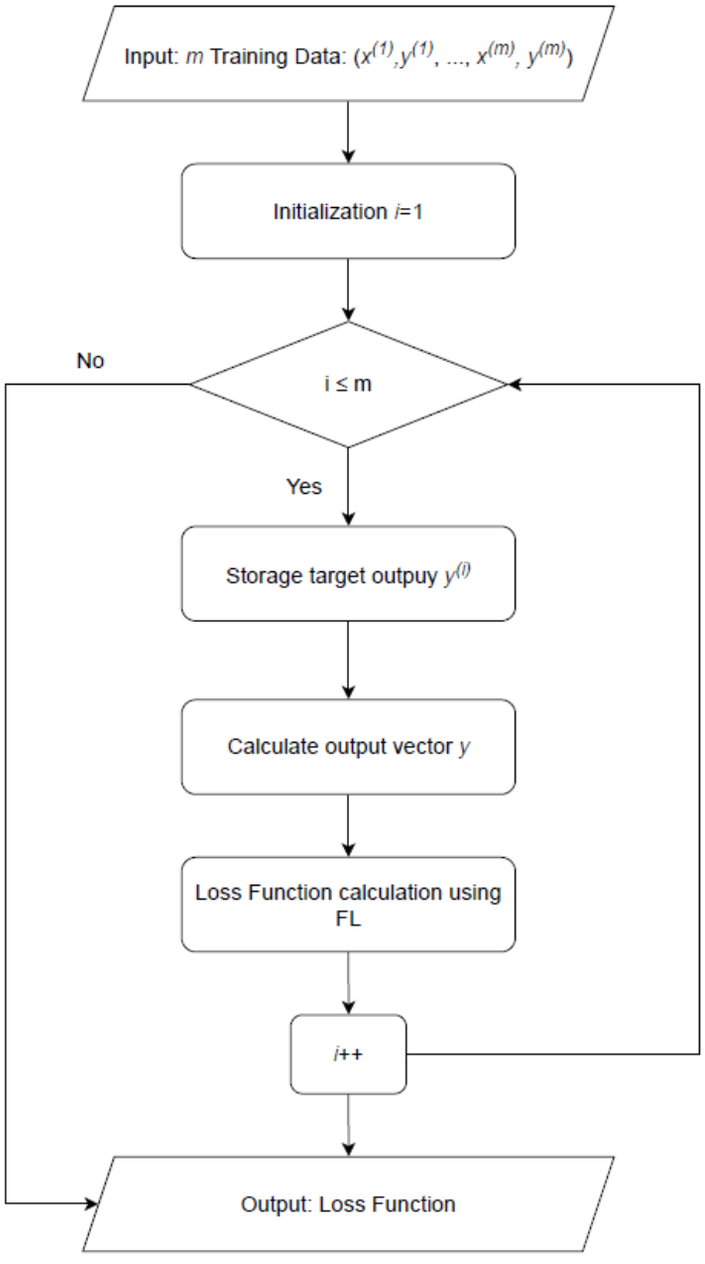

Figure 3.9: Block diagram showing how the loss is calculated using Focal Loss.

Table 3.2: Hyperparameters attempted during the grid search technique.

γ	Learning Rate	Batch Size
0.0	0.01	32
0.5	0.01	64
1.0	0.001	128
2.0		256
3.0		512
4.0		

3.6.2 Dataset Division and Cross-Validation

Cross-validation and train/test split are essential techniques for evaluating the performance of a model on unseen data. This work employed a nested ten-fold cross-validation approach to assess the model's performance. Thus, the dataset was divided into ten folds, ensuring that each fold contained an equal distribution of segments and conditions within the heartbeats (stratified sampling).

During the cross-validation process, the model was reinitialised for each fold, with one fold as the test set and the remaining nine for training. This process was repeated ten times, with each fold serving as the test set once. The model's performance was then averaged across all ten folds for an overall evaluation.

To monitor the model's training progress, 30% of the Training Set was set aside for validation. This validation set allowed for the examination of the model's performance during the training process. Details regarding the ten-fold cross-validation methodology can be found in Figure 3.10.

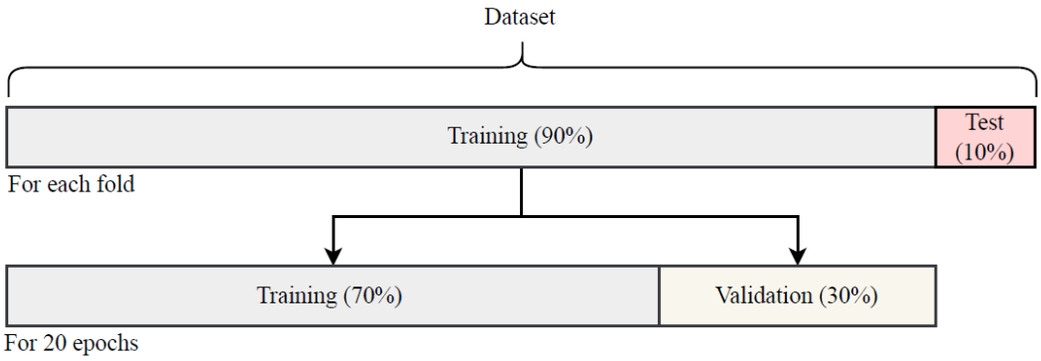

Figure 3.10: Dataset division in Training, Test and Validation Set.

In this work, the validation phase occurs at the end of each epoch during the training process. During this phase, the value of the loss function on the Validation Set (validation loss) is recorded. The model is saved if the validation loss improves compared to the previous epoch. Otherwise, the training proceeds to the next epoch.

An Early Stopping technique was implemented to prevent overfitting and avoid unnecessary training. The training process is terminated if there is no improvement in the validation loss for five consecutive epochs. This helps to ensure that the model is trained at the point where it no longer improves its performance on unseen data. By employing Early Stopping, the training process can be efficiently stopped when there is no significant progress in the model's validation loss, saving computational resources and preventing overfitting as it helps find the optimal

point of training where the model achieves good generalisation performance on unseen data.

3.7 Test Phase

In evaluating the 90 saved models, the recommended evaluation metrics by the AAMI were used, as described in paragraph 2.4.2. Specifically, on the Test Set, the following metrics were evaluated with the aim of:

- Distinguishing 'S' type beats from other beats (considered metrics can be found in Table 3.3(a))
- Distinguishing 'V' type beats from other beats (considered metrics can be found in Table 3.3(b))
- Distinguish the five AAMI classes (considered metrics can be found in Table 3.4)

Table 3.3: a. **Evaluation metrics proposed by AAMI for the classification of 'S' beats**; b. **Evaluation metrics proposed by AAMI for the classification of 'V' beats**. Abbreviations: ACC: Accuracy; F: Fusion heartbeats; FN: False Negatives; FP: False Positives; N: Normal heartbeats; +P: Positive predictivity; Q: Unknown heartbeats; Se: Sensitivity; Sp: Specificity; S: Supraventricular ectopic heartbeats; V: ventricular ectopic beats; TN: True Negatives; TP: True Positives. Modified from [62]

True class \ Predicted class	N	S	V	F	Q
N	Nn	Ns	Nv	Nf	Nq
S	Sn	Ss	Sv	Sf	Sq
V	Vn	Vs	Vv	Vf	Vq
F	Fn	Fs	Fv	Ff	Fq
Q	Qn	Qs	Qv	Qf	Qq

$$TN_V = Nn + Ns + Nf + Sn + Ss + Sf + Sq + Fn + Fq + Qn + Qs + Qf + Qq$$

$$FN_V = Vn + Vs + Vf + Vq$$

$$TP_V = Vv$$

$$FP_V = Nv + Sv$$

$$Se_V = TP_V/(TP_V + FN_V)$$

$$+P_V = TP_V/(TP_V + FP_V)$$

$$FPR_V = FP_V/(TN_V + FP_V)$$

$$ACC_V = \frac{TP_V + TN_V}{TP_V + TN_V + FP_V + FN_V}$$

(a)

True class \ Predicted class	N	S	V	F	Q
N	Nn	Ns	Nv	Nf	Nq
S	Sn	Ss	Sv	Sf	Sq
V	Vn	Vs	Vv	Vf	Vq
F	Fn	Fs	Fv	Ff	Fq
Q	Qn	Qs	Qv	Qf	Qq

$$TN_S = Nn + Nv + Nf + Nq + Vn + Vv + Vf + Vq + Ff + Fq + Qn + Qv + Qf + Qq$$

$$FN_S = Sn + Ss + Sf + Sq$$

$$TP_s = Ss$$

$$FP_S = Ns + Vs + Fs$$

$$Se_S = TP_S/(TP_S + FN_S)$$

$$+P_S = TP_S/(TP_S + FP_S)$$

$$FPR_S = FP_S/(TN_S + FP_S)$$

$$ACC_S = \frac{TP_S + TN_S}{TP_S + TN_S + FP_S + FN_S}$$

(b)

Table 3.4: Evaluation Metrics to distinguish the five AAMI classes, modified from [62]. Please refer to the abbreviation in Table 3.3.

		Predicted class					
		N	S	V	F	Q	Sum
True class	N	Nn	Ns	Nv	Nf	Nq	ΣN
	S	Sn	Ss	Sv	Sf	Sq	ΣS
	V	Vn	Vs	Vv	Vf	Vq	ΣV
	F	Fn	Fs	Fv	Ff	Fq	ΣF
	Q	Qn	Qs	Qv	Qf	Qq	ΣQ
							Σ

$$TN = Nn$$

$$TP_V = Vv$$

$$TP_s = Ss$$

$$TP_F = Ff$$

$$TP_Q = Qq$$

$$Sp = TN/\Sigma N$$

$$Se_V = TP_V/(TP_V + FN_V)$$

$$Se_S = TP_S/(TP_S + FN_S)$$

$$Se_F = TP_F/\Sigma F$$

$$Se_Q = TP_Q/\Sigma Q$$

$$ACC = \frac{TN + TP_s + TP_V + TP_F + TP_Q}{\Sigma}$$

It is worth noting that, according to Table 3.3, the calculation of positive predictivity for V-type beats ($+P_V$) does not penalise false positives related to F and Q-type beats. Similarly, false positives of Q-type beats are not included in the calculation for positive predictivity of S-type beats ($+P_S$). By considering these specific metrics, the evaluation provides a comprehensive assessment of the model's performance in distinguishing different types of beats and aligns with the recommendations provided by the AAMI.

Finally, to evaluate the best model, it was decided to identify the top 10 models for the identification of V-type beats and the top 10 models for the identification of S-type beats based on the following indexes:

$$\begin{aligned} \text{index}_V &= +P_V + Se_V \\ \text{index}_S &= +P_S + Se_S \end{aligned} \tag{3.12}$$

Of these two sets of models, the intersection was made. Finally, of the remaining models, the most accurate one was chosen as the best.

Chapter 4

Development of a Method for the Adaptation of a Pre-Trained CAD System to Hi-ECG Signal

In the previous chapter, an example of the design and development of a CAD system for classifying cardiac anomalies – trained on a freely available public database – was presented. However, this system does not apply to Hi-ECG device signals as they are morphologically different from the signals used to train the model. Therefore, in the absence of an appropriate database of Hi-ECG signals acquired with the device and properly labelled, this chapter proposes a methodology to adapt the signals acquired with the analysed device to a pre-trained CAD system using a public database, a 12-lead ECG DB. To achieve this, the objective is to convert the wearable device signals to a "standard" morphology, such as that obtained from the three Einthoven limb leads. In this way, the Hi-ECG signals are transformed to have a morphology similar to those used for training the CAD system.

The proposed methodology involves a signal pre-processing phase, including denoising, a step to identify the device placement on the user's chest, the conversion of Hi-ECG signals to a unique configuration (specifically, the one recommended by the user manual), and finally, the conversion of these signals to "standard" signals.

The proposed method is intended to be appropriately validated in future work, where Hi-ECG signals with anomalies will be available for analysis.

4.1 Proposed Pipeline

This chapter will describe the steps of the proposed methodology to adapt a pre-trained CAD system to Hi-ECG device-acquired signals.

The need for developing such a methodology arises from the lack of a database containing appropriately labelled cardiac signals acquired with this wearable device. Therefore, the methodology suggests preprocessing steps for Hi-ECG signals to convert them into "standard" signals. Specifically, the aim is to reconstruct the three standard Einthoven leads (obtained by applying electrodes to the limbs) from the Hi-ECG signals, which, as discussed in the previous section, are acquired with a non-standard positioning.

At this stage, the methodology proposes classifying the ECG signals using a CAD system pre-trained on 12-lead signals so that the morphology of the input signals to the system is as similar as possible to those used for training the network. This would enable the classification of any cardiac anomalies recorded with the Hi-ECG device using a CAD system without needing a custom-built database specifically for this device.

The pipeline for this task is illustrated in Figure 4.1.

In general, the proposed steps include:

1. *Noise removal*: This phase is necessary to extract the ECG signal from background noise.
2. *Patch Positioning Identification*: In this phase, the type of configuration in which the subject has positioned the Hi-ECG device on the chest will be identified.
3. *Misplacement Correction*: If any misplacement of the Hi-ECG device is identified, it will be corrected in this phase.
4. *Conversion of signals to Configuration 1*: Signals related to Configurations 2 and 3 are converted so that their morphology is similar to those acquired in Configuration 1.
5. *Conversion to "Standard" Configuration*: In this phase, various approaches will be proposed to achieve the described objective.
6. *Classification of cardiac anomalies* using a CAD system pre-trained with a 12-lead ECG database.

It should be noted that the proposed methodology has been explored and validated only up to Step #4. In future developments of this work, the focus will be on Steps #5 and #6.

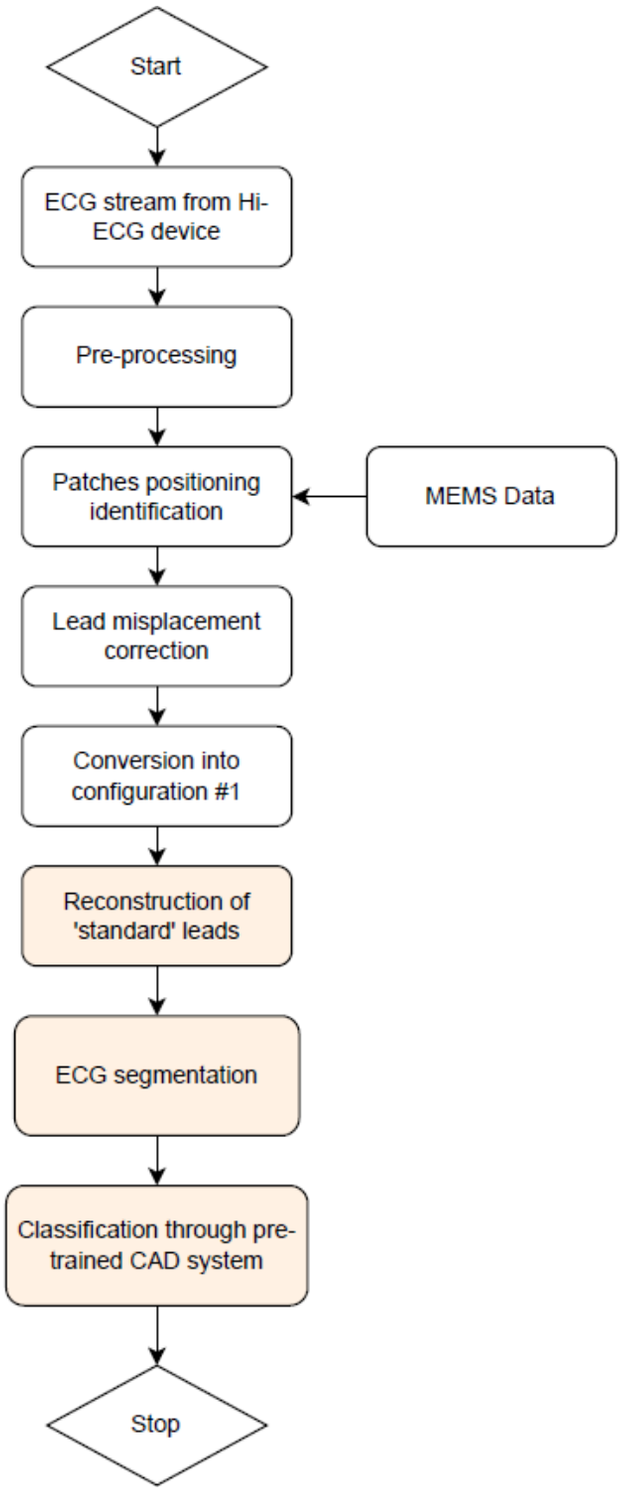

Figure 4.1: Proposed pipeline for the second task of the thesis. Colour boxes indicate steps for which no implementation is provided in this work.

4.2 Noise Removal

This phase is performed differently from what was described in Section 3.3.1 due to the following reasons:

- The user can select the sampling frequency of the signals acquired with the Hi-ECG device. In this section, we will focus on two scenarios: when the sampling frequency is set to 128 Hz (the default value of the device) and when it is set to 512 Hz.
- The signals acquired with the Hi-ECG device are inherently noisier compared to the signals in the MIT-BIH database, which are recorded under more controlled conditions and for shorter durations (30 minutes compared to durations that can reach up to 48 hours with the Hi-ECG device signals) [84].

Due to the reasons above, it was chosen to implement a cascaded filter approach to address baseline wander removal and high-frequency noise that may affect the signal. The literature suggests that a bandwidth ranging from 0.05 Hz (which can be relaxed up to 0.67 Hz for digital linear filters with zero-phase distortion) to 40 Hz is suitable for ensuring ECG quality and facilitating clinical interpretation [100, 107]. Therefore, the implemented filters aim to attenuate noise and artefacts outside this frequency range while preserving the informative components of the ECG signal.

As a first step, wavelet-based denoising was applied primarily for the removal of baseline wander in the following manner:

- *For signals sampled at 128 Hz*: seven decomposition levels were chosen. This ensured that the 7th level approximation subband, which corresponds to the frequency range of 0-0.5 Hz, predominantly representing the baseline wander, was excluded from the denoised signal reconstruction. Therefore, only the detail signals were used to compute the inverse wavelet transform and obtain the denoised ECG signal.
- *For signals sampled at 512 Hz*: In this case, the number of levels was set to nine, ensuring that the 9th level approximation subband, covering frequencies from 0 to 0.5 Hz, was not used for denoising. Additionally, the detail coefficients at the first and second levels, corresponding to the frequency bands of 128-256 Hz and 64-128 Hz, were excluded from the denoised signal reconstruction.

Subsequently, to remove high-frequency noise, a windowed FIR filter with an order of 30 and a cutoff frequency of 40 Hz was applied [108]. This filter helps attenuate noise components above 40 Hz, improving the overall quality of the denoised ECG signal.

4.3 Patch Positioning Identification

This phase of the methodology aims to identify the placement type of the Hi-ECG device on the patient's chest. As mentioned in Section 1.2.2, the device's user manual specifies three configurations to position the device (shown in Figure 4.2). Identifying the configuration type serves the following purposes:

1. Correct any misplacement errors related to the central body of the Hi-ECG device. It is highly likely that the user, misinterpreting the instructions from the user manual, may position the central body of the device in the opposite direction as indicated.

2. Proceed with the subsequent phase of the methodology, which involves converting configurations 2 and 3 (Figure 4.2b and Figure 4.2c) into Configuration 1 (Figure 4.2a).

The placement type identification was considered a ternary classification problem, where the classes correspond to the three configurations from the user manual. The chosen approach for this task is using a Multilayer Perceptron (MLP) network, a type of feedforward NN consisting of multiple layers of interconnected nodes or neurons. The MLP network was selected because, in addition to successfully addressing intricate and diverse classification problems, its simplicity of architecture makes it suitable for potential integration into the device's firmware in future studies [109].

The problem consists of the following phases:

1. *Database creation*: In this phase, a database that includes ECG signals with known placement configurations is constructed.

2. *ECG signal segmentation*: The ECG signals from the database are segmented into individual beats.

3. *MLP training*: The MLP model is trained using the segmented ECG signals. The training process involves presenting the input signals to the MLP and adjusting the model's weights and biases to minimise the classification error.

4. *MLP testing*: After training, the performance of the MLP model is evaluated using a separate set of ECG signals. This testing phase assesses the model's ability to classify the placement configurations accurately.

5. *Identification and correction of misplacements*: After the patch positioning identification, Accelerometer data are used to identify any misplacements. Corrective actions can be taken to address the issue if misplacements are detected.

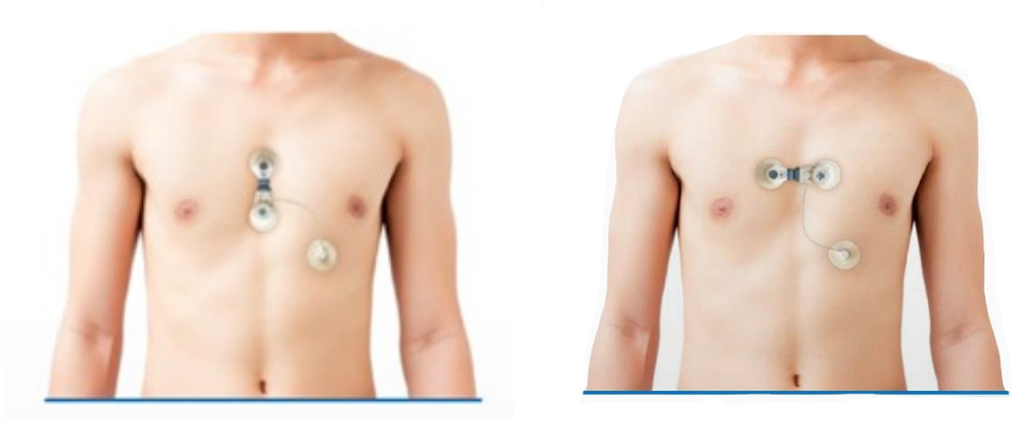

(a) Configuration #1

(b) Configuration #2

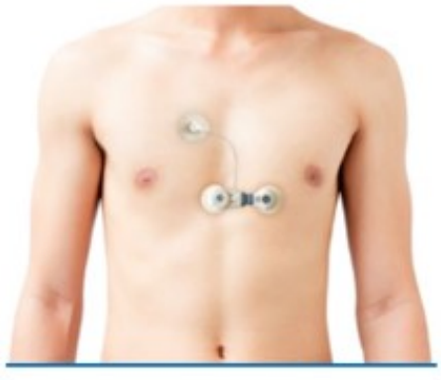

(c) Configuration #3

Figure 4.2: Placement of the wearable device, as indicated in the user manual [27]

These phases collectively form the methodology for addressing the problem of placement identification and correction using the MLP model.

4.3.1 Creation of a Hi-ECG Database

To create an appropriate dataset for training and testing the MLP, ten subjects were recruited for ECG signal acquisition using the Hi-ECG device. All subjects were asked to remain seated during the approximately 2-minutes long acquisition sessions. Multiple acquisitions were performed for each subject, simulating both correct and incorrect device placement conditions, with a sampling frequency of 512 Hz. Precisely, as shown in Figures in Appendix the device was positioned for

each subject in the following ways:

- The three manual configurations (referred to as Class 1, 2, and 3).
- The three configurations with the central body of the device inverted compared to the manual instructions (referred to as Class 4, 5, and 6).
- The three configurations with device translation (considering both correct and incorrect central unit orientation):
  - For Configuration 1, a vertical translation was considered (Class 1 and 4).
  - For configurations 2 and 3, a horizontal translation was considered (class 2, 3, 5 and 6).

For the purpose of training and testing the MLP network, Classes 4, 5, and 6 were merged with Classes 1, 2, and 3, respectively, resulting in a ternary classification.

Subsequently, as described in more detail in paragraph 4.3.6, any misplacements of the device's central unit will be identified and corrected using accelerometer data recorded during the acquisitions. The accelerometer data, sampled at 8 Hz, provides information on the orientation of the device with respect to the gravitational acceleration vector.

4.3.2 ECG Segmentation

The segmentation process of the signals acquired with the Hi-ECG device is necessary to generate the dataset used for training the MLP. This procedure considers the three recorded ECG channels. Specifically, for each channel, the same procedure described in paragraph 3.3.3 regarding the segmentation of MIT-BIH DB signals is followed, with the difference of the imposed length for each beat, which in this case is set to 200 samples.

Subsequently, the segmented beats for each channel are aligned into a single vector of 600 samples, which will serve as the input for the MLP.

The pseudo-code for the described procedure is provided in Algorithm 2

4.3.3 Training of the Multi-Layer Perceptron Network

The MLP architecture, as depicted in Figure 4.3, is composed of an initial input layer, one or more hidden layers, and an output layer. Each neuron in a hidden layer receives inputs from the neurons in the preceding layer and produces an output based on its weights and activation function. In this work, the input layer of the MLP architecture consists of 600 neurons, which matches the dimension of the input data. The number of neurons in the output layer corresponds to the

Algorithm 2 Hi-ECG Heartbeat Segmentation Algorithm

Require: Hi-ECG signals (3 channels)
Initialize empty dataset D
for channel $= 1$ **to** 3 **do**
    for each signal sig in channel **do**
        Perform denoising on sig
        Detect R-peaks in sig using Pan-Tompkins algorithm: R_pos
        for $j = 1$ **to** length(R_pos) $- 1$ **do**
            Compute $T_1 \leftarrow \text{R\_pos}(j) - \text{R\_pos}(j-1)$
            Compute $T_2 \leftarrow \text{R\_pos}(j+1) - \text{R\_pos}(j)$
            Compute interval $I \leftarrow \min\left(\frac{T_1}{2}, \frac{T_2}{2}\right)$
            Segment beat as beat $\leftarrow \text{sig}[\text{R\_pos}(j) - I : \text{R\_pos}(j) + I]$
            Append beat to dataset D
        end for
    end for
end for
Concatenate all beats in D into a single vector: dataset
Output: dataset

number of classes to be distinguished, which in this case is three. Furthermore, we employed ten neurons for the hidden layer.

The performances of the network were assessed using a nested ten-fold cross-validation approach. The ECG dataset was divided into ten equal portions, ensuring each portion contained a balanced representation of segments corresponding to the three positioning options. During the training phase, which consisted of 70 epochs, nine portions of the ECG segments were used for training, while the remaining portion was reserved for testing. This process was repeated ten times, with each iteration involving model reinitialisation and testing on a distinct subset of data.

To monitor the training progress of the models, 30% of the training set was dedicated to validation. The MLP network was trained using the backpropagation technique with a batch size of 27. The Adam optimiser was employed to expedite the learning process, with a weight decay of zero and a variable learning rate that depended on the epochs. At the end of each training epoch, the categorical Cross-Entropy loss function was evaluated on the validation set. The performance of each epoch was compared to previous epochs, and the model with the best validation loss was saved at the end of the training. Table 4.1 summarises the critical choices made for the training of the MLP network.

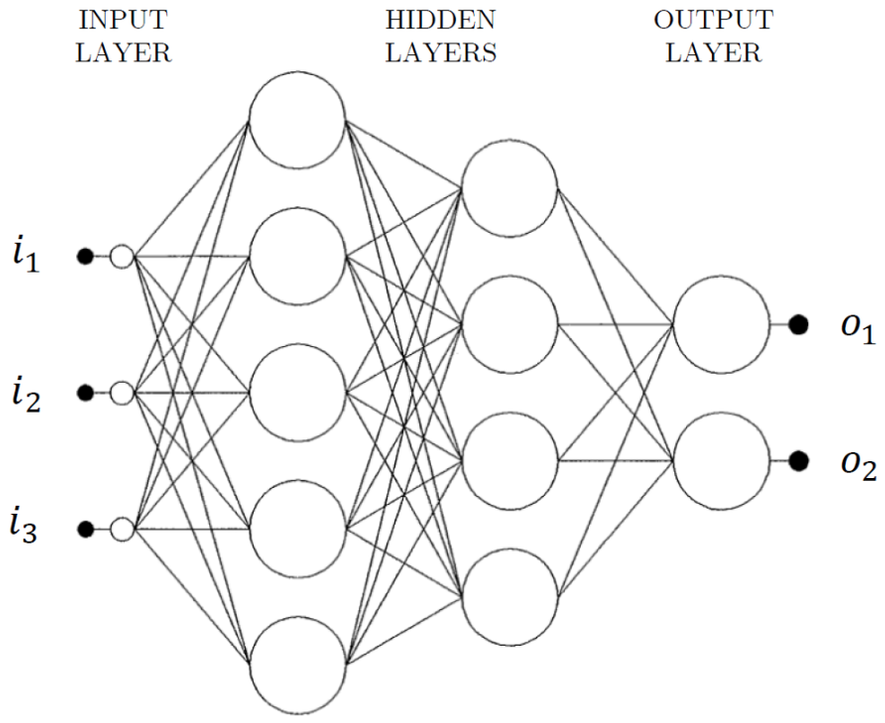

Figure 4.3: Example of architecture of a MLP network with two hidden layers, modified from [110]. In this case $\vec{i} = [i_1, i_2, i_3]$ is the input vector whereas $\vec{o} = [o_1, o_2]$ is the output vector.

4.3.4 Evaluation Metrics and Analysis of the Classification

The metrics chosen to evaluate the MLP network's performance are reported below, based on the counted True Positives (TP), True Negatives (TN), False Positives (FP) and False Negatives (FN) for every class:

$$\text{Accuracy(Acc)} = \frac{TP + TN}{TP + TF + FP + FN} \tag{4.1}$$

$$\text{Sensitivity(Sens)} = \frac{TP}{TP + FN} \tag{4.2}$$

$$\text{Specificity(Spec)} = \frac{TN}{TN + FP} \tag{4.3}$$

Table 4.1: Parameters and choices for training the proposed MLP network.

Aspect	Details
Cross-valitadion approach	Nested 10-fold
Dataset division	Stratified Sampling
Validation set size	30% of Training Set
MLP network training technique	Backpropagation
Optimization Technique	Adam
Training epochs	70
Batch size	27
Evaluation metric on Validation Set	Categorical Cross-Entropy Loss
Model selection during training	Best validation loss

4.3.5 Intended Use of the MLP

In order to determine the corresponding class for the positioning of the device associated to a recording, the following steps are performed:

1. Denoising and segmentation of the signal, as described in the previous paragraphs.

2. Use of the MLP network. Each segment will then have a predicted class by the network.

3. Considering ten consecutive segments, the most representative class value within each block was determined and assigned to it. In cases the number of segments was not a multiple of ten, zero-padding was used to ensure a consistent block size.

4. Considering all the ECG blocks results, the most representative class value was again identified, which was ultimately designated as the overall class assigned to the entire acquisition.

4.3.6 Misplacement Identification and Correction

Once the device placement has been determined, assuming the user is sitting, it is possible to detect any misplacement by examining the principal component of the acceleration recorded during the session. Considering the coordinate system shown in Figure 4.4, the principal axis of acceleration and its sign should align with the expected values based on the determined placement, as outlined in Table 4.2. If the sign is opposite to what is expected, it indicates a misplacement of the device's rigid body.

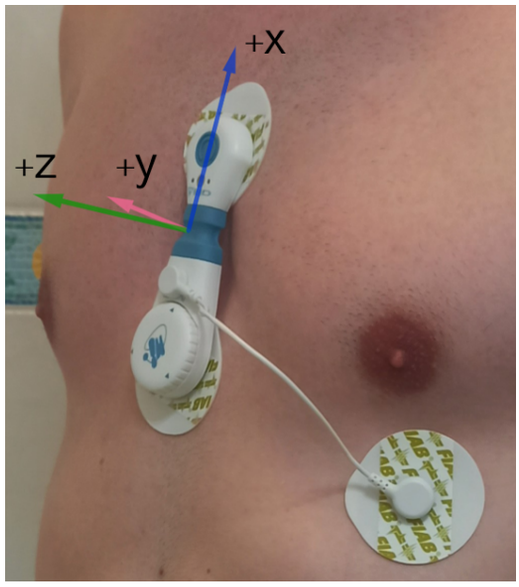

Figure 4.4: Coordinate system of the accelerometer in the Hi-ECG device.

The proposed method is valid only for users who are in a sitting or standing position while wearing the Hi-ECG device. For patients lying down, the principal component of acceleration would be along the z-axis with a positive sign in all configuration types, making it difficult to distinguish between a normal positioning condition and a misplacement.

To extend the identification of device placement to bedridden patients, an approach suggested for future development of this work consists of introducing a six-class classification, incorporating the three manual placement classes (1, 2, and 3) and the three classes where the central body is considered inverted (4, 5, 6). This extended classification would allow for the differentiation of device placement in various patient positions and accommodate a broader range of scenarios.

If a misplacement of the main body of the device is detected, the ECG data undergoes treatment to correct the misplacement. Specifically, the following steps are taken (Figure 4.5):

Table 4.2: Expected magnitudes and orientation of normalised acceleration (expressed in g) along the three axes for the three configurations when the user is sitting.

		Conf. 1		Conf. 2		Conf.3	
		Normal	Misplacement	Normal	Misplacement	Normal	Misplacement
Acc. Values on x, y, z axis (g)	x	+1	-1	0	0	0	0
	y	0	0	-1	+1	+1	-1
	z	0	0	0	0	0	0

1. The sign of lead I, which is associated with the rigid body, is inverted using the following equation:

$$I \leftarrow -I \tag{4.4}$$

2. Leads II and III are swapped, and their signs are inverted to account for lead polarity. This means that the data from the third lead is treated as if it was acquired from the second lead, and vice versa:

$$\begin{aligned} II &\leftarrow -III \\ III &\leftarrow -II \end{aligned} \tag{4.5}$$

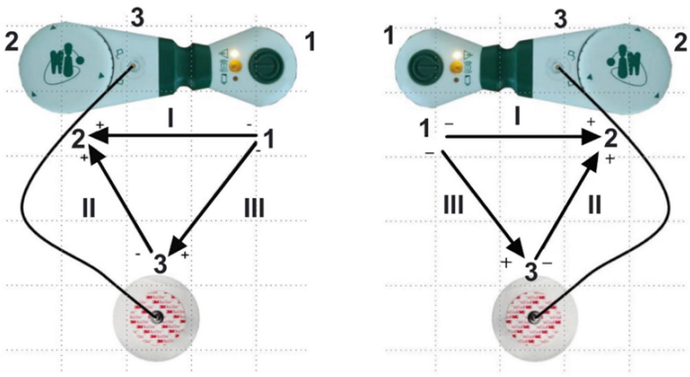

Figure 4.5: Left Panel: Hi-ECG device and lead polarities before misplacement correction; Right Panel: Hi-ECG device and lead polarities after misplacement correction.

4.4 Conversion into Configuration #1

In cases where the user has positioned the device according to Configuration 2 or 3, we chose to convert the three ECG leads so that they have a morphology similar to signals acquired according to Configuration 1, as it is the recommended configuration based on the instruction provided by the user manual of the device. This can be useful in cardiac anomaly classification problems, where the focus of the process is on the morphology of the signal. With this method, we eliminate the issue related to the device being placed in different configurations, thereby introducing additional variability to the problem, in addition to the inherent inter-patient variability.

To achieve the objective of this phase, a geometric-analytical approach based on the general theory of heart vector projection, described in the paragraph 1.3.3, was chosen. Some underlying premises of the proposed method are summarized below:

- The proposed method relies on the accurate identification of the device's placement on the user's chest in the previous step. Any misplacement of the central body must also be corrected.
- It should be noted that the general theory of vector heart projection is based on the assumptions formulated by Einthoven, as described before. In the configurations proposed by the Hi-ECG user manual, the assumption that the heart is positioned at the centre of the sampling volume does not hold. Therefore, it is important to consider that the proposed method for converting the signals to Configuration 1 is only valid in a reference system related to the Hi-ECG device.

- The signals considered for this phase are the same as those described at the beginning of the chapter, where denoising is applied. However, the analysis is conducted on the signals in their entirety, without applying the segmentation process described before. Normalization is also not applied.

The proposed method is based on the following steps:

1. *Obtaining the system geometry*: Based on the acquisitions made on each user placing the Hi-ECG device on the patient's chest in the three configurations recommended by the user manual, photos were obtained and used for the calculation of the angle between the corresponding line of each lead and the horizontal line.

   With this procedure, a set of three angles – named A, B and C were obtained. The sets are averaged (Equation 4.6) for all the subjects to find the system geometry of the three configurations, which will be used in the subsequent steps.

$$\begin{aligned}
[A_1, B_1, C_1] &= \sum_{s=1}^{10} [A_{s,1}, B_{s,1}, C_{s,1}] \\
[A_2, B_2, C_2] &= \sum_{s=1}^{10} [A_{s,1}, B_{s,1}, C_{s,1}] \\
[A_3, B_3, C_3] &= \sum_{s=1}^{10} [A_{s,3}, B_{s,3}, C_{s,3}]
\end{aligned} \tag{4.6}$$

   Here, A, B and C are the set of angles for the three configurations and s is the number of subjects considered for the calculation.

2. *Segmenting the ECG signal into the three characteristic waves*:

   - P wave.
   - QRS complex.
   - T wave.

   To do this, 'The Electrocardiogram Kit' (ecg-kit) is used. It is an open-source application programming interface that provides tools for accessing and processing ECG signals. It includes algorithms for QRS detection, wave delineation, pulse wave detection and heartbeat classification. The toolbox can be accessed at http://marianux.github.io/ecg-kit/ [111], where documentation and source code are available [112]. In this work, ecg-kit is used for ECG delineation, which involves computing the onset and offset locations for each

ECG wave (P, QRS, and T waves). An example of the report generated by ecg-kit for a 7-second recording from the dataset is shown in Figure 4.6.

As an output of the ECG delineation, the following vectors will be obtained for the analyzed recording, with a number of components equal to the number of detected heartbeats in the signal:

- P_{ON}: Identifies samples where the detected P waves begin.
- P_{OFF}: Identifies samples where the detected P waves end.
- Similarly, QRS_{ON}, QRS_{OFF}, T_{ON} and T_{OFF}.

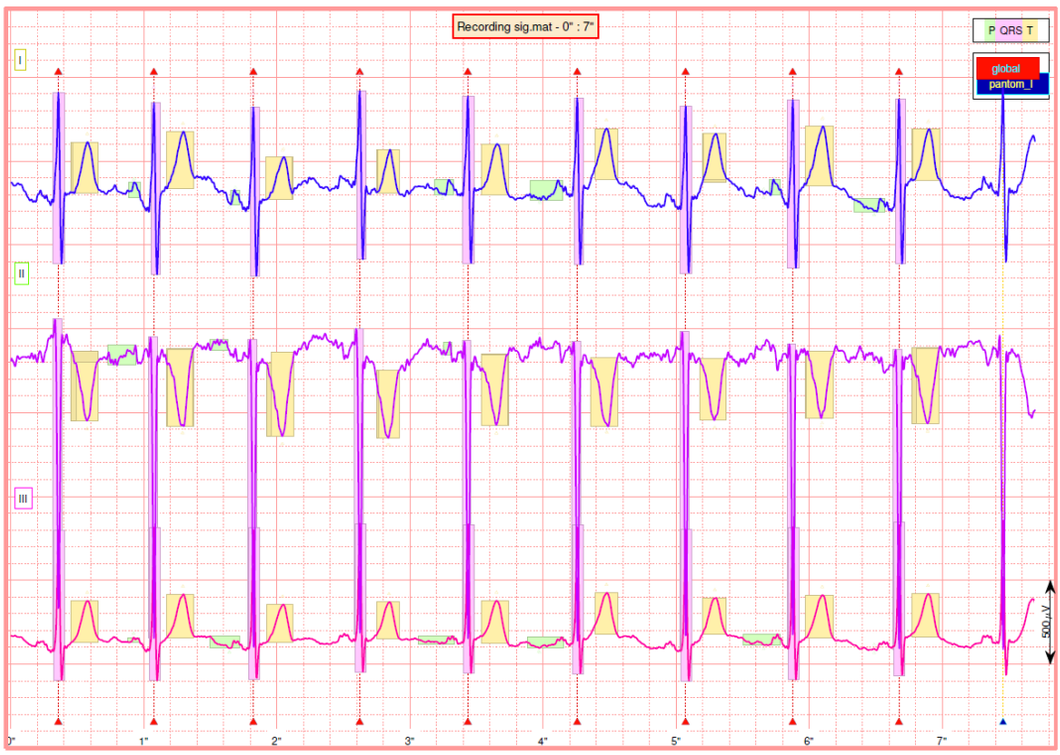

Figure 4.6: A report generated by ecg-kit for a three-lead recording of the Hi-ECG device of 7 seconds. Heartbeats in the ECG signals are indicated by vertical lines, with colour coding representing the type of heartbeat and the corresponding algorithm responsible for detection. Additionally, the delineated waves are overlaid on the signal with different colours: P waves are shown in green, QRS complexes in pink, and T waves in yellow.

3. *Calculating the amplitudes of the waves for each lead*, as described in Figure 4.7.

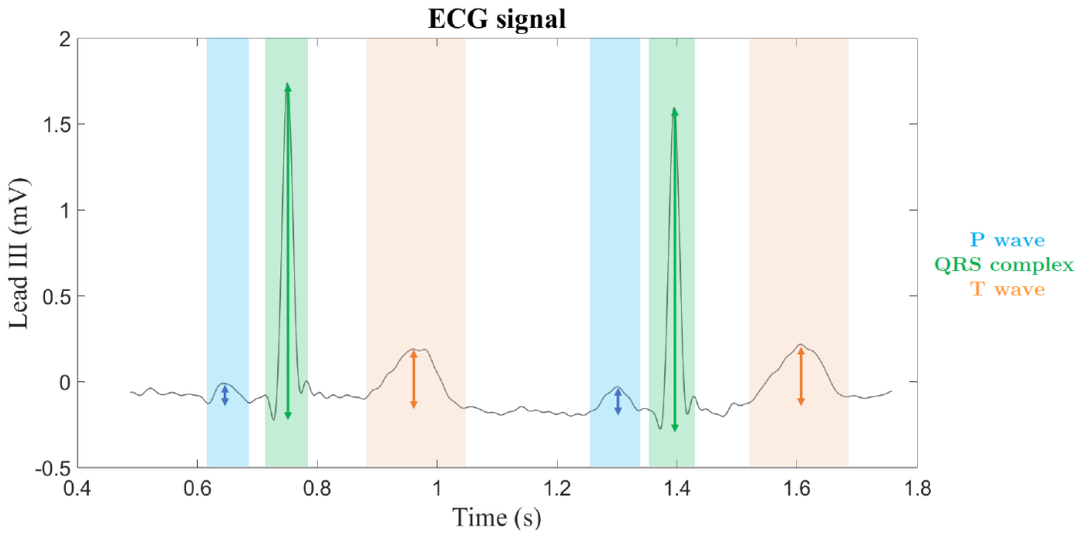

Figure 4.7: Graphical representation of the calculation process for wave amplitudes. Considering each wave separately, the amplitude is computed as: $Ampl_w = |\max(\text{signal}_w) - \min(\text{signal}_w)| \cdot \text{sgn}(\max(\text{signal}_w) - \min(\text{signal}_w))$, where w represents P, QRS, and T. For example, $signal_P$ corresponds to the P wave of the signal.

4. *Determining the angles related to the instantaneous cardiac electrical vector* at:

   - Atrial depolarization (P-wave axis): θ_P
   - Ventricular depolarization (mean axis): θ_{QRS}
   - Ventricular repolarization (T-wave axis): θ_T

   This step follows the procedure reported in Figure 4.8, which is different depending on the configuration under analysis. It relies on the method described in paragraph 1.3.3, where heart vector is projected onto the three lead lines (Figure 4.9). In these calculations, I and III refer to amplitude of waves in lead 1 and lead 3 recorded with the Hi-ECG device. P, QRS, and T are referred to the portions of the signal corresponding to the P waves, QRS complexes, and T waves, respectively. For example, $I(P)$ refers to the amplitude of the P waves in the signal, and so on. Finally, x refers to the magnitude of the cardiac electrical vector during depolarization of atria and ventricles and repolarization of ventricles.

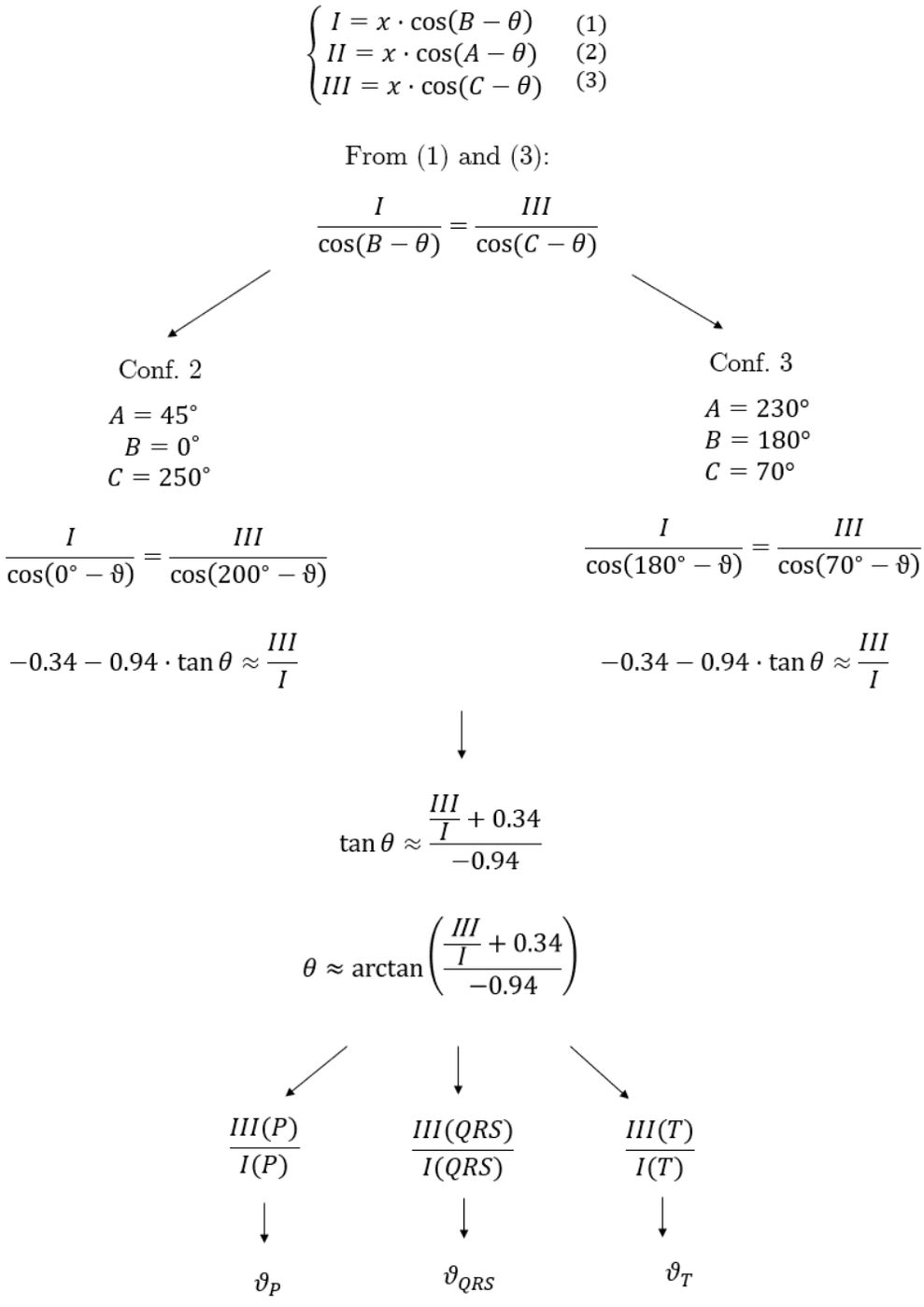

Figure 4.8: Procedure to determine the angles related to the instantaneous cardiac electrical vector

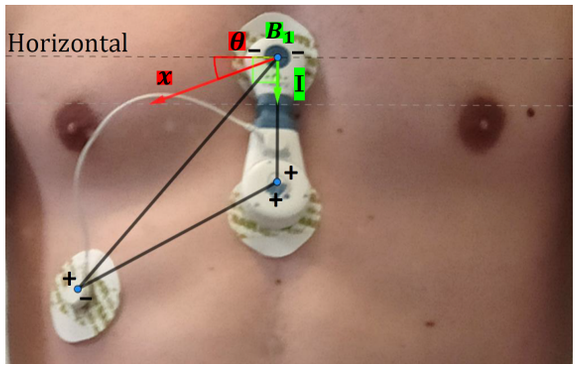

(a) Projection on Lead I line

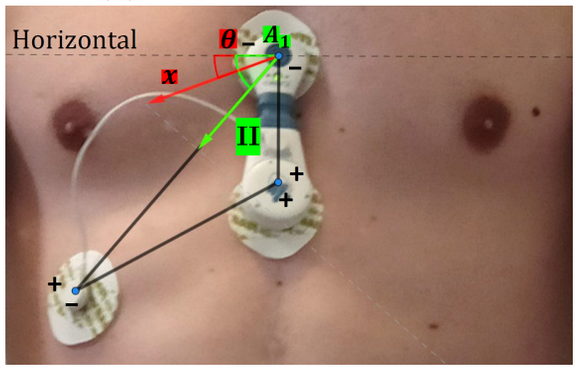

(b) Projection on Lead II line

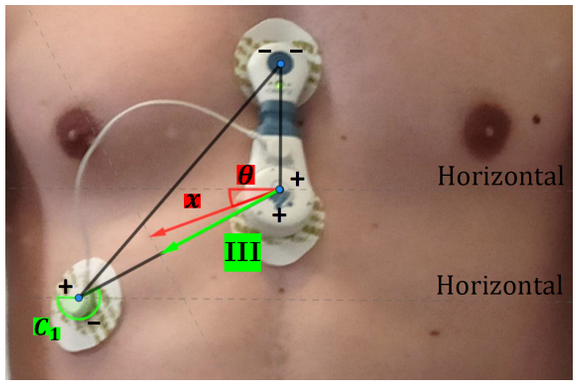

(c) Projection on Lead III line

Figure 4.9: Projection of the electrical heart axis on the lead lines

5. *Reconstructing the magnitude of the instantaneous cardiac electrical vector* (x) based on the previously calculated angles. For each lead, different equations are applied depending on the configuration being analyzed (2 or 3). This process is applied to each lead, resulting in reconstructed x values: x_1, x_2,

and x_3. These values are averaged to obtain x_{TOT}. If, for a specific lead, the denominator of one of the equations tends to zero (particularly if it is less than or equal to 0.1), the corresponding lead is excluded from the calculation of x_{TOT}. Detailed calculation regarding this step can be found in Figure 4.10.

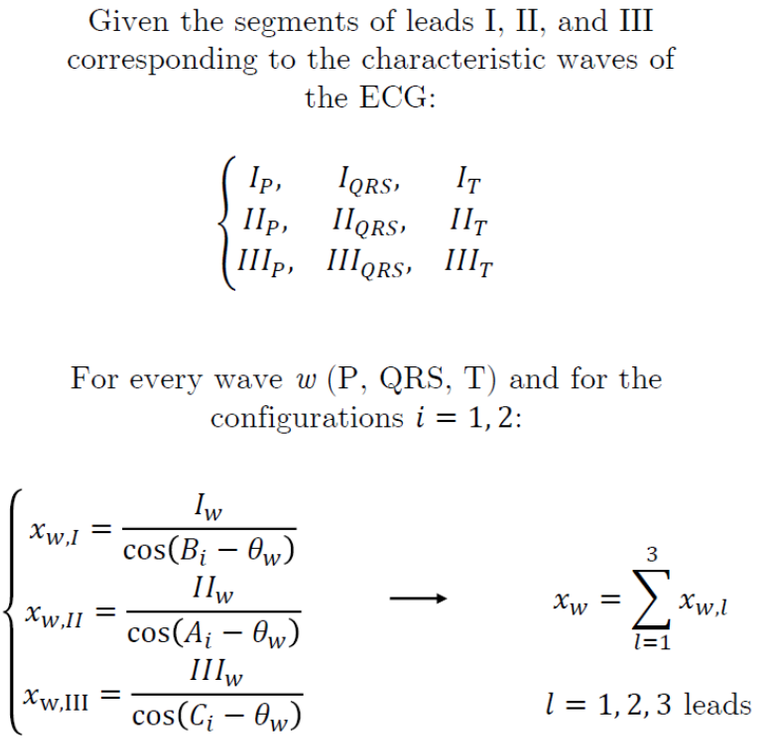

Figure 4.10: Procedure to obtain the magnitude of instantaneous heart vector during P, QRS and T waves basing on the results of segmentation and the angles θ calculated in the previous steps.

6. *Reconstructing the three leads corresponding to Configuration 1* based on the x_{TOT} value obtained in the previous step. Specifically, the following equations are applied:

$$\begin{aligned} I_{w,1} &= x_w \cdot \cos(B_1 - \theta_w) \\ II_{w,1} &= x_w \cdot \cos(A_1 - \theta_w) \\ III_{w,1} &= x_w \cdot \cos(C_1 - \theta_w) \end{aligned} \tag{4.7}$$

Here, w corresponds to P, T and QRS waves. A_1, B_1 and C_1 are the angle relative to Configuration 1. Finally, θ is the angle of the instantaneous heart vector during depolarization of atria and ventricles and repolarization of ventricles.

4.5 Signal Conversion to the 'Standard' Configuration and Use of the CAD System

The goal of this phase is to make the signals acquired with the Hi-ECG device as similar as possible to the Einthoven leads, which are acquired using a standard placement. The motivation behind this is the different morphology exhibited by the signals acquired with the wearable device, as already discussed in Section 3.1. Therefore, since a labelled database of Hi-ECG signals is not available, it is necessary to 'align' these signals to a morphology similar to that of the signals used for training the DL-Based CAD system.

For this specific task, it is recommended to use a database of 12-lead ECG signals, such as the ones described in Paragraph 2.4.1. The design and development of such a model can follow the pipeline proposed in Chapter 4. It should be noted that this section will only present proposed approaches to the problem found in the literature, as they were not developed in this thesis and should be considered as future work.

4.5.1 LSTM networks for the reconstruction of standard leads

In the work of Sohn et al. [113], a three-lead patch type device, similar to the Hi-ECG device, was used with the goal of reconstructing a 12-Lead Electrocardiogram. As an approach, a Long Short-Term Memory (LSTM) Network was proposed, which was compared to more classical algorithms such as linear regression that have been used in the past for the same purpose but are influenced by the notion that the electrogenesis of the heart is not a purely linear process [114]. On the other hand, LSTM networks are very effective for ECG modelling as they can effectively retain historical information and learn long-term dependencies in the input data. In the cited work, to obtain a personalized model for each user, a single standard 12-lead ECG is required, and the proposed algorithm is graphically represented in Figure 4.11.

The cost function that needs to be minimized during the training of the network is:

$$J = \frac{1}{m} \sum_{i=1}^{m} h\left(y_t, \hat{y}_t\right) \tag{4.8}$$

Here, the cost function is the average of the reconstruction error $h\left(y_t, \hat{y}_t\right)$ for all training samples (m). It can be represented by the mean square error between the original signal y_t (i.e., the standard 12-leads ECG) and the reconstructed signal $\hat{y}_t$.

The main limitations of these methods are the requirement of a reference signal for the reconstruction of standard leads and the lack of testing on patients with

heart disease. Further research needs to be conducted to reconstruct standard leads from patch-type devices like the Hi-ECG device.

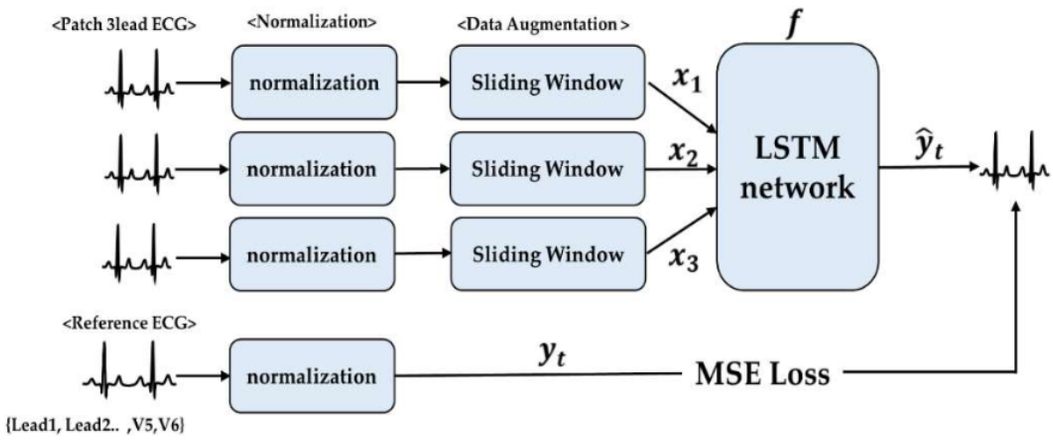

Figure 4.11: Flow of the algorithm proposed by [113]. x_1: Lead 1 ECG data, x_2: Lead 2 ECG data, x_3: Lead 3 ECG data. Reference ECG is needed to compute Mean Square Error (MSE) Loss, that is minimized during training of the LSTM network.

Chapter 5

Results

This chapter presents the results related to the two main tasks developed in this thesis. Specifically, for the first task, "Design and Implementation of a CAD System for Automated ECG Anomaly Classification", the results regarding the preprocessing of the signal from the employed database (MIT-BIH DB) will be discussed. This preprocessing includes the segmentation of signals into denoised beats, which are then fed into the developed CNN. Details will be provided regarding how the training of the network was performed, and the chosen best model will be identified. The evaluation metrics selected for performance assessment and comparison with state-of-the-art works will also be presented.

On the other hand, for the second part of the chapter, the results related to the second task, "Development of a method for adapting a pre-trained CAD system to Hi signals", will be presented. Similarly, the results of signal preprocessing will be shown, this time focusing on signals acquired with the Hi-ECG device. Subsequently, the results regarding the identification of the device placement on the user's chest and the subsequent correction of any detected misplacements will be discussed. Finally, the results related to the conversion of signals into a unique configuration, particularly Configuration 1, will be presented.

5.1 Task #1 Results

In this section, the results of the steps related to the development of a CAD system for the classification of cardiac abnormalities will be described. In particular, the following results will be presented:

- *Signal preprocessing*: the impact of wavelet-based denoising on the signal will be demonstrated, followed by the resulting beats from the segmentation process.
- *Network testing*: metrics related to the top-performing networks will be presented, and finally, a comparison between the selected model for this task and state-of-the-art approaches will be provided.

5.1.1 Data Preprocessing

Figure 5.1 compares a signal from the MIT-DB (specifically, number #100) before and after wavelet-based filtering. The effective elimination of baseline wander can be observed. On the other side, the effect of removing high-frequency noise is most noticeable in individual beats, as shown in Figure 5.2.

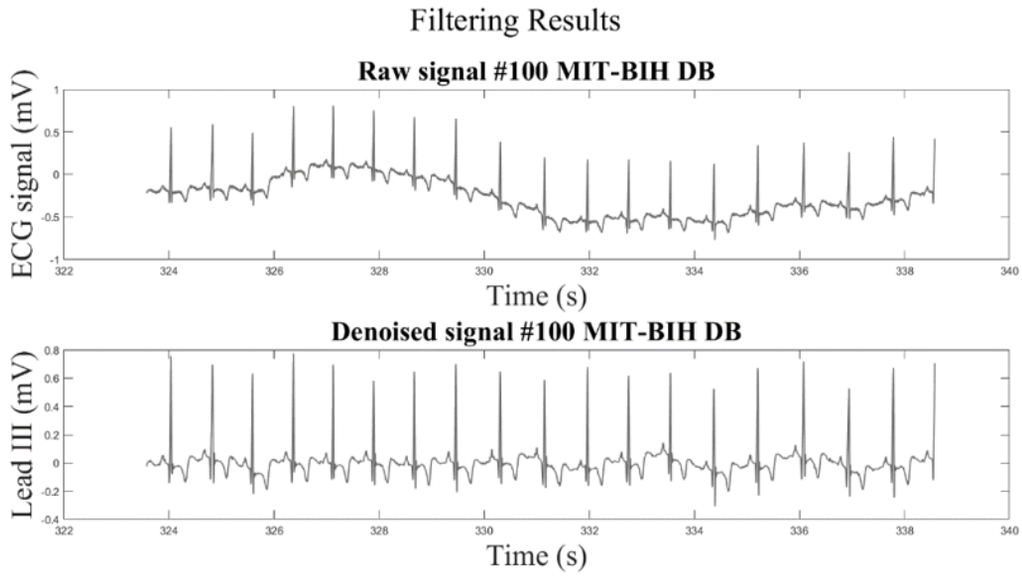

Figure 5.1: Comparison between 15 seconds of an ECG signal from MIT-BIH DB pre- and post-filtering.

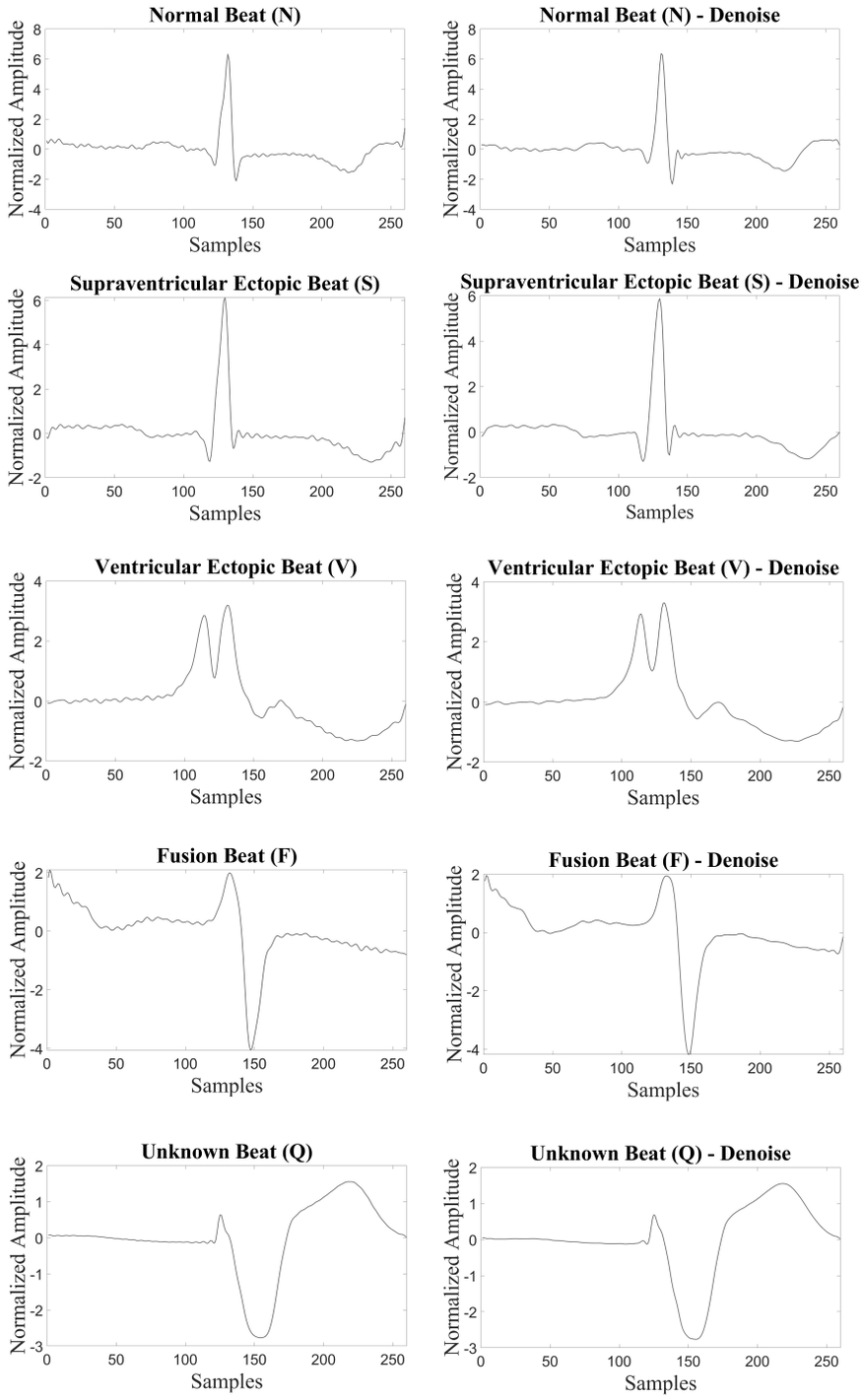

Figure 5.2: Example of segmentation of five beats belonging to superclasses identified by AAMI. The left column shows the beats before filtering, while the right column shows the denoised ones.

The segmentation phase is then carried out on filtered signals to identify the beats that will be given as input to the CNN. Based on the operation of the implemented segmentation algorithm, beats of length 260 samples are obtained, with the R peak located at the centre of the beat.

Figure 5.2 shows five beats obtained after segmentation, belonging to the superclasses identified by AAMI - Normal (N), Supraventricular (S) ectopic, Ventricular (V) ectopic, Fusion (F), and Unknown (Q). These beats have undergone denoising and normalisation using z-score normalisation. A comparison with the corresponding raw beats is also provided to highlight the overall effect of the preprocessing.

After the segmentation process, a database consisting of 102,023 beats is obtained. The distribution of beats in the various classes is reported in Table 5.1. The weight associated with each class is also provided based on the class representation in the dataset. This information is helpful for understanding which classes are more challenging to handle due to their lower representation. The class weight for a particular class is calculated by taking the inverse of its class frequency, which is obtained by dividing the total number of samples by the number of samples in that class. Mathematically, the class weight (W) for class i can be calculated as:

$$W_i = \frac{N}{C \cdot n_i} \tag{5.1}$$

Where N represents the total number of beats in the dataset, C is the number of classes (five in this problem), and n_i represents the number of samples in class i. To ensure that the average weight is 1, the class weights are further normalised by dividing them by the sum of all weights. This normalisation step guarantees that the sum of all class weights equals the number of classes.

5.1.2 CNN Results

This study involved using a CNN-based approach to classify abnormal heartbeats. A rigorous evaluation using a 10-fold cross-validation strategy was conducted to ensure reliable model performance. A total of 90 networks were trained, each with different hyperparameters, through a grid search. The training process utilised the scikit-learn and Keras libraries, with TensorFlow as the backend. The model was trained on a notebook equipped with an Intel® Core™ i7-1195G7 CPU and 16 GB of RAM.

A number of epochs equal to 20 was set during training, but an Early Stopping mechanism was implemented that halted training if the validation set performance did not improve for five consecutive epochs. Notably, the time required for each epoch varied depending on the batch size. For a batch size of 32, an epoch took

Table 5.1: Dataset heartbeats distribution in the five classes recommended by AAMI: Normal (N), Supraventricular (S) ectopic, Ventricular (V) ectopic, Fusion (F), and Unknown (Q).

Class	# of beats	Weight (%)
N	85219	0.60
S	2655	19.24
V	6342	8.05
F	788	64.83
Q	7019	7.28
TOT	102023	100

approximately 60 seconds, while a batch size of 512 reduced the time to around 4 seconds.

Cross-validation and hyperparameter exploration contributed to a comprehensive assessment of model performance. However, it is important to consider the computational cost associated with training 90 networks, which can be considered intensive. On the other hand, the long training time is secondary because, once trained, the system can immediately identify an unknown ECG beat. Moreover, given that CNNs are concurrently-based algorithms training the CNNs with graphics processing unit will help to reduce the complexity and power consumption due to computation.

In order to evaluate the performance and progression of the trained model, we monitored the validation and training loss as well as accuracy throughout the training process. These metrics are key indicators of the model's learning dynamics and generalisation capabilities. Tensorboard – a popular visualisation tool for deep learning experiments – was used to illustrate these trends visually. As an example, Figure 5.3 showcases the evolution of accuracy and loss on both the training and validation sets during training one of the 90 models. It is interesting to note that in this specific instance, the number of epochs was not the expected 20 but rather 17. This discrepancy occurred due to the implementation of Early Stopping, triggered

when no improvement in the validation loss was observed for five consecutive epochs. As expected, validation accuracy and loss are slightly worse than training ones. In fact, with fewer examples, the validation set may exhibit more variability and result in higher uncertainty in the estimated performance metrics.

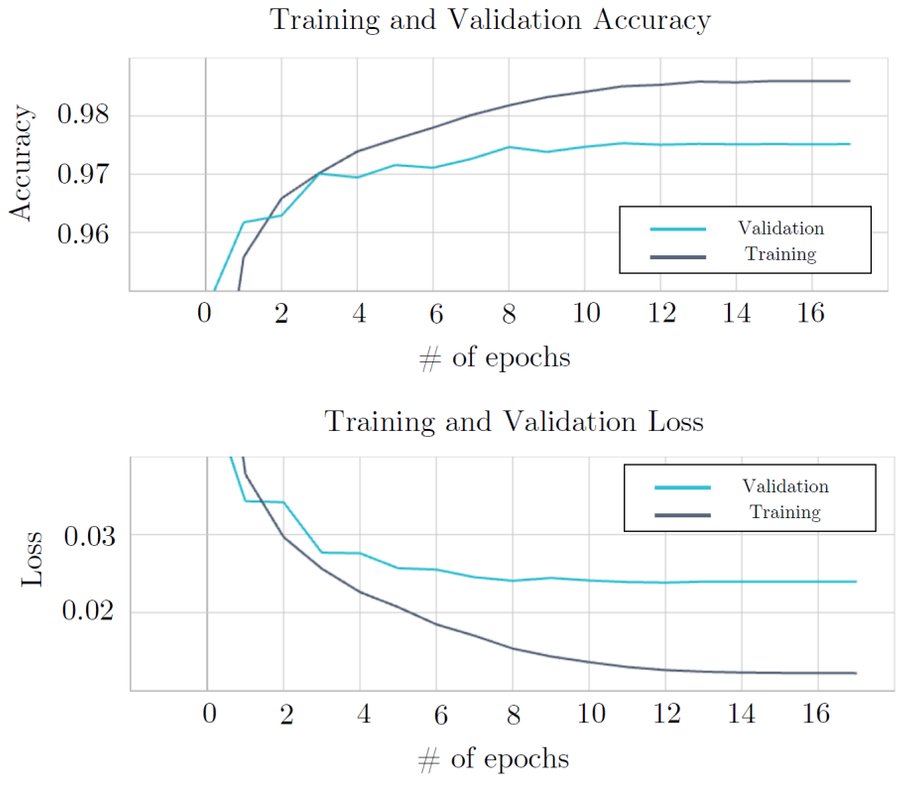

Figure 5.3: Trend of Training and Validation Accuracy and Loss depending on the number of epochs.

5.1.3 Evaluation Metrics and Choice of Best Model

Table 5.2(a) and Table 5.2(b) show the top 10 networks for classifying S-type and V-type beats based on the indexes described in Section 3.7.

Table 5.2: Ranking of the ten best models for S and V -type heartbeats identification, based on $index_s = +P_s + Se_s$ and $index_v = +P_v + Se_v$, where $+P$ is the positive predictivity and Se is the sensitivity.

Set – S beats

Rank	γ	Batch size	LR	$index_S$
1	0.5	32	0.001	1.6102
2	0.5	64	0.001	1.6029
3	0	32	0.001	1.6028
4	0	64	0.001	1.5920
5	1	32	0.001	1.5883
6	0	128	0.01	1.5859
7	0	32	0.01	1.5837
8	0	256	0.01	1.5822
9	0.5	512	0.01	1.5787
10	0.5	256	0.01	1.5786

(a)

Set – V beats

Rank	γ	Batch size	LR	$index_V$
1	1	32	0.001	1.8313
2	0.5	32	0.001	1.8219
3	0.5	64	0.001	1.8201
4	0	256	0.01	1.8198
5	0	32	0.001	1.8188
6	0.5	64	0.01	1.8178
7	0	128	0.01	1.8172
8	2	32	0.001	1.8158
9	1	64	0.001	1.8152
10	0.5	256	0.01	1.8140

(b)

Table 5.3 reports the network results from the intersection between Set V and Set S. Of these networks, the accuracy, metric used for choosing the best model, is reported.

Table 5.3: Ranking of the best models resulting from the intersection of Set S and Set V. Accuracy in percentage was considered as the metric for ranking.

Intersection Set				
Rank	γ	Batch size	LR	Accuracy (%)
1	**0.5**	**32**	**0.001**	**97.72**
2	0	32	0.001	97.62
3	0.5	64	0.001	97.61
4	1	32	0.001	97.60
4	0	256	0.01	97.60
5	0.5	256	0.01	97.53
6	0	128	0.01	97.38

Finally, considering the above results, the model of CNN trained with the following hyperparameters was chosen:

- Focusing parameter (γ) = 0.5
- Batch size = 32
- Initial Learning rate (LR) = 0.001

Given the highly unbalanced nature of the dataset, it was expected that a higher value of the focusing parameter would be necessary to mitigate the impact of the majority class and improve the performance on the minority class. However, upon experimentation, it was surprising to discover that the best-performing networks consistently emerged with a low gamma value. One reason that could explain this finding is that anomalous beats in our dataset exhibited distinct and well-defined patterns that were easier for the model to learn, even in the presence of class imbalance. Moreover, specific subgroups within the majority class could have contributed significantly to misclassification errors. By opting for a lower gamma value, the model could allocate more attention to these challenging examples within the majority class, improving overall classification accuracy. Thus, the

empirical results and thorough analysis guided the selection of a gamma equal to 0.5, challenging the initial expectation but ultimately leading to superior performance in our anomalous beat classification task.

Regarding the batch size value, the fact that a small value was found can be attributed to several factors. Firstly, a small batch size facilitates more frequent weight updates during training than a higher one, allowing the model to learn and adapt to the dataset more rapidly. This characteristic is particularly advantageous when dealing with unbalanced datasets, such as the MIT-BIH DB, as it enables the model to capture the intricate patterns of anomalous beats better. Additionally, a smaller batch size reduces the risk of overfitting, promoting better generalisation to unseen data.

Finally, as the initial value of the learning rate is concerned, it is worth noting that the optimal value can depend on various factors, including the dataset characteristics, network architecture, and complexity of the classification problem. Our empirical findings, precisely an initial learning rate of 0.001, highlight the effectiveness of this choice for our anomalous beat classification task on the MIT-BIH DB.

Overall, this technique does not focus on optimising each parameter individually for the problem, but more on optimising the whole set of parameters, by varying them independently. Therefore, it is more meaningful to consider them as an optimal set rather than as a set of optimal values.

Based on the confusion matrix obtained from the results shown by the chosen model, below are the metrics recommended by the AAMI, as specified in paragraph 3.7, relating to the performance assessment for:

- Distinguishing ‘S’ type beats from other beats (Table 5.4(a))
- Distinguishing ‘V’ type beats from other beats (Table 5.4(b))
- Distinguishing the five AAMI classes (Table 5.5)

From the results, it can be inferred that the beat class that posed the most challenges during classification was the one corresponding to Supraventricular ectopic beats (S). This may be due to their lower proportion in the dataset compared to other beat categories.

Table 5.4: Confusion Matrices relative to the best model and evaluation metrics used to assess the performances of the model in distinguishing S and V -type heartbeats. Abbreviations: ACC: Accuracy; FN: False Negatives; FP: False Positives; $+P$: Positive predictivity; S: supraventricular ectopic beats; Se: Sensitivity; V: ventricular ectopic beats; TN: True Negatives; TP: True Positives.

True class \ Predicted class	N	S	V	F	Q
N	8459	23	32	3	5
S	65	195	5	0	0
V	56	5	566	4	3
F	13	0	8	57	1
Q	7	0	2	1	693

$$Se_S = TP_S/(TP_S + FN_S) \cdot 100 = 73.58\,\%$$

$$+P_S = TP_S/(TP_S + FP_S) \cdot 100 = 87.44\,\%$$

$$FPR_S = FP_V/(TN_V + FP_V) \cdot 100 = 0.28\,\%$$

$$ACC_S = \frac{TP_S+TN_S}{TP_S+TN_S+FP_S+FN_S} \cdot 100 = 99.04\,\%$$

(a)

True class \ Predicted class	N	S	V	F	Q
N	8459	23	32	3	5
S	65	195	5	0	0
V	56	5	566	4	3
F	13	0	8	57	1
Q	7	0	2	1	693

$$Se_V = TP_V/(TP_V + FN_V) \cdot 100 = 89.27\,\%$$

$$+P_V = TP_V/(TP_V + FP_V) \cdot 100 = 93.86\,\%$$

$$FPR_V = FP_V/(TN_V + FP_V) \cdot 100 = 0.39\,\%$$

$$ACC_V = \frac{TP_V+TN_V}{TP_V+TN_V+FP_V+FN_V} \cdot 100 = 98.96\,\%$$

(b)

Table 5.5: Confusion Matrix relative to the best model and evaluation metrics used to assess the performances of the model in distinguish the five AAMI classes. Abbreviations: ACC: Accuracy; F: Fusion heartbeats; FN: False Negatives; N: Normal heartbeats; Q: Unknown heartbeats; Se: Sensitivity; Sp: Specificity; S: Supraventricular ectopic heartbeats; V: ventricular ectopic beats; TN: True Negatives; TP: True Positives.

True class \ Predicted class	N	S	V	F	Q	Sum
N	8459	23	32	3	5	ΣN = 8522
S	65	195	5	0	0	ΣS = 265
V	56	5	566	4	3	ΣV = 634
F	13	0	8	57	1	ΣF = 79
Q	7	0	2	1	693	ΣQ = 703
						Σ = 10203

$$Sp = TN/\Sigma N \cdot 100 = 99.26\%$$

$$Se_V = TP_V/(TP_V + FN_V) \cdot 100 = 89.27\%$$

$$Se_S = TP_S/(TP_S + FN_S) \cdot 100 = 73.58\%$$

$$Se_F = TP_F/\Sigma F \cdot 100 = 72.15\%$$

$$Se_Q = TP_Q/\Sigma Q \cdot 100 = 98.58\%$$

$$ACC = \frac{TN + TP_s + TP_V + TP_F + TP_Q}{\Sigma} \cdot 100 = 97.72\%$$

Finally, Table 5.6 shows a comparison between the results obtained in the present work and the results of some studies in the literature. Specifically, for the comparison, total accuracy (Acc) and sensitivities in the classification of S-type and V-type beats ($Sens_s$ and $Sens_V$) were selected metrics to be compared.

Table 5.6: Comparison between present work and some literature works on the classification of cardiac abnormalities. The year of publication of the work, the type of approach and the metrics used for the evaluation of the results are reported.

Author	Year	Approach	Performance
This work	2023	DCNN FL	$Acc = 97.72\%$ $Sens_S = 73.58\%$ $Sens_V = 89.27\%$
Zubair et. al [83]	2022	DCNN Cost-Sensitive Loss	$Acc = 93.47\%$ $Sens_S = 89.04\%$ $Sens_V = 84.07\%$
Wang et. al [115]	2020	Dual FC NN	$Acc = 93.94\%$ $Sens_S = 90.30\%$ $Sens_V = 81.40\%$
Zhai et. al [116]	2018	DCNN Dual Heartbeat Coupling	$Acc = 99.81\%$ $Sens_S = 95.03\%$ $Sens_V = 98.47\%$
Acharya et. al [71]	2017	DCNN, Data Augmentation	$Acc = 96.05\%$ $Sens_S = 93.80\%$ $Sens_V = 76.8\%$

5.2 Task #2 Results

This section will present the results related to the proposed methodology for adapting a pre-trained CAD system to Hi-ECG device signals. Specifically, the focus will be on the following steps:

- Denoising and segmentation of the signals.
- Results of patches positioning identification and misplacement correction.
- Conversion of the signals to configuration #1.

5.2.1 Denoising and Segmentation of ECG Signals

The analysed ECG signals are part of a custom-created database for this thesis work, as described in paragraph 4.3.1. Specifically, Table 5.7 presents the distribution, for each recruited subject, of the acquisitions in the three classes used for patches positioning identification. For more information regarding the acquisition procedures, please refer to Appendix.

Each signal has been filtered as described in paragraph 3.3.1. Figure 5.4 reports a comparison between 15 seconds of one of the signals of the database pre- and post-denoising.

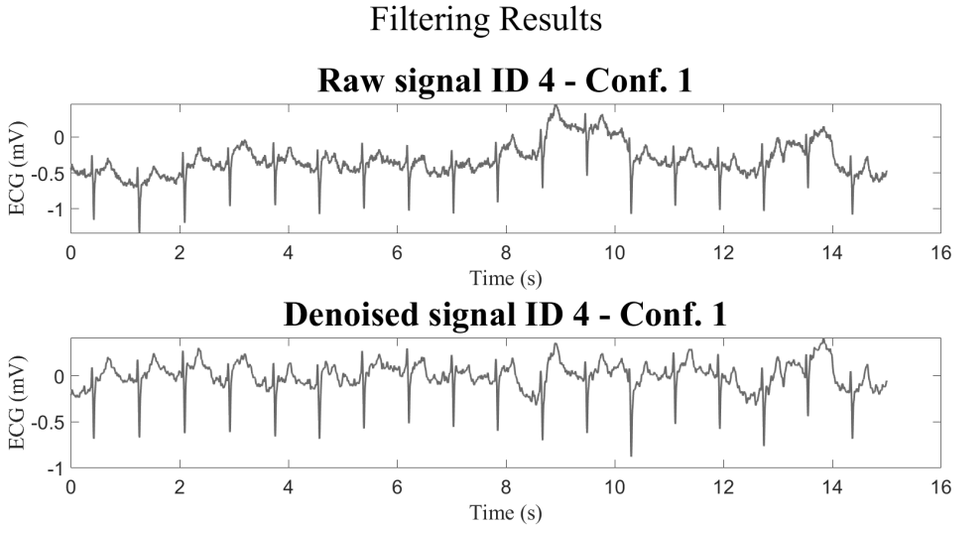

Figure 5.4: Comparison between 15 seconds of a signal in the Hi-ECG database before and after denoising.

Subsequently, the filtered signals were segmented into beats, concatenated then into segments to create the actual dataset used for training the MLP for device

Table 5.7: Distribution of acquisitions made on subjects who participated in the study for each class (e.g., type of positioning of the wearable device).

ID	Class 1	Class 2	Class 3
1	14	10	9
2	12	25	18
3	3	4	4
4	7	5	2
5	3	4	4
6	12	5	5
7	5	7	-
8	6	4	2
9	2	4	3
10	2	6	7
TOT	66	74	54
	194 records x 3 Leads		

placement identification on the user's chest. Figure 5.5 shows examples of these segments referring to acquisitions performed on the same subject (ID10) in the three configurations recommended by the device's user manual.

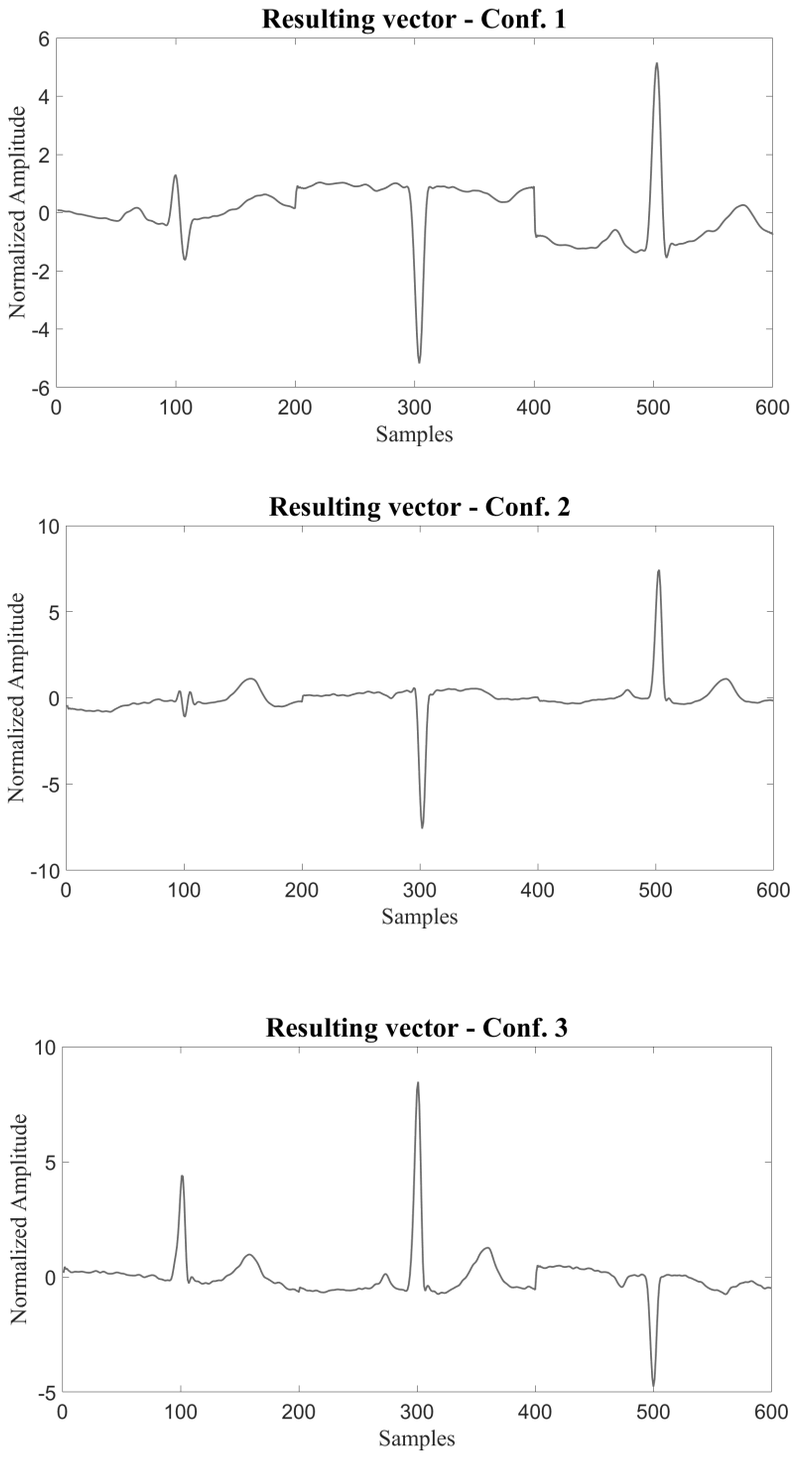

Figure 5.5: Segments resulting from the concatenation of beats in the three leads. Examples are given for each configuration type.

Finally, after segmentation, the dataset used for MLP network training is distributed as shown in Table 5.8.

Table 5.8: Distribution of database segments in the three classes.

Class	# of segments
1	20110
2	18682
3	15347
TOT	54139

5.2.2 Patches Positioning Identification

The training of the MLP for patches positioning in the wearable ECG reader has yielded good results, verified through a rigorous 10-fold cross-validation approach. The dataset was divided into ten folds, allowing for comprehensive evaluation. Following the training process, several metrics were calculated on the test set to assess the performance of the MLP. Results obtained from the ten folds were averaged to obtain the confusion matrix presented in Table 5.9. Accuracy, sensitivity, and specificity for each class are also reported as well as overall results.

Table 5.9: Confusion Matrix of MLP network results and metrics used for its evaluation (Accuracy, Sensitivity and Specificity).

		Predicted class					
		1	2	3	Acc (%)	Sen (%)	Spec (%)
True class	1	1958	31	22	98.97	97.36	99.91
	2	2	1836	30	97.69	98.29	97.38
	3	1	62	1473	97.18	97.27	98.63
Overall					98.18	97.27	98.63

The calculated metrics demonstrate the MLP's ability to accurately classify the patches positions on the body. Sensitivity, a measure of true positive rate, was found to be 97.27%, indicating the model's effectiveness in identifying the correct patches positions. Moreover, the specificity, measuring the true negative rate, was measured at 98.63%, further validating the MLP's ability to correctly identify non-relevant patches positions.

Due to the limited number of subjects recruited for the creation of the Hi-ECG database, the approach used to obtain these results was an intra-patient type, e.g., the segments used for training were also used for testing the network. Further studies need to be conducted to attempt an inter-patient approach, where data is reserved solely for testing, which can be performed according to the description in paragraph 4.3.5. As an example of the inter-patient paradigm, the testing procedure for an acquisition from a subject different from those involved in the database creation is described. The Hi-ECG device was placed in Configuration 1 for this acquisition.

These steps were followed:

- The acquisition was segmented as described earlier, and each segment was fed into the pre-trained MLP network, resulting in a prediction (Figure 5.6).

- Out of a total of 58 segments, only 2 segments were misclassified by the network. To assign a single label to the acquisition, blocks of 10 segments were considered, and for each block, the assigned class was determined as the most frequently occurring value (Figure 5.7).

- The assigned class for the acquisition, in this case, class number 1, is the most frequently occurring value among the labels assigned to the various blocks that compose the signal (Figure 5.8).

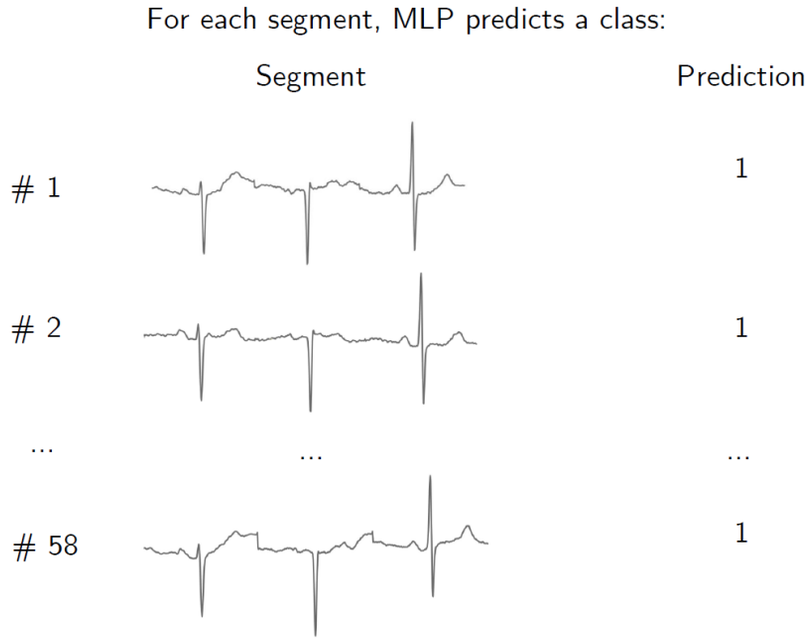

Figure 5.6: Example showing prediction output from MLP for each input segment.

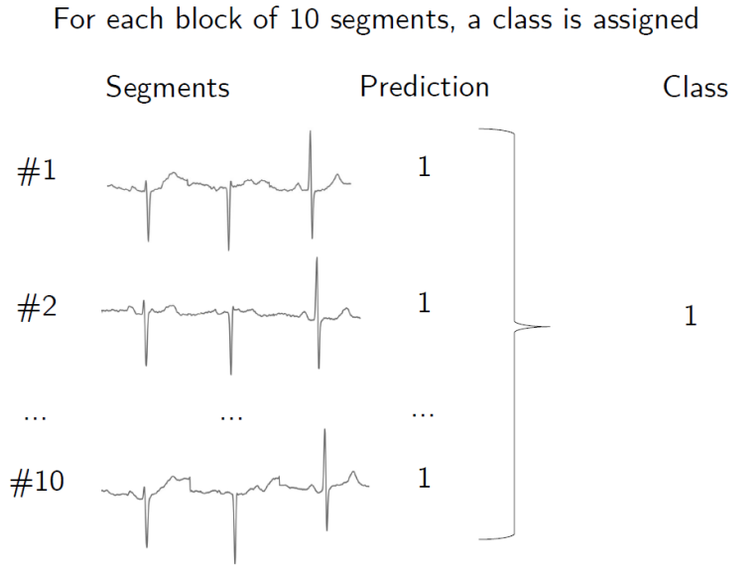

Figure 5.7: Example showing the class associated with a block of 10 segments, based on the most represented prediction. If a block contains less than 10 segments, the zero-padding technique is applied.

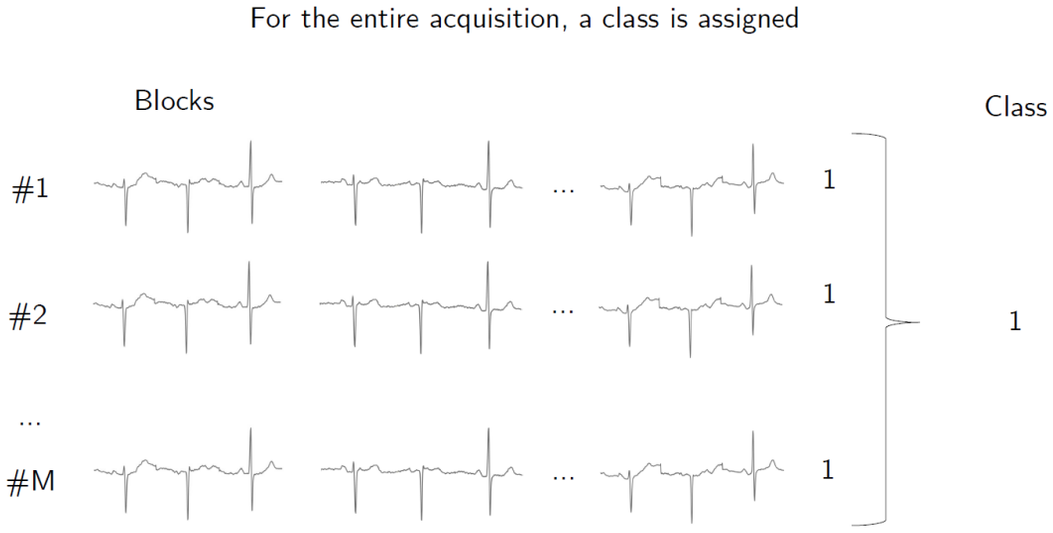

Figure 5.8: Example showing how the class is associated to the entire acquisition based on the most representative value of the blocks. M corresponds to the number of beats of the signal divided by 10. The number is approximated to the upper integer because the zero-padding technique is applied for incomplete blocks.

5.2.3 Misplacement Correction Results

Assuming that the MLP network has correctly classified the class associated to an acquisition, indicating the placement of the Hi-ECG device on the user's chest, the next step is to identify misplacement using the accelerometer data recorded during the acquisition, as described in paragraph 4.3.6.

Table 5.10 presents a comparison of the accelerometer data, obtained as the average acceleration along each axis, recorded on a subject who underwent acquisitions in all types of configurations, including simulating the condition of central body misplacement.

If a central body misplacement is identified, the signals are then corrected as described in paragraph 4.3.6. Figure 5.9 shows an example of signal correction from acquisitions on a subject where the Hi-ECG device was placed in the misplacement Configuration 1. The signals acquired in Configuration 1 are also displayed as a reference for evaluating the correction.

Table 5.10: Accelerations (expressed in g) on the three axes related to the three configurations, also considering the misplacement of the central body. The axis for which the acceleration has greater modulus is highlighted. The distinction between a case of normal configuration and misplacement one can be made based on the sign of acceleration on that axis.

Acc. Values on x, y, z axis (g)	Conf. 1		Conf. 2		Conf.3	
	Normal	Misplacement	Normal	Misplacement	Normal	Misplacement
x	0.92	-1.05	-0.03	-0.21	-0.19	0.03
y	-0.06	0.01	-0.97	0.81	0.78	-0.75
z	-0.07	-0.02	-0.04	0.40	0.51	0.59

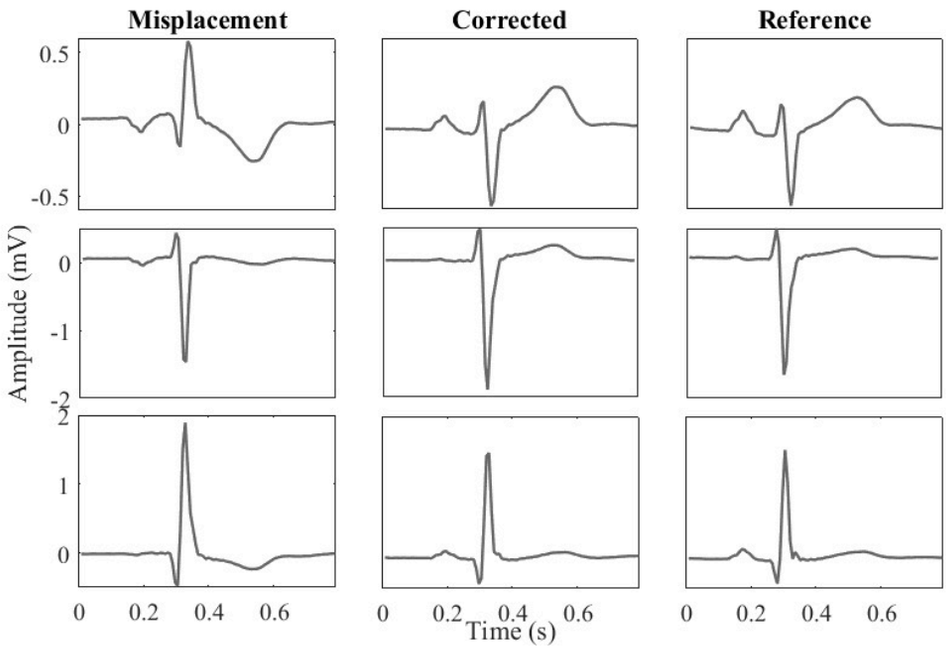

Figure 5.9: Results of the misplacement correction on the three leads, compared with a signal taken from a recording without electrodes misplacement (reference).

Finally, Table 5.11 presents some physiological parameters related to the two signals to assess the success of signal misplacement correction. As can be seen, the correction does not alter the amplitude of the ECG segments, and the swap

between leads 2 and 3 reflects the behaviour of the signal without misplacement.

Table 5.11: Physiological amplitude (QRS AMPL), computed as the sum of the electrical values in correspondence of the peaks Q, R and S of a single beat, and signal amplitude (SIGNAL AMPL), computed along the different ECG leads, comparing a misplaced recording, before and after the correction, with another recording on the same patient without misplacing the device

	Lead	Misplaced	Corrected	Reference
QRS AMPL (mV)	1	1.252	-1.252	-1.238
	2	0.934	-0.318	-0.285
	3	-0.318	0.934	0.953
SIGNAL AMPL (mV)	1	1.355	1.355	1.301
	2	1.208	0.784	0.762
	3	0.784	1.208	1.140

5.2.4 Signals Conversion Results

This paragraph presents the results of the proposed algorithm for converting signals acquired by placing the Hi-ECG device in Configuration 2 or 3 into signals morphologically similar to those acquired in Configuration 1.

Firstly, the geometry associated with the three configurations was computed. This geometry was derived based on photographs taken of the subjects during the signal acquisition phase, which were then analysed to determine the angles associated with each configuration. An example of how the geometry was computed from the subjects' photographs is shown in Figure 5.10.

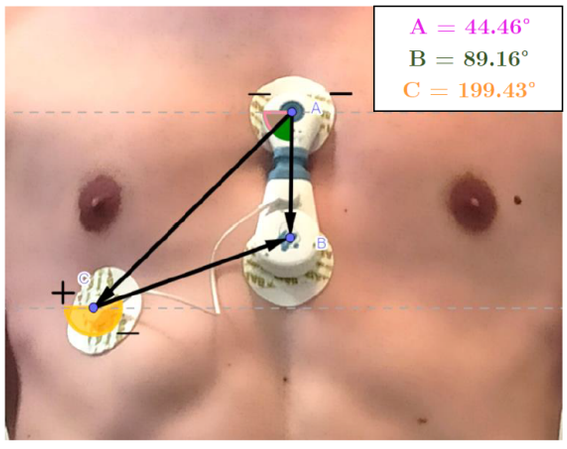

(a) Configuration #1

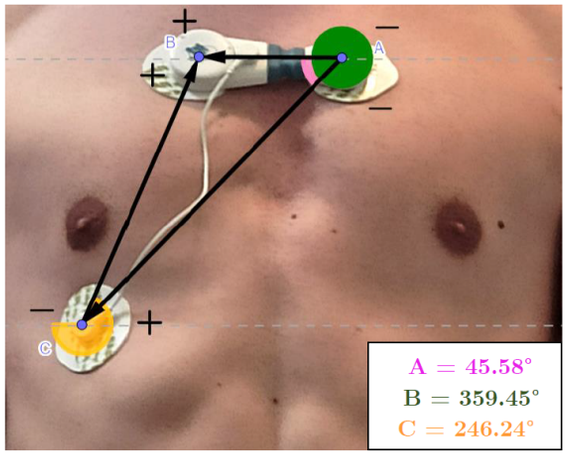

(b) Configuration #2

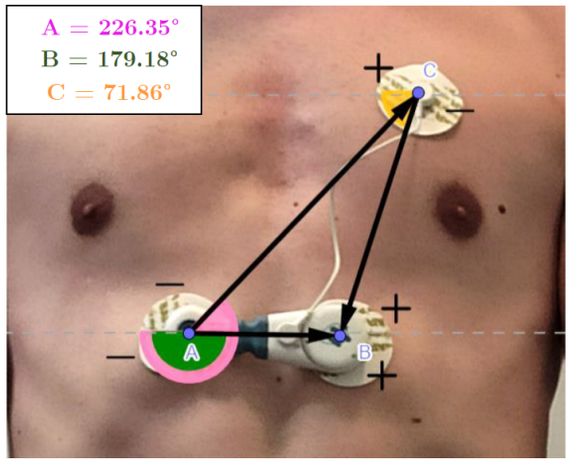

(c) Configuration #3

Figure 5.10: Geometry associated to the three configuration computed for a subject that participate at the study.

The geometries for each subject were averaged to obtain an overall geometry for each configuration, as shown in Table 5.12. Figure 5.11 present the results of the conversion to Configuration 1 for two acquisitions made on the same subject in Configuration 2 and Configuration 3. For comparison, data from an acquisition made in Configuration 1 on the same subject are also provided.

Finally, Table 5.13 displays the wave amplitudes computed along the different ECG leads, comparing the signals of the original configuration, the converted one, and the reference.

Table 5.12: Geometry associated with the three configurations of Hi-ECG device positioning.

Angles	Conf. 1	Conf. 2	Conf. 3
A	45°	45°	230°
B	90°	360°	180°
C	200°	250°	70°

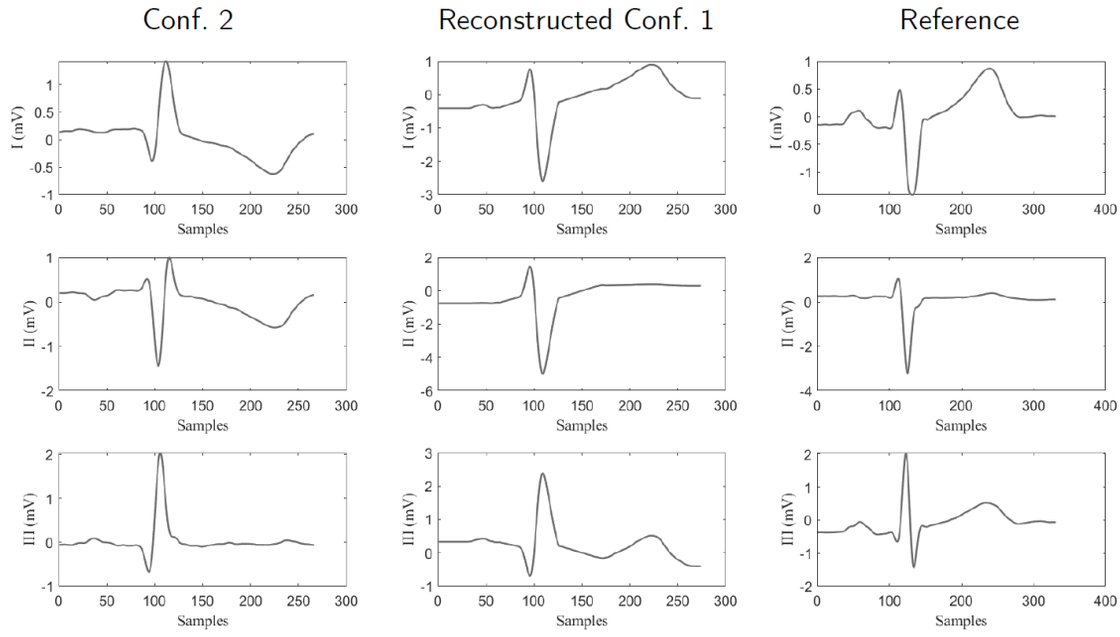

(a) Configuration #2 to #1

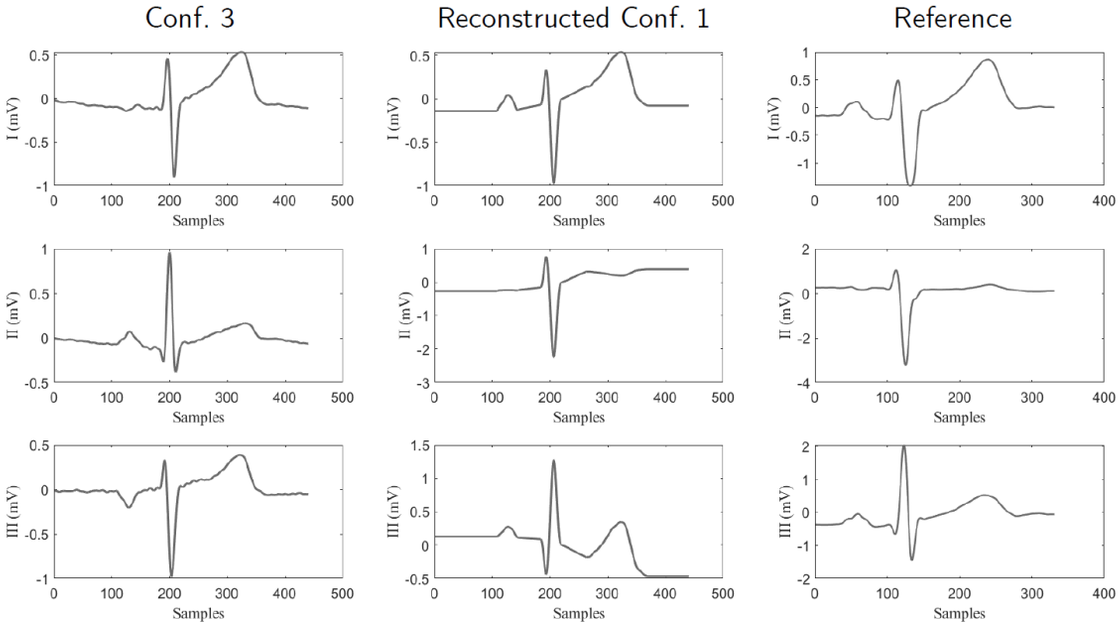

(b) Configuration #3 to #1

Figure 5.11: Signal reconstruction results in Configuration 1 from Configuration 2 and 3. Signals in Configuration 1 are also reported as a reference.

Table 5.13: Comparison between the wave amplitudes of the original (conf. 2 and 3), reconstructed and reference signals (conf. 1).

Reconstruction of Conf. 1 from Conf.2

	Lead	Original	Reconstructed	Reference
P Ampl (mV)	1	-0.05	0.10	0.26
	2	-0.14	-	-
	3	0.09	0.10	0.40
QRS Ampl (mV)	1	1.04	-1.84	-0.91
	2	-0.47	-3.50	-2.23
	3	1.37	1.60	0.59
T Ampl (mV)	1	-0.51	0.88	0.87
	2	-0.58	-	0.18
	3	-	0.39	0.41

(a) Configuration #2 to #1

Reconstruction of Conf. 1 from Conf. 3

	Lead	Original	Reconstructed	Reference
P Ampl (mV)	1	0.10	0.14	0.26
	2	0.14	-	-
	3	-0.20	0.16	0.40
QRS Ampl (mV)	1	-0.44	-0.67	-0.91
	2	0.60	-1.50	-2.23
	3	-0.65	0.80	0.59
T Ampl (mV)	1	+0.53	0.54	0.87
	2	0.16	-	0.18
	3	0.38	0.51	0.41

(b) Configuration #3 to #1

The actual impact of the correction can be observed as the converted leads exhibit the same polarity as the reference. Some morphological differences between the converted signals and the reference, especially in the case of the conversion from configuration 3, may be attributed to the approximations involved in the method. In future developments of this work, a more extensive evaluation of the method is envisioned, analysing the conversion results for other subjects who participated in the study and acquisitions from subjects with cardiac anomalies.

Chapter 6

Conclusions and Future Works

This thesis work is related to research on the classification of anomalies present in electrocardiographic (ECG) signals through Artificial Intelligence-based approaches. In particular, the Hi-ECG device, a wearable ECG recorder commercialised by CompuGroup Medical and developed in collaboration with STMicroelectronics, has been presented. This device can acquire three channels of signals for extended durations of time. Through this device, an approach has been sought to classify cardiac anomalies in order to be integrated on one side into a cardiac telemonitoring system and, on the other, to be used as part of a Computer-Aided Diagnosis (CAD) system to support physicians' diagnosis.

The main challenge encountered in this work is the current absence of a database of Hi-ECG recorded signals containing appropriately labelled anomalies by experts. Based on this consideration, two parallel works have been developed.

The first work involved the development of a CAD system for classifying cardiac anomalies using a publicly available database, particularly the MIT-BIH Database. Based on a 9-layer convolutional neural network, the system successfully classified cardiac anomalies at the beat level with an overall accuracy of 97.72%. The classification followed the ANSI/AAMI EC57:1998/(R) 2008 standard proposed by the Association for Advancement of Medical Instrumentation (AAMI), which categorises heartbeats into five subclasses: Normal (N), Supraventricular (S) ectopic, Ventricular (V) ectopic, Fusion (F), and Unknown (Q).

The proposed methodology, including the signal preprocessing, the chosen network architecture, and the training and testing procedures, can also be applied on signals acquired with Hi-ECG device when a database of recordings with anomalies acquired with it becomes available. In this regard, during this thesis work, the foundations for a possible clinical trial at Mauriziano Hospital in Turin

aimed at creating such a database have been laid.

At the same time, a methodology has been proposed to achieve the objectives of the work without the need for a dedicated database specifically built for Hi-ECG signal classification.

The fundamental premise of this task is that signals acquired by placing the device, as indicated in the user manual, have morphological differences compared to signals obtained by placing the electrodes in the standard Einthoven positions (i.e., on the limbs). Additionally, it is essential to consider both the intra-patient variability, related to the device being placed in different configurations resulting in different morphologies, and the inter-patient variability, due to the variations in electrophysiological characteristics of the cardiac muscle among individuals.

With this understanding, the idea behind this method is to use a pre-trained CAD system with signals considered "standard" including the three Einthoven leads. The objective is to transform the three leads acquired with the Hi-ECG device into "standard" configurations, making them morphologically similar to the signals used for training the CAD system.

To achieve this, it has been proposed to first eliminate the intra-patient variability by employing an experimental method that enables the transformation of all signals acquired with the Hi-ECG device into the morphology corresponding to a singular configuration. The accurate identification of device placement on the patient's chest and the correction of any placement errors resulting from an incorrect reading of the user manual form the basis of this analysis. It is performed by leveraging the accelerometer data recorded by the device during acquisition and using an appropriately trained and tested Multi-Layer Perceptron Network.

The device placement identification work is innovative in the context of wearable devices, as it could also be used to provide feedback to individuals who are required to wear the device without assistance from a specialist independently. In future developments, it is intended to further validate this method by testing it on subjects who did not participate in this study. Additionally, the method will be extended to bedridden subjects, as it is currently designed for subjects in a seated or standing position.

Finally, the last step of the proposed methodology involves obtaining "standard" signals from the Hi-ECG signals, which have been appropriately processed as explained, and the subsequent validation of the CAD system on these signals. The reconstruction of "standard" signals is an increasingly studied problem, and interesting artificial intelligence-based methods have been proposed in recent years. An interesting approach for this task, analysed in this thesis, is using of a Long Short-Term Memory Network, whose implementation can be considered as future development of the work.

Overall, this thesis work demonstrates excellent promise in the field of cardiac anomaly classification, showcasing the potential of wearable devices and artificial intelligence to enhance cardiac monitoring and diagnosis, ultimately improving patient care and outcomes.

Appendix

Hi-ECG Electrodes Positioning for the creation of the Hi-ECG Database.

Manual Configurations

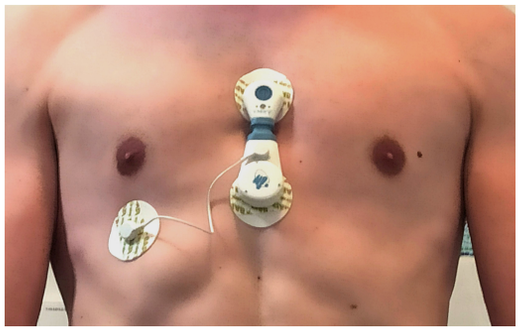

(a) Configuration #1

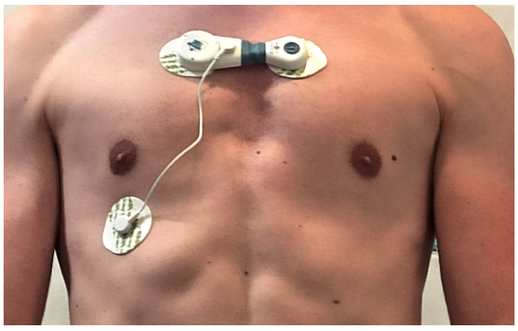

(b) Configuration #2

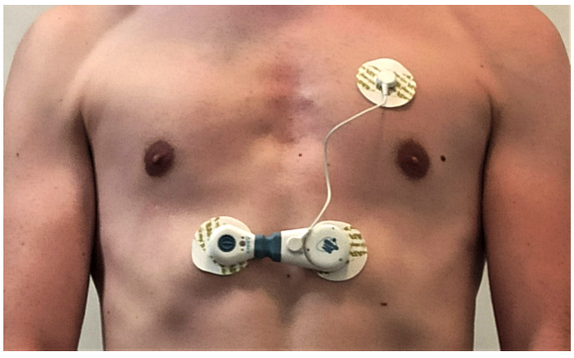

(c) Configuration #3

Misplaced Configurations

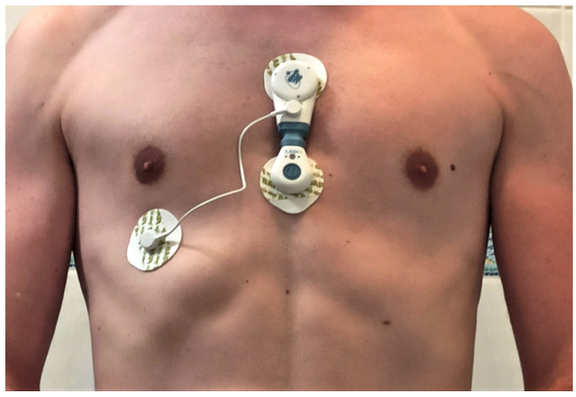

(a) Configuration #1

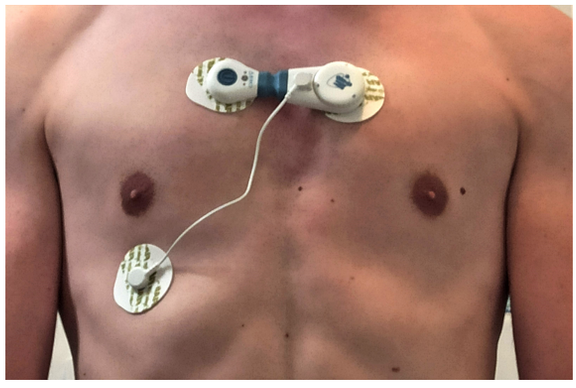

(b) Configuration #2

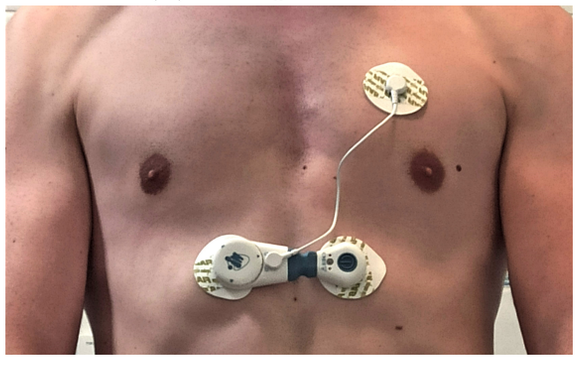

(c) Configuration #3

Main Body Translation - Configuration #1

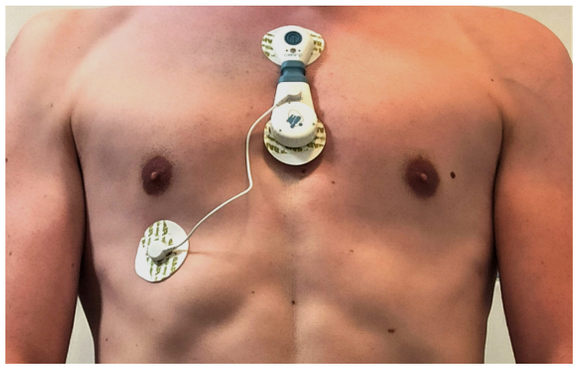

(a) Configuration #1 - high

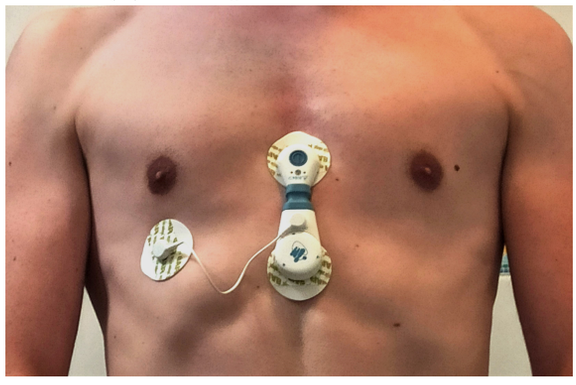

(b) Configuration #1 - low

Main Body Translation - Configuration #2

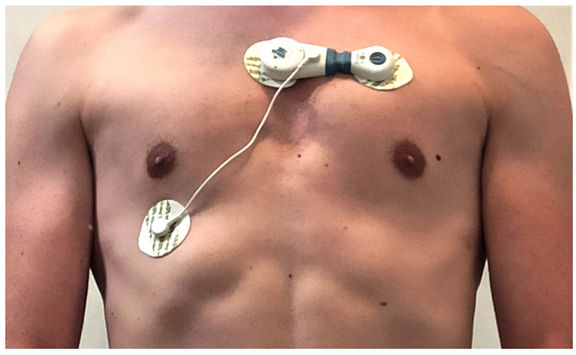

(a) Configuration #2 - right

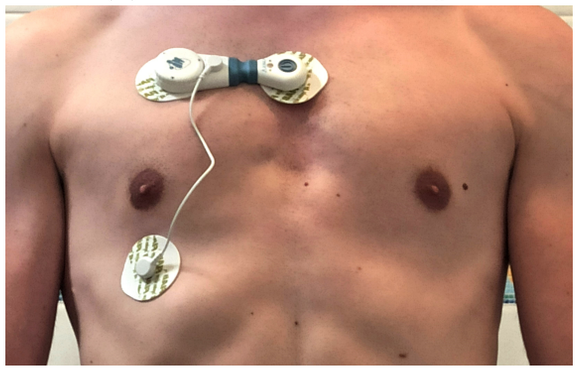

(b) Configuration #2 - left

Main Body Translation - Configuration #3

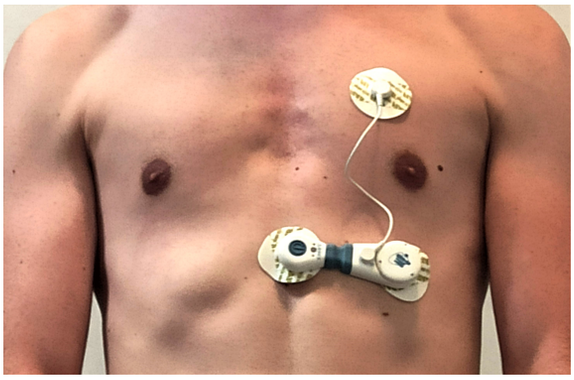

(a) Configuration #3 - right

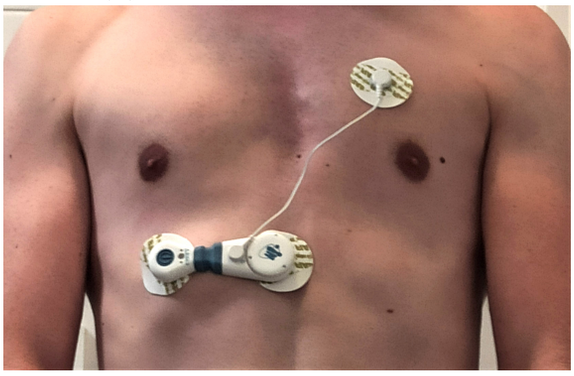

(b) Configuration #3 - left

Bibliography

[1] Maryam A Hyder and Junaid Razzak. «Telemedicine in the United States: an introduction for students and residents». In: *Journal of medical Internet research* 22.11 (2020), e20839 (cit. on p. 3).

[2] A WHO. «Health telematics policy in support of WHO's Health-For-All strategy for global health development». In: *Report of the WHO group consultation on health telematics* (1997), pp. 11–16 (cit. on p. 3).

[3] Gates B Colbert, A Verner Venegas-Vera, and Edgar V Lerma. «Utility of telemedicine in the COVID-19 era». In: *Reviews in cardiovascular medicine* 21.4 (2020), pp. 583–587 (cit. on p. 3).

[4] Nicole Lurie and Brendan G Carr. «The role of telehealth in the medical response to disasters». In: *JAMA internal medicine* 178.6 (2018), pp. 745–746 (cit. on p. 3).

[5] Marco Longoni. «Identificazione di anomalie in tracciati ECG mediante dispositivi indossabili. Algoritmi per l'analisi in movimento ed implementazione ottimizzata per sistemi ultra-low power». MA thesis. Politecnico di Milano, 2017 (cit. on p. 3).

[6] Kamil Kędzierski, Jadwiga Radziejewska, Agnieszka Sławuta, Magdalena Wawrzyńska, and Jacek Arkowski. «Telemedicine in Cardiology: Modern Technologies to Improve Cardiovascular Patients' Outcomes—A Narrative Review». In: *Medicina* 58.2 (2022), p. 210 (cit. on pp. 3, 5).

[7] Manuel Gonzalez Garcia, Farhad Fatehi, and Roghayeh Ershad Sarabi. «Telecardiology and Digital Health for Cardiac Care During COVID-19 Pandemic: Opportunities and Precautions». In: *Health Scope* 9.3 (2020) (cit. on p. 3).

[8] Rafael Vidal-Perez. «eHealth and COVID-19: time for telecardiology». In: *European Society of Cardiology* 21.6 (2021) (cit. on pp. 4, 6).

[9] Eiran Z Gorodeski, Parag Goyal, Zachary L Cox, Jennifer T Thibodeau, Rebecca E Reay, Kismet Rasmusson, Joseph G Rogers, and Randall C Starling. «Virtual visits for care of patients with heart failure in the era of COVID-19: a statement from the Heart Failure Society of America». In: *Journal of Cardiac Failure* 26.6 (2020), pp. 448–456 (cit. on p. 4).

[10] Natale D Brunetti, Antonio Curcio, Savina Nodari, Gianfranco Parati, Stefano Carugo, Martina Molinari, Flavio Acquistapace, Gianfranco Gensini, and Giuseppe Molinari. «The Italian Society of Cardiology and Working Group on Telecardiology and Informatics 2023 updated position paper on telemedicine and artificial intelligence in cardiovascular disease». In: *Journal of Cardiovascular Medicine* 24.Supplement 2 (2023), e168–e177 (cit. on p. 4).

[11] Silvana De Bonis, Nadia Salerno, Antonio Bisignani, Antonella Verta, Cristina Capristo, Antonio Capristo, Gennaro Sosto, Sabato Sorrentino, and Giovanni Bisignani. «The Telecardiology Revolution: From Emergency Management to Daily Clinical Practice». In: *Journal of Clinical Medicine* 11.7 (2022), p. 1920 (cit. on p. 5).

[12] CGMJ Eurlings, JJ Boyne, RA De Boer, and HP Brunner-La Rocca. «Telemedicine in heart failure—more than nice to have?» In: *Netherlands Heart Journal* 27 (2019), pp. 5–15 (cit. on p. 6).

[13] *TeleCheck-AF*. URL: `https://www.fibricheck.com/telecheck-af/` (cit. on p. 5).

[14] Monika Gawałko et al. «The European TeleCheck-AF project on remote app-based management of atrial fibrillation during the COVID-19 pandemic: centre and patient experiences». In: *EP Europace* 23.7 (2021), pp. 1003–1015 (cit. on p. 6).

[15] Aleksandr Ometov et al. «A survey on wearable technology: History, state-of-the-art and current challenges». In: *Computer Networks* 193 (2021), p. 108074 (cit. on p. 7).

[16] Shwetambara Kekade, Chung-Ho Hseieh, Md Mohaimenul Islam, Suleman Atique, Abdulwahed Mohammed Khalfan, Yu-Chuan Li, and Shabbir Syed Abdul. «The usefulness and actual use of wearable devices among the elderly population». In: *Computer methods and programs in biomedicine* 153 (2018), pp. 137–159 (cit. on p. 7).

[17] Andrea Aliverti. «Wearable technology: role in respiratory health and disease». In: *Breathe* 13.2 (2017), e27–e36 (cit. on pp. 7, 8).

[18] *Cardiovascular Diseases - WHO*. URL: `https://www.who.int/health-topics/cardiovascular-diseases#tab=tab_1` (cit. on pp. 8, 9).

[19] *Arrhythmia - American Heart Association*. URL: https://www.heart.org/en/health-topics/arrhythmia (cit. on p. 8).

[20] José Leal, Ramón Luengo-Fernández, Alastair Gray, Sophie Petersen, and Mike Rayner. «Economic burden of cardiovascular diseases in the enlarged European Union». In: *European heart journal* 27.13 (2006), pp. 1610–1619 (cit. on p. 8).

[21] Gizeaddis Lamesgin Simegn, Worku Birhanie Gebeyehu, and Mizanu Zelalem Degu. «Computer-Aided Decision Support System for Diagnosis of Heart Diseases». In: *Research Reports in Clinical Cardiology* (2022), pp. 39–54 (cit. on pp. 9, 34, 35).

[22] Dani Kiyasseh, Tingting Zhu, and David Clifton. «The promise of clinical decision support systems targetting low-resource settings». In: *IEEE Reviews in Biomedical Engineering* 15 (2020), pp. 354–371 (cit. on p. 9).

[23] British Medical Association et al. «Pressure points in the NHS». In: *See https://www. bma. org. uk/advice-and-support/nhs-delivery-and-workforce/pressures/pressu points-in-the-nhs (2020, last checked 2 September 2020)* (2021) (cit. on p. 9).

[24] Spyretta Golemati, Stavroula Mougiakakou, John Stoitsis, Ioannis Valavanis, and Konstantina S Nikita. «Clinical decision support systems: Basic principles and applications in diagnosis and therapy». In: *Clinical Knowledge Management: Opportunities and Challenges*. IGI Global, 2005, pp. 251–270 (cit. on p. 9).

[25] Oliver Faust and Eddie YK Ng. «Computer aided diagnosis for cardiovascular diseases based on ecg signals: A survey». In: *Journal of Mechanics in Medicine and Biology* 16.01 (2016), p. 1640001 (cit. on pp. 10, 26).

[26] Gawsalyan Sivapalan, Koushik Kumar Nundy, Soumyabrata Dev, Barry Cardiff, and Deepu John. «ANNet: A lightweight neural network for ECG anomaly detection in IoT edge sensors». In: *IEEE Transactions on Biomedical Circuits and Systems* 16.1 (2022), pp. 24–35 (cit. on p. 10).

[27] *cgm.com*. URL: https://www.cgm.com/ita_it/telemedicina/cgm-hi-3-leads-ecg-en.html (cit. on pp. 11–13, 81).

[28] *STMicroelectronics: Our technology starts with you*. URL: https://www.st.com/content/st_com/en.html (cit. on p. 12).

[29] Luigi F Agnati. *Fisiologia cardiovascolare*. Piccin-Nuova Libraria, 1996 (cit. on pp. 14, 15, 18, 26, 60).

[30] J Feher. «The Electrocardiogram». In: *Quantitative Human Physiology*. Elsevier, 2012, pp. 537–546 (cit. on pp. 14, 16, 19–21).

[31] João Ribeiro Pinto, Jaime S Cardoso, and André Lourenço. «Evolution, current challenges, and future possibilities in ECG biometrics». In: *IEEE Access* 6 (2018), pp. 34746–34776 (cit. on p. 23).

[32] Margus Metshein, Andrei Krivošei, Anar Abdullayev, Paul Annus, and Olev Märtens. «Non-Standard Electrode Placement Strategies for ECG Signal Acquisition». In: *Sensors* 22.23 (2022), p. 9351 (cit. on p. 23).

[33] Dongseok Lee, Hyunbin Kwon, Hongji Lee, Chulhun Seo, and Kwangsuk Park. «Optimal lead position in patch-type monitoring sensors for reconstructing 12-lead ECG signals with universal transformation coefficient». In: *Sensors* 20.4 (2020), p. 963 (cit. on p. 23).

[34] James P Sheppard, Thomas A Barker, Aaron M Ranasinghe, Thomas H Clutton-Brock, Michael P Frenneaux, and Michael J Parkes. «Does modifying electrode placement of the 12 lead ECG matter in healthy subjects?» In: *International journal of cardiology* 152.2 (2011), pp. 184–191 (cit. on p. 23).

[35] NI Jowett, AM Turner, A Cole, and PA Jones. «Modified electrode placement must be recorded when performing 12-lead electrocardiograms». In: *Postgraduate medical journal* 81.952 (2005), pp. 122–125 (cit. on p. 23).

[36] *MIT-BIH Arrhythmia Directory*. URL: `https://archive.physionet.org/physiobank/database/html/mitdbdir/intro.htm` (cit. on pp. 23, 46, 47).

[37] Sivaraman Jayaraman, Venkatesan Sangareddi, R Periyasamy, Justin Joseph, and Ravi Marimuthu Shanmugam. «Modified limb lead ECG system effects on electrocardiographic wave amplitudes and frontal plane axis in sinus rhythm subjects». In: *Anatolian Journal of Cardiology* 17.1 (2017), p. 46 (cit. on pp. 24, 25).

[38] U Rajendra Acharya, Shankar M Krishnan, Jos AE Spaan, and Jasjit S Suri. *Advances in cardiac signal processing*. Springer, 2007 (cit. on pp. 26, 28–31).

[39] Winston Liaw and Ioannis Kakadiaris. «Artificial intelligence and family medicine: better together». In: *Family Medicine* 52.1 (2020), pp. 8–10 (cit. on pp. 34, 38).

[40] Yoav Mintz and Ronit Brodie. «Introduction to artificial intelligence in medicine». In: *Minimally Invasive Therapy & Allied Technologies* 28.2 (2019), pp. 73–81 (cit. on p. 34).

[41] Faiq Shaikh, Jamshid Dehmeshki, Sotirios Bisdas, Diana Roettger-Dupont, Olga Kubassova, Mehwish Aziz, and Omer Awan. «Artificial intelligence-based clinical decision support systems using advanced medical imaging and radiomics». In: *Current Problems in Diagnostic Radiology* 50.2 (2021), pp. 262–267 (cit. on p. 34).

[42] *Artificial Intelligence for clinical decision support*. URL: https://www.kantify.com/insights/artificial-intelligence-for-clinical-decision-support (cit. on p. 34).

[43] MIT Management Sloan School Sara Brown. *Machine Learning, Explained*. 2021. URL: https://mitsloan.mit.edu/ideas-made-to-matter/machine-learning-explained (cit. on p. 35).

[44] Thomas W Malone, Daniela Rus, and Robert Laubacher. «Artificial intelligence and the future of work». In: *Research Brief* 17 (2020) (cit. on p. 35).

[45] Arijit Ukil, Soma Bandyoapdhyay, Chetanya Puri, and Arpan Pal. «IoT healthcare analytics: The importance of anomaly detection». In: *2016 IEEE 30th international conference on advanced information networking and applications (AINA)*. IEEE. 2016, pp. 994–997 (cit. on p. 35).

[46] Karan Aggarwal, Maad M Mijwil, Abdel-Hameed Al-Mistarehi, Safwan Alomari, Murat Gök, Anas M Zein Alaabdin, Safaa H Abdulrhman, et al. «Has the future started? The current growth of artificial intelligence, machine learning, and deep learning». In: *Iraqi Journal for Computer Science and Mathematics* 3.1 (2022), pp. 115–123 (cit. on p. 35).

[47] Deepack Jakhar and Ishmeet Kaur. «Artificial intelligence, machine learning and deep learning: definitions and differences». In: *Clinical and experimental dermatology* 45.1 (2020), pp. 131–132 (cit. on p. 36).

[48] Anupreet Kaur Singh and Sridhar Krishnan. «ECG signal feature extraction trends in methods and applications». In: *BioMedical Engineering OnLine* 22.1 (2023), pp. 1–36 (cit. on pp. 36, 61).

[49] Shenda Hong, Yuxi Zhou, Junyuan Shang, Cao Xiao, and Jimeng Sun. «Opportunities and challenges of deep learning methods for electrocardiogram data: A systematic review». In: *Computers in biology and medicine* 122 (2020), p. 103801 (cit. on pp. 36, 37, 63).

[50] Jürg Schläpfer and Hein J Wellens. «Computer-interpreted electrocardiograms: benefits and limitations». In: *Journal of the American College of Cardiology* 70.9 (2017), pp. 1183–1192 (cit. on p. 36).

[51] Shu Lih Oh, Eddie YK Ng, Ru San Tan, and U Rajendra Acharya. «Automated beat-wise arrhythmia diagnosis using modified U-net on extended electrocardiographic recordings with heterogeneous arrhythmia types». In: *Computers in biology and medicine* 105 (2019), pp. 92–101 (cit. on p. 37).

[52] Özal Yildirim. «A novel wavelet sequence based on deep bidirectional LSTM network model for ECG signal classification». In: *Computers in biology and medicine* 96 (2018), pp. 189–202 (cit. on pp. 37, 59).

[53] Jinyuan He. «Automated Heart Arrhythmia Detection from Electrocardiographic Data». PhD thesis. Victoria University, 2020 (cit. on pp. 37, 38, 43, 44, 48, 54, 57).

[54] Sandeep Raj, Kailash Chandra Ray, and Om Shankar. «Cardiac arrhythmia beat classification using DOST and PSO tuned SVM». In: *Computer methods and programs in biomedicine* 136 (2016), pp. 163–177 (cit. on p. 38).

[55] Roshan Joy Martis, M Muthu Rama Krishnan, Chandan Chakraborty, Sarbajit Pal, Debranjan Sarkar, KM Mandana, and Ajoy Kumar Ray. «Automated screening of arrhythmia using wavelet based machine learning techniques». In: *Journal of medical systems* 36 (2012), pp. 677–688 (cit. on p. 38).

[56] Kandala NVPS Rajesh and Ravindra Dhuli. «Classification of ECG heartbeats using nonlinear decomposition methods and support vector machine». In: *Computers in biology and medicine* 87 (2017), pp. 271–284 (cit. on p. 38).

[57] Mohebbanaaz, LV Rajani Kumari, and Y Padma Sai. «Classification of ECG beats using optimized decision tree and adaptive boosted optimized decision tree». In: *Signal, Image and Video Processing* (2021), pp. 1–9 (cit. on p. 38).

[58] Mohamed Sraitih, Younes Jabrane, and Amir Hajjam El Hassani. «An automated system for ECG arrhythmia detection using machine learning techniques». In: *Journal of Clinical Medicine* 10.22 (2021), p. 5450 (cit. on p. 38).

[59] Vahid Tavakoli, Nima Sahba, and Nima Hajebi. «A fast and accurate method for arrhythmia detection». In: *2009 Annual International Conference of the IEEE Engineering in Medicine and Biology Society*. IEEE. 2009, pp. 1897–1900 (cit. on p. 38).

[60] Mehmet Engin. «ECG beat classification using neuro-fuzzy network». In: *Pattern Recognition Letters* 25.15 (2004), pp. 1715–1722 (cit. on p. 38).

[61] Inan Güler and Elif Derya Übeylı. «ECG beat classifier designed by combined neural network model». In: *Pattern recognition* 38.2 (2005), pp. 199–208 (cit. on p. 38).

[62] Eduardo José da S Luz, William Robson Schwartz, Guillermo Cámara-Chávez, and David Menotti. «ECG-based heartbeat classification for arrhythmia detection: A survey». In: *Computer methods and programs in biomedicine* 127 (2016), pp. 144–164 (cit. on pp. 38, 46–49, 73, 74).

[63] Yann LeCun, Bernhard Boser, John Denker, Donnie Henderson, Richard Howard, Wayne Hubbard, and Lawrence Jackel. «Handwritten digit recognition with a back-propagation network». In: *Advances in neural information processing systems* 2 (1989) (cit. on p. 38).

[64] Francesco Piccialli, Vittorio Di Somma, Fabio Giampaolo, Salvatore Cuomo, and Giancarlo Fortino. «A survey on deep learning in medicine: Why, how and when?» In: *Information Fusion* 66 (2021), pp. 111–137 (cit. on p. 38).

[65] Laith Alzubaidi et al. «Review of deep learning: Concepts, CNN architectures, challenges, applications, future directions». In: *Journal of big Data* 8 (2021), pp. 1–74 (cit. on pp. 39–42).

[66] Nadia Jmour, Sehla Zayen, and Afef Abdelkrim. «Convolutional neural networks for image classification». In: *2018 international conference on advanced systems and electric technologies (IC_ASET)*. IEEE. 2018, pp. 397–402 (cit. on pp. 40, 41).

[67] Samuel Yeom, Irene Giacomelli, Matt Fredrikson, and Somesh Jha. «Privacy risk in machine learning: Analyzing the connection to overfitting». In: *2018 IEEE 31st computer security foundations symposium (CSF)*. IEEE. 2018, pp. 268–282 (cit. on p. 41).

[68] ANSI AAMI and AAMI EC57. «Testing and reporting performance results of cardiac rhythm and ST segment measurement algorithms». In: *American National Standards Institute, Arlington, VA, USA* (2008) (cit. on p. 43).

[69] Manab Kumar Das. «Electrocardiogram signal analysis for heartbeat pattern classification». PhD thesis. 2015 (cit. on p. 43).

[70] Jianwei Zheng, Jianming Zhang, Sidy Danioko, Hai Yao, Hangyuan Guo, and Cyril Rakovski. «A 12-lead electrocardiogram database for arrhythmia research covering more than 10,000 patients». In: *Scientific data* 7.1 (2020), p. 48 (cit. on pp. 43, 45).

[71] U Rajendra Acharya, Shu Lih Oh, Yuki Hagiwara, Jen Hong Tan, Muhammad Adam, Arkadiusz Gertych, and Ru San Tan. «A deep convolutional neural network model to classify heartbeats». In: *Computers in biology and medicine* 89 (2017), pp. 389–396 (cit. on pp. 43, 52, 63, 64, 66, 109).

[72] Jen Hong Tan, Yuki Hagiwara, Winnie Pang, Ivy Lim, Shu Lih Oh, Muhammad Adam, Ru San Tan, Ming Chen, and U Rajendra Acharya. «Application of stacked convolutional and long short-term memory network for accurate identification of CAD ECG signals». In: *Computers in biology and medicine* 94 (2018), pp. 19–26 (cit. on p. 44).

[73] Shu Lih Oh, Eddie YK Ng, Ru San Tan, and U Rajendra Acharya. «Automated diagnosis of arrhythmia using combination of CNN and LSTM techniques with variable length heart beats». In: *Computers in biology and medicine* 102 (2018), pp. 278–287 (cit. on pp. 44, 62).

[74] Özal Yıldırım, Paweł Pławiak, Ru-San Tan, and U Rajendra Acharya. «Arrhythmia detection using deep convolutional neural network with long duration ECG signals». In: *Computers in biology and medicine* 102 (2018), pp. 411–420 (cit. on p. 44).

[75] U Rajendra Acharya, Hamido Fujita, Oh Shu Lih, Yuki Hagiwara, Jen Hong Tan, and Muhammad Adam. «Automated detection of arrhythmias using different intervals of tachycardia ECG segments with convolutional neural network». In: *Information sciences* 405 (2017), pp. 81–90 (cit. on p. 45).

[76] Weiyi Yang, Yujuan Si, Di Wang, and Gong Zhang. «A novel approach for multi-lead ECG classification using DL-CCANet and TL-CCANet». In: *Sensors* 19.14 (2019), p. 3214 (cit. on p. 45).

[77] Hao Tung, Chao Zheng, Xinsheng Mao, and Dahong Qian. «Multi-lead ECG classification via an information-based attention convolutional neural network». In: *Journal of Shanghai Jiaotong University (Science)* (2020), pp. 1–15 (cit. on p. 45).

[78] Vikto Tihonenko, A Khaustov, S Ivanov, A Rivin, and E Yakushenko. «St Petersburg INCART 12-lead arrhythmia database». In: *PhysioBank PhysioToolkit and PhysioNet* (2008) (cit. on p. 48).

[79] *PhysioBank Annotations*. URL: `https://archive.physionet.org/physiobank/annotations.shtml` (cit. on p. 48).

[80] *PTB Diagnostic ECG Database*. URL: `https://physionet.org/content/ptbdb/1.0.0/` (cit. on p. 48).

[81] *CU Ventricular Tachyarrhythmia Database*. URL: `https://physionet.org/content/cudb/1.0.0/` (cit. on p. 48).

[82] Feifei Liu et al. «An open access database for evaluating the algorithms of electrocardiogram rhythm and morphology abnormality detection». In: *Journal of Medical Imaging and Health Informatics* 8.7 (2018), pp. 1368–1373 (cit. on p. 48).

[83] Muhammad Zubair and Changwoo Yoon. «Cost-sensitive learning for anomaly detection in imbalanced ECG data using convolutional neural networks». In: *Sensors* 22.11 (2022), p. 4075 (cit. on pp. 49, 52, 109).

[84] Diego Carrera, Beatrice Rossi, Daniele Zambon, Pasqualina Fragneto, and Giacomo Boracchi. «Ecg monitoring in wearable devices by sparse models». In: *Machine Learning and Knowledge Discovery in Databases: European Conference, ECML PKDD 2016, Riva del Garda, Italy, September 19-23, 2016, Proceedings, Part III 16*. Springer. 2016, pp. 145–160 (cit. on pp. 51, 79).

[85] George B Moody and Roger G Mark. «The impact of the MIT-BIH arrhythmia database». In: *IEEE engineering in medicine and biology magazine* 20.3 (2001), pp. 45–50 (cit. on p. 52).

[86] U Rajendra Acharya, Hamido Fujita, Oh Shu Lih, Yuki Hagiwara, Jen Hong Tan, and Muhammad Adam. «Automated detection of arrhythmias using different intervals of tachycardia ECG segments with convolutional neural network». In: *Information sciences* 405 (2017), pp. 81–90 (cit. on p. 52).

[87] U Rajendra Acharya, Hamido Fujita, Shu Lih Oh, Yuki Hagiwara, Jen Hong Tan, and Muhammad Adam. «Application of deep convolutional neural network for automated detection of myocardial infarction using ECG signals». In: *Information Sciences* 415 (2017), pp. 190–198 (cit. on pp. 52, 62).

[88] Tsung-Yi Lin, Priya Goyal, Ross Girshick, Kaiming He, and Piotr Dollár. «Focal loss for dense object detection». In: *Proceedings of the IEEE international conference on computer vision*. 2017, pp. 2980–2988 (cit. on pp. 52, 67, 68).

[89] Aswathy Velayudhan and Soniya Peter. «Noise analysis and different denoising techniques of ECG signal-a survey». In: *IOSR J. Electron. Commun. Eng* 1.1 (2016), pp. 40–44 (cit. on pp. 54, 55).

[90] Rahul Kher et al. «Signal processing techniques for removing noise from ECG signals». In: *J. Biomed. Eng. Res* 3.101 (2019), pp. 1–9 (cit. on p. 55).

[91] Manpreet Kaur, Birmohan Singh, and Seema. «Comparison of different approaches for removal of baseline wander from ECG signal». In: *Proceedings of the international conference & workshop on emerging trends in technology*. 2011, pp. 1290–1294 (cit. on p. 55).

[92] Larisa G Tereshchenko and Mark E Josephson. «Frequency content and characteristics of ventricular conduction». In: *Journal of electrocardiology* 48.6 (2015), pp. 933–937 (cit. on p. 56).

[93] Elhassane Abdelmounim, Rachid Haddadi, Abdelaziz Belaguid, et al. «Electrocardiogram signal denoising using discrete wavelet transform». In: *2014 International Conference on Multimedia Computing and Systems (ICMCS)*. IEEE. 2014, pp. 1065–1070 (cit. on p. 56).

[94] Brij N Singh and Arvind K Tiwari. «Optimal selection of wavelet basis function applied to ECG signal denoising». In: *Digital signal processing* 16.3 (2006), pp. 275–287 (cit. on p. 57).

[95] V Seena and Jerrin Yomas. «A review on feature extraction and denoising of ECG signal using wavelet transform». In: *2014 2nd international conference on devices, circuits and systems (ICDCS)*. IEEE. 2014, pp. 1–6 (cit. on p. 57).

[96] Inan Güler and Elif Derya Übeylı. «ECG beat classifier designed by combined neural network model». In: *Pattern recognition* 38.2 (2005), pp. 199–208 (cit. on p. 57).

[97] *Introduction to the Wavelet Families*. URL: `https://it.mathworks.com/help/wavelet/gs/introduction-to-the-wavelet-families.html` (cit. on p. 57).

[98] Mounaim Aqil, Atman Jbari, and Abdennasser Bourouhou. «ECG Signal Denoising by Discrete Wavelet Transform.» In: *International journal of online engineering* 13.9 (2017) (cit. on pp. 59, 60).

[99] C Saritha, V Sukanya, and Y Narasimha Murthy. «ECG signal analysis using wavelet transforms». In: *Bulg. J. Phys* 35.1 (2008), pp. 68–77 (cit. on p. 59).

[100] Danilo Ricciardi et al. «Impact of the high-frequency cutoff of bandpass filtering on ECG quality and clinical interpretation: A comparison between 40 Hz and 150 Hz cutoff in a surgical preoperative adult outpatient population». In: *Journal of electrocardiology* 49.5 (2016), pp. 691–695 (cit. on pp. 60, 79).

[101] Jiapu Pan and Willis J Tompkins. «A real-time QRS detection algorithm». In: *IEEE transactions on biomedical engineering* 3 (1985), pp. 230–236 (cit. on pp. 60, 61).

[102] Edmund Do, Jack Boynton, Byung Suk Lee, and Daniel Lustgarten. «Data augmentation for 12-lead ecg beat classification». In: *SN Computer Science* 3 (2022), pp. 1–17 (cit. on p. 63).

[103] Xavier Glorot and Yoshua Bengio. «Understanding the difficulty of training deep feedforward neural networks». In: *Proceedings of the thirteenth international conference on artificial intelligence and statistics*. JMLR Workshop and Conference Proceedings. 2010, pp. 249–256 (cit. on p. 64).

[104] Kizito Nyuytiymbiy. «Parameters and hyperparameters in machine learning and deep learning». In: *Towards Data Science* (2022) (cit. on p. 65).

[105] Machine Learning Mastery Jason Brownlee. *Understand the Impact of Learning Rate on Neural Network Performance*. 2020. URL: `https://machinelearningmastery.com/understand-the-dynamics-of-learning-rate-on-deep-learning-neural-networks/` (cit. on p. 67).

[106] David E Rumelhart, Richard Durbin, Richard Golden, and Yves Chauvin. «Backpropagation: The basic theory». In: *Backpropagation: Theory, architectures and applications* (1995), pp. 1–34 (cit. on p. 67).

[107] Paul Kligfield et al. «Recommendations for the standardization and interpretation of the electrocardiogram: part I: the electrocardiogram and its technology: a scientific statement from the American Heart Association Electrocardiography and Arrhythmias Committee, Council on Clinical Cardiology; the American College of Cardiology Foundation; and the Heart Rhythm Society endorsed by the International Society for Computerized Electrocardiology». In: *Circulation* 115.10 (2007), pp. 1306–1324 (cit. on p. 79).

[108] Giovanni Di Martino. «ECG PRE-PROCESSING & AF DETECTION ALGORITHM for ECG-WATCH DEVICE». PhD thesis. Politecnico di Torino, 2020 (cit. on p. 79).

[109] Fionn Murtagh. «Multilayer perceptrons for classification and regression». In: *Neurocomputing* 2.5-6 (1991), pp. 183–197 (cit. on p. 80).

[110] Matt W Gardner and SR Dorling. «Artificial neural networks (the multilayer perceptron)—a review of applications in the atmospheric sciences». In: *Atmospheric environment* 32.14-15 (1998), pp. 2627–2636 (cit. on p. 84).

[111] *ecg-kit*. URL: `http://marianux.github.io/ecg-kit/` (cit. on p. 89).

[112] Mariano Llamedo Soria. «ecg-kit: a Matlab Toolbox for Cardiovascular Signal Processing». In: (2016) (cit. on p. 89).

[113] Jangjay Sohn, Seungman Yang, Joonnyong Lee, Yunseo Ku, and Hee Chan Kim. «Reconstruction of 12-lead electrocardiogram from a three-lead patch-type device using a LSTM network». In: *Sensors* 20.11 (2020), p. 3278 (cit. on pp. 96, 97).

[114] Ramesh M Gulrajani. «The forward and inverse problems of electrocardiography». In: *IEEE Engineering in Medicine and Biology Magazine* 17.5 (1998), pp. 84–101 (cit. on p. 96).

[115] Haoren Wang, Haotian Shi, Ke Lin, Chengjin Qin, Liqun Zhao, Yixiang Huang, and Chengliang Liu. «A high-precision arrhythmia classification method based on dual fully connected neural network». In: *Biomedical Signal Processing and Control* 58 (2020), p. 101874 (cit. on p. 109).

[116] Xiaolong Zhai and Chung Tin. «Automated ECG classification using dual heartbeat coupling based on convolutional neural network». In: *IEEE Access* 6 (2018), pp. 27465–27472 (cit. on p. 109).